LEHRSTUHL FÜR BIOMEDIZINISCHE PHYSIK

TECHNISCHE UNIVERSITÄT MÜNCHEN

CONTRIBUTIONS TO X-RAY PHASE-CONTRAST IMAGING WITH AN ENERGY–SENSITIVE PHOTON–COUNTING DETECTOR

FRANZ MICHAEL EPPLE

DISSERTATION

DECEMBER 2015

SUPERVISORS:
PROF. DR. SIBYLLE ZIEGLER
PROF. DR. FRANZ PFEIFFER

Technische Universität München

Technische Universität München
Physik Department
Lehrstuhl für Biomedizinische Physik

Contributions to
X-Ray Phase-Contrast Imaging with an Energy-Sensitive Photon-Counting Detector

Franz Michael Epple

Vollständiger Abdruck der von der Fakultät für Physik der Technischen Universität
München zur Erlangung des akademischen Grades eines

Doktors der Naturwissenschaften (Dr. rer. nat.)

genehmigten Dissertation.

Abstract

In recent years, the field of X-ray imaging has gained increasing interest in research and industry as a result of major technological and conceptual breakthroughs. One of the promising imaging concepts is X-ray differential phase-contrast imaging with a Talbot-Lau interferometer, which has proven to be feasible with conventional incoherent and polychromatic X-ray sources. Further, it was demonstrated to provide valuable complementary information about the object. Also in the field of X-ray imaging detectors an important development has been made with energy-sensitive single-photon counting detectors, which for instance provide noise-free energy-discriminated measurements. Today, both differential phase-contrast imaging with a Talbot-Lau interferometer and energy-sensitive photon-counting detectors are promising concepts, which are about to be translated from research into real clinical and industrial use.

However, one limitation for differential phase-contrast imaging for real applications arises from phase wrapping, which leads to errors in the measured phase and to strong artefacts in the final images. The correction of those errors, the phase-unwrapping, is still unresolved to a large degree and thus of great interest in research. In the framework of this thesis, a new phase-unwrapping method has been developed that exploits the spectral information delivered by an energy-sensitive photon-counting detector in order to reconstruct the true phase estimated in the sense of maximum-likelihood. Initially, the method was developed for consecutive monochromatic measurements and has been tested by means of according experimental data acquired at the synchrotron. Subsequently, the unwrapping method has been extended to conventional polychromatic X-ray sources combined with an energy-sensitive photon-counting detector. For the acquisition of the X-ray images the new LAMBDA detector has been utilized. To demonstrate its potential for spectral application in the field of biomedical X-ray imaging, the K-edge imaging method has been briefly investigated.

In conclusion, the results accomplished in this work provide a basis to correct for phase wrapping artefacts that are a major issue in grating-based phase-contrast imaging. Therefore, the findings of this thesis may contribute to translate the differential phase-contrast imaging technique from research to routine applications in the clinical and industrial area.

Zusammenfassung

Aufgrund wichtiger technologischer und konzeptioneller Durchbrüche sind die bildgebenden Verfahren mit Röntgenstrahlen in den vergangen Jahren wieder verstärkt in den Fokus der Forschung gerückt. Eines dieser vielversprechenden Bildgebungsverfahren ist die differenzielle Phasenkontrast- und Dukelfeldbildgebung. Diese Bildgebungsmethode ist mit einem Talbot-Lau Interferometer, in Kombination mit inkoheränten Röntgenquellen umsetzbar und liefert wertvolle komplementäre Informationen über das zu untersuchende Objekt. Eine weitere wichtige Entwicklung sind energiesensitive photonenzählende Röntgendetektoren. Diese ermöglichen es, rauschfreie Röntgenbilder aus unterschiedlichen Energiebereichen des Röntgenspektrums aufzunehmen. Sowohl die differentielle Phasenkontrast- und Dunkelfeldbildgebung mit Talbot-Lau Interferometer, als auch die photonenzählenden Detektoren haben großes Potential in den nächsten Jahren den Sprung aus der Forschung hin zu klinischen und industriellen Anwendungen zu schaffen.

Ein bisher weitgehend ungelöstes Problem der differentiellen Phasenkontrastbildgebung für reale Anwendungen ist das Auftreten von sogenannten Phasewrapping-Artefakten: Dabei wird ein falscher Phasenwert gemessen, was zu deutlichen Fehlern im Phasenbild führt. Im Rahmen dieser Dissertation wurde ein neuer Ansatz zur Korrektur der Phasewrapping-Artefakte entwickelt, welcher die spektrale Information der energiesensitiven photonenzählenden Röntgendetektoren ausnutzt, um die echte Phase mittels Maximum-Likelihood zu rekonstruieren. Diese spektrale "phase unwrapping" Methode wurde zunächst für mehrere hintereinander ausgeführte monochromatische Messungen entwickelt und ihr Potential anhand entsprechender Messungen am Synchrotron evaluiert. Danach wurde die Methode auf Messungen mit energiesensitiven Detektoren an konventionellen polychromatischen Röntgenquellen erweitert. Die spektralen Phasenkontrastbilder wurde mit dem photonenzählenden Röntgendetektor LAMBDA aufgenommen. Um das Potential dieses neuen Röntgendetektors für klinische Anwendungen aufzuzeigen, wurde zudem die spektrale K-Kanten Bildgebung als zusätzliches Anwendungsgebiet untersucht.

Zusammengefasst liefert diese Arbeit einen Ansatz zur Korrektur von Phasewrapping-Artefakten und trägt damit dazu bei, die Translation der spektralen differentiellen Phasenkontrastbildgebung aus der Forschung zu klinischen und industriellen Anwendungen voranzutreiben.

Contents

Chapter 1

Introduction

X-RAYS were first reported in 1895 by Wilhelm Conrad Röntgen (1845-1923, Würzburg University, Germany), after he observed this new kind of rays during experiments with Lenard and Crookes tubes [1]. He was awarded the first Nobel Prize in physics in 1901 for their systematical investigation.

Shortly after their discovery, X-rays lead to revolutionary changes in science, industrial research, and clinical diagnostics because of their ability to pass through solid matter and to provide an image from its inner structure. This property of X-rays generated large enthusiasm resulting in their first use by battlefield physicians to locate bullets in wounded soldiers, only six months after their discovery [2]. Later, when X-ray tubes were able to produce rays with a sufficient power to penetrate metal parts, it became also interesting for industrial applications.

In the early stages, X-ray images were captured with photographic plates, i.e. glass plates coated with a light-sensitive emulsion of silver salts, which locally turns black when hit by an X-ray photon. Later, photographic plates were mostly replaced by screen films; however it was only possible to capture single 2-dimensional radiographic images from the object.
This changed with the availability of the first solid-state detectors which provided a better sensitivity, an improved image quality, and –most importantly– allowed to digitally post-process the acquired images. The possibility to subsequently process the images with the help of a computer lead to the invention of computed tomography (CT) by Godfrey Hounsfield (EMI Laboratories, England) and Allan Cormack (Tufts University, Massachusetts) in 1972. They accomplished computed three-dimensional representations of the scanned object through acquisition of several radiographic images from different viewing angles. In 1979, both scientist were awarded the Nobel Prize for their contributions to medicine and science.

While X-ray imaging based on the attenuation of their intensity in the scanned

object is well suited to detect large density differences, as for example between bones or calcifications and soft tissue, it often fails to distinguish between different types of soft tissue with similar densities. This issue was tackled with the development of X-ray phase-contrast imaging, which generates contrast from phase changes that the X-ray wavefront undergoes when passing through the object. With a cross section that is up to three orders of magnitude larger than the attenuation cross section, the phase shift provides a superior soft tissue contrast, in particular in the low energy regime. In recent years, different phase-imaging techniques have been developed, which are generally categorized as propagation-based [3,4], analyzer-based [5,6], and grating-based imaging [7,8].

The grating-based technique, which exploits the Talbot effect using an X-ray interferometer, is subject of this work. The interferometer consists of two or three gratings and is referred to as Talbot or Talbot-Lau interferometer, respectively. The Talbot interferometer utilizes a phase grating to introduce an intensity modulation, or more precisely multiple intensity modulations at distinct distances, further downstream. When an object is placed in the beam, the intensity modulation is distorted due to the imposed phase shift. The distortion is resolved by a stepping procedure performed with an absorption grating in front of the detector, which samples the modified intensity pattern. From the measured distortion it is possible to regain the phase shift that was imposed by the object. In recent years, grating-based X-ray imaging has been proven to visualize features that are not detectable with conventional attenuation-based imaging, as it provides complementary contrast types, namely differential phase contrast and the scatter-based dark-field contrast.

The advances in novel X-ray imaging techniques were facilitated to a large extend by new detector technologies that have emerged in the last decades. New concepts such as solid-state detectors, as already mentioned, lead to significant improvements in sensitivity and noise reduction, which came along with a reduction of both measuring time and radiation dose. The latest concept of single-photon–counting detectors, which has been investigated in recent years has the potential for the next great change in medical and industrial micro-CT imaging. Because their ability for classical-noise free measurements, to count individual X-ray photons and to measure their energy brings several benefits: Among others, they allow for improved signal-to-noise ratio, reduction of beam hardening and metal artifacts, material or tissue type-specification, quantitative imaging, and simultaneous multi-agent imaging.

This doctoral thesis seeks to investigate the benefits arising when both technologies, grating-based differential-phase contrast imaging and energy-sensitive single-photon– counting detectors, are combined.

To put this work in context, earlier scientific work by different groups about grating-based phase-contrast imaging combined with an energy-sensitive detector, needs to be acknowledged: First preliminary studies about the energy dependency of phase-contrast and dark-field signals have been done by Weber et al. in 2011 and Bayer et al. in 2012, respectively. They performed spectroscopic X-ray phase-contrast and dark-field measurements using a grating-based Talbot-Lau interferometer combined with the

Timepix detector [9, 10]. In 2012, Weber et al. accomplished energy-resolved visibility measurements for the optimization of the Talbot-Lau interferometer [11]. In 2013, Thuering et al. utilized an energy-sensitive detector equipped with a CdTe sensor, provided by W. C. Barber, to investigate the dependency of noise on the spectral bandwidth, with the aim to optimize the interferometer system with respect to sensitivity and dose [12, 13]. In 2013, Pelzer et al. used the energy-sensitive detector Dosepix to optimize the contrast-to-noise-ratio of grating-based X-ray differential phase-contrast images. For this purpose they combined images that have been recorded simultaneously at different spectral bandwidths with appropriate energy-weights [14]. In 2014, Pelzer et al. extended the concept of contrast-to-noise-ratio enhancement using spectral measurements to the area of dark-field imaging [15].

In the framework of this thesis, the energy-sensitive photon-counting detector LAMBDA has been used to perform spectral measurements in order to utilize the spectral information for the correction of phase-wrapping artefacts.

The thesis is structured as follows:

After this introduction, chapter 2 outlines the theoretical background about X-rays and their properties, and introduces the most common concepts of X-ray detectors, including energy-discriminating photon-counting detectors. Moreover, the grating-based phase-contrast imaging modality including signal extraction and the three-dimensional image reconstruction is explained.

Chapter 3 is devoted to the energy-sensitive photon-counting detector LAMBDA which was used to acquire the experimental data throughout this work. First, the Medipix3 ASIC and its imaging schemes are introduced. After that, the description of a preliminary high-speed readout concept of the LAMBDA detector is given, which was developed and implemented on the FPGA as part of this work.

In chapter 4, a method for phase-wrapping artifact correction is investigated that utilizes the noise model of differential phase-contrast imaging and exploits the spectral information provided by energy sensitive-detectors.

First, the phase-wrapping problem is introduced as it appears in grating-based phase-contrast imaging. Subsequently, the appropriate noise model is theoretically derived and possible approximations are given. After that, the method for phase wrapping correction is presented, which utilizes the derived noise model and the spectral information, provided by energy sensitive detectors, to estimate the unwrapped phase using the maximum-likelihood method. Finally, the method is experimentally evaluated with both multiple monochromatic measurements acquired at a synchrotron source as well as with simultaneously acquired images using the LAMBDA detector and a polychromatic X-ray source.

In chapter 5, a preliminary experimental study about K-edge imaging with multiple contrast agents is given, and first results about the combination with phase-contrast imaging are shown.

Finally, chapter 6 summarizes this work and discusses possible perspectives.

Chapter 2

Theoretical Background | X-ray Imaging and Detectors

2.1 Introduction

This chapter provides an overview of the theoretical background about the generation of X-rays, their physical properties and their interaction with matter. A particular focus is set on the grating-based phase-contrast imaging modality, as well as on X-ray detectors.

2.2 X-ray generation

X-rays are generated with an X-ray tube as illustrated in Fig. 2.1 (a). It basically consists of two opposing electrodes, the cathode and the anode, in a vacuum enclosure. The cathode filament is heated by an applied voltage and releases electrons proportional to the filament current $(50 - 300 \, \text{mA})$ due to thermionic emission. An additional high voltage $(10 - 160 \, \text{kV})$ applied between the cathode and the anode accelerates the emitted electrons towards the anode. X-rays are produced by converting the kinetic energy of the electrons into electromagnetic radiation due to collisional and radiative interactions [16]. The accelerated electrons interact with the atoms of the target material (i.e. the anode material), for instance tungsten or molybdenum, by the processes shown in Fig. 2.1 (b). Most of the kinetic energy of the electrons striking the target is converted into heat, and only less than $1\,\%$ is transformed into X-rays. As the electrons are decelerated and deflected by the atoms the loss of energy goes along with an emission of electromagnetic radiation with an energy depending on the interaction strength. Electrons that directly hit the atomic nucleus, lose all their energy in a single collision and emit X-rays with the highest possible energy $E_{Xmax} = eV_T$ with $e = 6.02 \times 10^{19} \, \text{C}$, which is the maximum kinetic energy of the electrons as determined by the applied voltage. As the distance to the atomic nucleus increases, the strength of deceleration and deflection and thus the energy of the respective X-ray decreases. In conclusion, the deceleration and deflection of the electrons results in an electromagnetic spectrum, known as Bremsstrahlung, with a
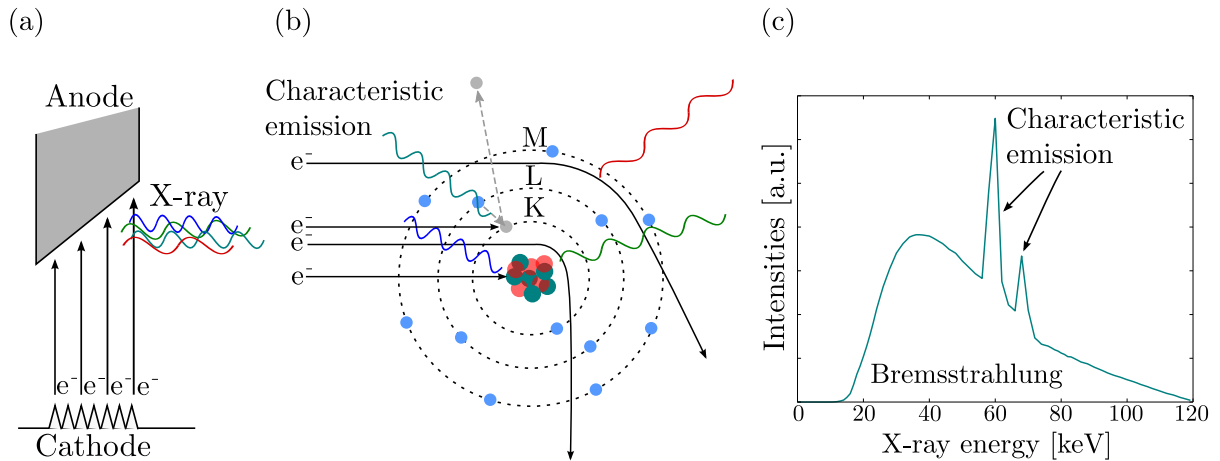
(a)   (b)   (c)

Figure 2.1: (a) Sketch of an X-ray tube showing the electrons being emitted from the cathode and accelerated towards the anode. By interacting with the anode material, X-rays are generated. (b) Interaction processes between the electrons and the atoms of the anode material generate Bremsstrahlung and characteristic emission. (c) Spectrum of an X-ray tube with continuous Bremsstrahlung and characteristic emission peaks.

minimum number of X-rays at the peak energy of the electrons, which linearly increases towards decreasing energy, see Fig. 2.1 (c). The emitted Bremsstrahlung intensity I_{Bs} of the X-ray tube is empirically given by

$$I_{Bs} \propto Z I_T V_T^2, \tag{2.1}$$

and thus depends on the atomic number Z of the target material, the tube current I_T and acceleration voltage V_T. As discovered by W. H. Bragg, the electrons are not only decelerated and deflected but also interact with the inner shell electrons of the target material. This occurs, if the kinetic energy of the accelerated electrons is equal or larger than the energy of the K-shell binding energy, allowing them to remove a K-shell electron. This results in an energetically unstable electron configuration. Therefore, electrons from higher orbits (L, M, N, O) transit to the vacant position in the K-shell resulting in the emission of characteristic X-ray photons with an energy equal to the difference in binding energies. In the continuous Bremsstrahlung's spectrum those photons can be seen as strong intensity peaks shown in Fig. 2.1 (c). The peak intensity I_C is empirically given by

$$I_C \propto I_T (V_T - V_O)^{1.5}, \tag{2.2}$$

and depends on the difference between the acceleration voltage V_T and the excitation voltage V_O of the orbit.

2.3 X-ray properties and free-space propagation

In the classical pictures of X-rays as electromagnetic waves with wavelength λ and propagation direction $\mathbf{k}$, their temporal and spatial variation can be described [17] by

$$\Psi(\mathbf{r}, t) = \mathbf{E}_0 e^{i(\mathbf{k} \cdot \mathbf{r} - \omega t)} \tag{2.3}$$

with a polarized amplitude $\mathbf{E}_0 = \hat{\mathbf{e}} E_0$ with unit polarization vector $\hat{\mathbf{e}}$, neglecting the magnetic part. In quantum mechanics, the continuous X-ray wave, or more precisely the magnitude of the field, is quantized into photons with energy $E = \hbar \omega$ and momentum $\mathbf{p} = \hbar \mathbf{k}$ with $\hbar = h/(2\pi)$ and the Planck constant $h \approx 4.14 \times 10^{15}$ eVs.

Using the wave picture, the correct description for the propagation of a known X-ray wavefront Ψ from one point $\mathbf{r}_0$ to another point $\mathbf{r}_1$ in free space depends on the relation between the X-ray wavelength λ, the dimension a of the sample detail, and the propagation distance R. In general, a distinction is made between the near-field (i.e. Fresnel) regime valid if $R \approx a^2/\lambda$ and the far-field (i.e. Fraunhofer) regime valid if $R \gg a^2/\lambda$. For the imaging method (i.e. grating-based phase-contrast imaging) used in this work, the propagation of a known X-ray wavefront Ψ from one point $\mathbf{r}_0$ behind the sample to another point $\mathbf{r}_1$ in free space can be described by the Huygens-Fresnel principle [18]. It considers a wavefront as the superposition of spherical wavelets distributed on the wavefront. A comprehensive summary of the wavefront propagation has been given for example by Bech [19]. Here, we assume for simplification that the spherical wavefront $\Psi(x_0, y_0, z = 0)$ is purely propagating along the z-direction with $|\mathbf{k}| = k = 2\pi/\lambda_z$, starting from $z = 0$. Moreover that we are only interested in the modulation of the amplitude and the phase of the spherical wavefront $\Psi(x, y, z)$ in a small area close to the origin, i.e. $x, y \ll z$. The resulting wavefront at $z = d$ can then be described by the summation over all individual spherical wavefronts (generated at $z = 0$), which is given by the Fresnel diffraction integral [20]:

$$\Psi(x, y, d) = \frac{e^{ikd}}{i\lambda d} \int \int \Psi(x_0, y_0, z = 0) e^{\frac{ik}{2d}[(x-x_0)^2 + (y-y_0)^2]} \, \mathrm{d}x_0 \mathrm{d}y_0. \tag{2.4}$$

From (2.4) it can be seen that the propagation of a wavefront $\Psi(x, y, z = 0)$ that is known at $z = 0$ by a distance d can be considered as the convolution between $\Psi(x, y, z = 0)$ and the propagator function $h_d = \frac{e^{ikd}}{i\lambda d} e^{\frac{ik}{2d}[(x-x_0)^2 + (y-y_0)^2]}$. Since the convolution in real space transforms to a simple multiplication in Fourier space, fast calculation of the wave propagation problem is possible, which as been shown by [19].

2.4 X-ray interaction with matter

2.4.1 Introduction

An X-ray photon traveling through a specimen can penetrate the section of matter without interacting at all or it will interact with the atoms of the material and be absorbed or produce scattered radiation. The three interaction processes, photoelectric absorption,
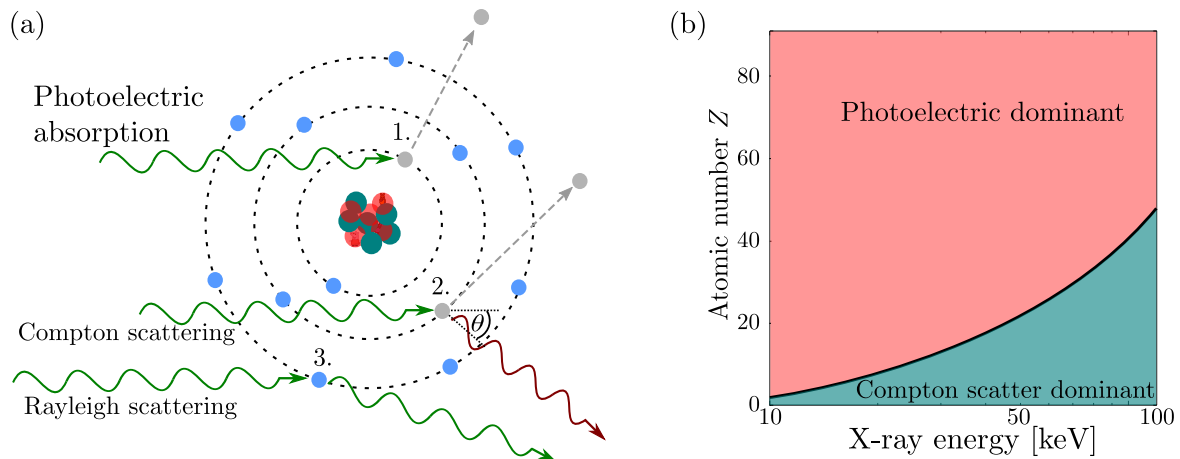
Figure 2.2: (a) Illustration of possible interaction processes of X-rays with matter showing 1. Photoelectric effect, 2. Compton scattering and 3. Rayleigh scattering. (b) Plot showing the dominant interaction process, photoelectric absorption or Compton scattering, for different materials and X-ray energies.

inelastic Compton scattering and elastic Rayleigh scattering, which are relevant for X-ray photons with an energy in the range of $10 - 120\,\text{keV}$, are illustrated in Fig. 2.2 (a). The probabilities of those interaction processes to occur, depend on the X-ray energy and the atomic number of the material, see Fig. 2.2 (b). In the following, first, the physical description of the absorption and scattering mechanisms, which are relevant in X-ray energy range used in this work, is given. After that, a quantitative description for a whole X-ray beam passing through a material will be given.

2.4.2 Physical description

2.4.2.1 Photoelectric Absorption

If the X-ray photon is absorbed, undergoing the photoelectric effect, it transfers all its energy to an electron of the atom. The electron is thereby ejected from the atomic shell with a kinetic energy E_{kin} given by:

$$E_{kin} = \hbar\omega - E_{bin} \tag{2.5}$$

with $\hbar\omega$ being the energy of the incident photon and E_{bin} the binding energy of the electron. From (2.5) it follows that, for the photoelectric absorption to occur, the energy of the X-ray photon needs to be higher than the binding energy of the electron. The cross section τ for a photoelectric absorption can be described approximately by

$$\tau \propto \frac{Z^n}{E^3}, \tag{2.6}$$

which increases with the atomic number Z to the power of $n = 3$ to 4 but also decreases strongly with an increasing X-ray energy E to the power of -3. However, a discontinuity in

the absorption cross section occurs when the X-ray energy just exceeds the binding energy of an electron in an atomic shell. At this point, the photoelectric absorption increases dramatically, because the X-rays are now able to transfer their energy and eject those electrons. These discontinuities are known as absorption-edge and are named after the orbit the electron is expelled from, for instance K-edge or L-edge. Since the photoelectric absorption leaves a vacant electron position in the atomic shell, electrons from higher shells can cascade and cause characteristic X-ray radiation to be emitted. This is most likely in high Z-materials such as iodine and CdTe, but is negligible in soft tissues.

2.4.2.2 Compton Scattering

Compton scattering describes the inelastic scattering between an X-ray photon with an energy E_i^γ and an electron of the atom with a binding energy $E_{bin}^e \ll E_i^\gamma$. During this process, the X-ray photon transfers a part of its momentum to the electron. As energy and momentum are conserved, the X-ray photon loses some of its energy and changes its direction of travel. The energy E_f^γ of the X-ray photon after Compton scattering can be calculated with the Klein-Nishina equation:

$$E_f^\gamma = \frac{E_i^\gamma}{1 + \frac{E_i^\gamma}{m_e c^2}(1 - \cos(\theta))}, \tag{2.7}$$

with the electron mass m_e, the scattering-angle θ and the speed of light c. Because Compton scattering occurs with quasi-free electrons (i.e. $E_{bin}^e \ll E_i^\gamma$), its probability σ to occur is proportional to the electron density of the material. Moreover within the energy range used in this work ($10 - 120\,\text{keV}$), it is nearly independent of the X-ray energy (at higher energies it decreases approximately as $1/E_i^\gamma$):

$$\sigma \propto \frac{Z}{(E_i^\gamma)^1}. \tag{2.8}$$

For soft tissues and X-ray energies above approx. $30\,\text{keV}$, Compton scattering is the dominant absorption mechanism and is also an effect that is responsible for a decrease in image quality. The image quality is degraded, because X-rays with high energies are mostly scattered in forward direction and thus decrease contrast and spatial resolution while back scattering events in the X-ray detector material add noise.

2.4.2.3 Rayleigh Scattering

The Rayleigh interaction is a coherent or elastic scattering process, in which the X-ray photon loses no energy, in contrast to the inelastic Compton scatter interaction process. In the classical picture, an incoming X-ray wavefront $|\Psi_i|$ forces the electrons to oscillate in the electric field with the same frequency as the incident X-ray wavefront which results in the emission of spherical wavefronts. If scattering appears at a continuous charge distribution $\varrho(r)$, the emitted wavefront $|\Psi_e|$ is given by

$$|\Psi_e| = -|\Psi_i|\, r_e \int \varrho(r) \frac{e^{i\,(\vec{k}_{out} - \vec{k}_{in})\vec{r}}}{R} d^3 r. \tag{2.9}$$
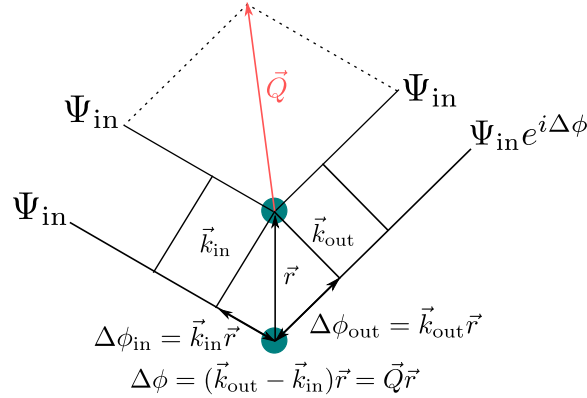
Figure 2.3: Illustration of the Rayleigh scattering, which goes along with a phase shift $\Delta\phi$.

Thus, a wavefront scattered at $\vec{r}$ has a phase shift $\Delta\phi$ at the point of observation that is quantified by

$$\Delta\phi = (\vec{k}_{out} - \vec{k}_{in})\,\vec{r} = \vec{Q}\,\vec{r}, \tag{2.10}$$

where $\vec{Q}$ is the scattering vector illustrated in Fig. 2.3. In general, electrons in an atom need to be considered as forced oscillators and their oscillation, with respect to the exciting wave, depends on the photon energy and is described by the atomic form factor

$$f(Q) = f^0(Q) + f'(E) + if''(E), \tag{2.11}$$

with $f^0(Q)$ quantifying the scatter strength form a single atom and $f'(E)$ and $f''(E)$ being the dispersion correction.

The probability σ_R for an X-ray photon with energy E_i^γ to be Rayleigh scattered is given by:

$$\sigma_R \propto \frac{Z^2}{(E_i^\gamma)^2}. \tag{2.12}$$

For low Z materials such as soft tissue (i.e. $Z \approx 7$), Rayleigh scattering is only a minor interaction process with a probability on the order of $5\,\%$ of all scattering events for X-ray energies above $70\,\mathrm{keV}$ and less than $12\,\%$ for X-ray energies at $30\,\mathrm{keV}$. However, the scattering angle increases as the X-ray energy decreases [21] and Rayleigh Scattering provides the general basis for the measurement procedures based on X-ray diffraction explained in section 2.6.

2.4.3 Quantitative description

So far, the three possible interaction processes of an X-ray photon with matter, i.e. photoelectric absorption, Compton- and Rayleigh scattering, are explained. However, in most cases, one is not interested in the interaction process of a single X-ray photon but in the
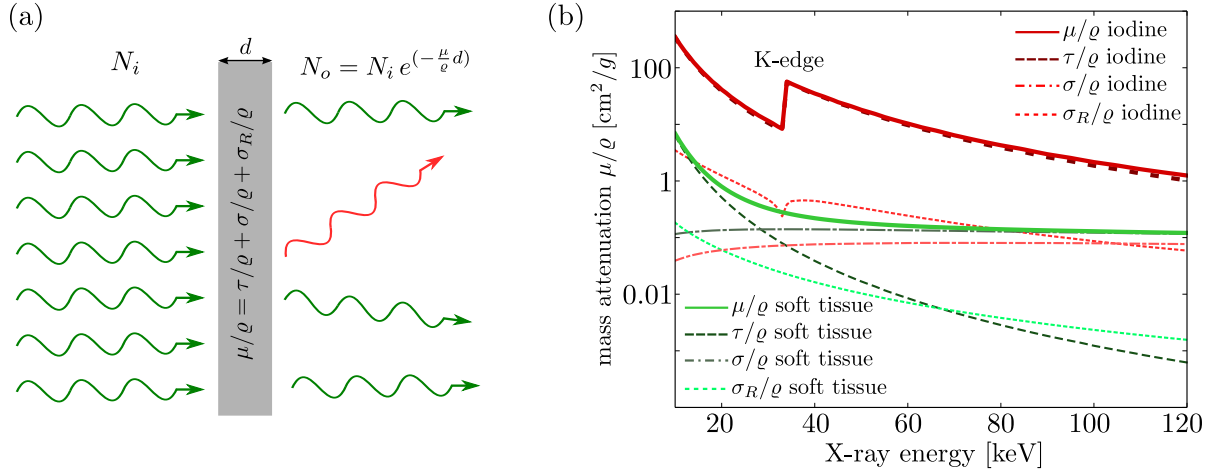
Figure 2.4: (a) Illustration of X-rays passing through a material described by the the linear attenuation coefficient μ including the probabilities for Photo effect τ, Compton scattering σ and Rayleigh scattering σ_R. If a number of N_i X-ray photons enter the material N_o photons exit the material without undergoing any interaction process (i.e. Photo effect, Compton effect or Rayleigh scattering). (b) Plot showing the total mass attenuation coefficient μ/ϱ and its individual components for soft tissue and iodine. It can be seen that the photo electric effect is dominant at low energies and high Z materials, while the Compton effect dominates at high energies and low Z materials and the Rayleigh scattering contributes only with a small fraction.

quantitative bulk attenuation of an X-ray beam due to absorption and scattering. For a quantitative description, it is useful to introduce the linear attenuation coefficient μ_x for an interaction process x with probability σ_x as:

$$\mu_x = \frac{N_A}{M} \varrho \, \sigma_x = \varrho_A \sigma_x, \tag{2.13}$$

with ϱ_A being the atomic number density of the material, N_A the Avogadro's constant, M the molar mass of the atom, and ϱ the density of the material. Figure 2.4 (a) illustrates a monochromatic X-ray beam, which consists initially of N_i photons, travelling through a material with thickness d. The amount of photons N_o that then exit the object without having interacted within the material, is given by the Beer-Lambert law:

$$N_o = N_i \, e^{-\mu_x d}. \tag{2.14}$$

As described above, different X-ray interaction processes are possible and the total attenuation coefficient μ of a material is given by the sum over the contribution of each individual process:

$$\mu = \varrho_A \sigma_{\text{sum}} = \varrho_A(\tau + \sigma + \sigma_R), \tag{2.15}$$

with τ, σ and σ_R being the cross sections for photoelectric absorption, Compton- and Rayleigh scattering, respectively. As explained above, the interaction probabilities depend

on the material and the X-ray energy, and therefore does also the linear attenuation coefficient. Obviously, the cross section (2.15) depends for a given material thickness on the number of atoms per volume. This can be overcome by normalizing the linear attenuation coefficient to the density ϱ of the material:

$$\mu_m = \frac{\mu}{\varrho},\tag{2.16}$$

which is commonly known as the mass-attenuation coefficient. In Fig.2.4 (b) the mass-attenuation and its components are shown for soft tissue and iodine. As can be seen, in soft tissue with low atomic number Z, Compton scattering exceeds photoelectric absorption at energies above 30 keV. Also, Rayleigh scattering can not be neglected for energies below 20 keV, where it is stronger than Compton scattering. For iodine, photoelectric absorption dominates over the whole energy range, and Rayleigh scattering exceeds Compton scattering up to about 100 keV. Moreover, the K-edge discontinuity at 33.2 keV is clearly visible.

2.5 X-ray detectors

2.5.1 Introduction

X-ray detectors are devices, which record the spatial intensity distribution and (or) the energy spectrum of an X-ray beam or even the position and the energy of individual X-ray photons. Position sensitive detectors are referred to as 'imaging' detectors. Over the last century, a great variety of imaging detectors has been developed, starting around 1890 with photographic plates and photographic films for radiographic images. However, the major breakthrough has been made when the first digital solid-state detector, the Charge Coupled Devices (CCDs), became available in the early 1970s. This new kind of detector lead to a revolution in X-ray imaging and made today's common imaging modalities, first and foremost the 3-D computed tomography, possible.

This chapter introduces first some of the terms that are used for the detector characterisation, summarizes the principles of image acquisition and readout of the most important solid-state detector types, used in X-ray imaging, and highlights main advantages and drawbacks. More details can be found in [22–25].

Glossary

Some of the terms that are used in the sections about detectors and their characterisation are first introduced in the following:

Spatial resolution and MTF: The spatial resolution is related to the smallest object feature that can be imaged with the detector. Without geometrical magnification, the perfect spatial resolution is given by the size of the detector pixel. In practice, the resolution is lowered because of an introduced unsharpness due to charge sharing or a low fill factor, among others. The actual resolution is often quantified and described by the modulation-transfer-function (MTF) of the detector [22]. Note, the experimental setup brings also physical sources of unsharpness, for instance an extended focal spot of the X-ray source, which add to the over all unsharpness and need to be respected. For example, if the extended focal spot is the main source of unsharpness, choosing a detecor with a smaller pixel size might not increase the real resolution of the setup.

Sensitivity: The sensitivity of an X-ray detector is defined by the amount of charge, which is generated (before amplification), per incident X-ray photon with a given energy. It depends on the X-ray absorption efficiency and the efficiency of the process to convert X-ray energy to electrical charges. A high sensitivity allows to detect also X-ray photons with low energies, which otherwise would be missed due to the presence of noise.

Fill factor: The fill factor is defined as the ratio between the active area of the detector, which is actually sensitive to X-rays, and the X-ray insensitive area. A fill factor of 1 or 100 % implies that there is no area on the detector, which is insensitive to light. Detectors with a low fill factor are less sensitive to X-rays and thus require a

longer exposure time to deliver the same image quality than a detector with a high fill factor. Also the spatial resolution can be decreased by a low fill factor.

Dynamic range: Simply speaking, for imaging detectors, the dynamic range can be defined as the ratio between maximal signal and the minimal signal (above noise) that can be detected. A high dynamic range makes it possible to measure intensity differences without saturating the detector and to detect low contrast features at the same time. The theoretically maximum dynamic range of a detector is limited by the bit depth per pixel that relates to the number of grey values that can be recorded. For example, a detector with a dynamic range of 16 bit could theoretically distinguish 65536 gray values, with 20 bit one could distinguish 1048576. However, in practice the usable dynamic range is limited by the presence of noise and potentially by the precision of the analogue-to-digital converter, in particular for integrating detectors.

Linearity: It is important that a pixel responses identically for different incident X-ray fluxes or intensities in order to obtain the same measurement results. This is described by the linearity of a detector. Simply speaking, a linear detector measures twice the intensity when X-ray current is doubled.

Uniformity: In order to achieve a homogeneous image, all of the detector pixels need to respond identically to the applied radiation. The uniformity of a detector describes the variance of the sensitivity over the entire area of the detector, due to gain and offset differences. The variances in the X-ray images because of a varying sensitivity is referred to as fixed-pattern noise. A simple method to correct for inhomogeneities is to record the detector response without a sample and use it for a correction mask. For detectors with a linear response, it is sufficient to acquire two masks, without and with radiation to correct the offset and gain variances. For detectors with a non-linear response, images over a whole range of intensities need to be acquired and a non-linear fit is needed for each element to obtain the correction coefficients.

Charge sharing: When an X-ray interacts with the sensor material, charge clouds are created with an initial width equal to its propagation length of the charge (for example: $10\,\mu$m at $40\,$keV [26, 27]). The charge clouds propagate towards the electrodes and diffuse according to the diffusion coefficients which goes along with an increase in volume. If the charge crosses the boundary of the physical pixel, it is shared between neighbouring pixels. This effect reduces both, the spatial- and energy resolution of the detector.

2.5.2 Classification of X-ray detectors

Solid-state X-ray detectors can be classified into categories according to the conversion process of the incident X-ray photons into electronic charges:

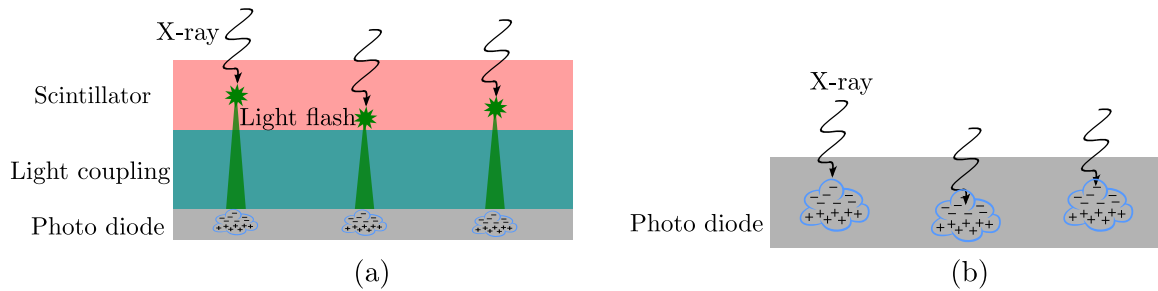- direct detection,

- indirect detection,

Figure 2.5: (a) Principle of an indirect X-ray detector. The scintillator converts the energy of the X-ray photons into a flash of visible or ultraviolet light. The light is subsequently absorbed in the semiconductor sensor (the photo-diode) coupled to the scintillator. (b) The direct X-ray detector immediately absorbs the X-rays in the semiconductor material.

and further according to the way this charge is measured:

- energy integrating detectors,
- photon counting detectors.

The main differences between those detectors will be explained in the following.

Indirect and direct X-ray Detectors

The terms 'indirect' and 'direct' X-ray detector are related to the way the X-ray photons are converted into electric charges. A schematic of the two principles is shown in Fig. 2.5. Indirect detectors are equipped with a scintillator material, for instance CsI(Tl) or NaI(Tl), to first convert the energy of the X-ray photon into a flash of ultraviolet or visible light. Those photons are subsequently converted into electric charge by a semiconductor sensor, i.e. a photo diode. Direct detectors, on the other hand, skip the X-ray conversion into visible light and directly convert it into an electric charge by absorption of the X-ray photon within the semiconductor sensor, which is directly exposed to the x-ray beam. The indirect method has the advantage that the X-ray photon conversion can be optimized relatively independent from the electrical charge creation. The efficiency of a scintillator material to convert the energy of an X-ray photon into visible light depends primarily on its physical parameters, such as thickness, chemical composition, and particle size. This allows, within certain boundaries, to optimize the scintillator to operate best over a preferred energy range and, in particular also for high X-ray energies even above 100 keV. Beside the coverage of a wide energy range, other advantages are a larger dynamic range and the benefit that the semiconductor material is protected against radiation damage caused by the high-energy X-ray photons. The main drawbacks using a scintillator, depending on the material and the X-ray energy, are the lower spatial resolution, the relatively long conversion time and the afterglow effect. Since the generated light flash spreads in every direction within a scintillator and because of additional internal scattering events, the spatial resolution of an indirect detector is limited. Further, there is a performance trade-off between spatial resolution and X-ray sensitivity:

An increase in thickness of the scintillator results in a higher absorption efficiency, but also increases the light spread resulting in an impaired spatial resolution. For a typical scintiallator thickness, an individual X-ray photon generates a light spot with a diameter of about $100\,\mu$m, which results in a spatial resolution of about 10 line pairs per millimeter, while for a thin scintillator $30\,\mu$m are possible. The performance of an indirect detector depends often on the technique to couple the light flash from the scintillator onto the light sensor. The main techniques are either to directly coat the sensor on the scintillator or to use fibre optic taper. The finite conversion time and the afterglow often limit both the maximal X-ray flux and acquisition frequency. For example, for successful use in clinical computed tomography, a dense ceramic material needs to be applied to suppress the afterglow. Further, indirect detectors typically provide a poor energy resolution since the energy response of a scintillator is not linear, due to the noisy absorption-emission process and the low spatial resolution.

Direct detectors on the other hand provide a better spatial resolution and sensitivity, highly contrasted images, and a mostly linear energy response. However, they typically provide a smaller active area. Moreover, as mostly silicon was used for the semiconductor sensor material so far, the detection efficiency for X-rays above $20\,$keV was low. Nevertheless, developments in recent years made it possible to nowadays manufacture larger crystals of high-Z semiconductor materials, such as GaAs or CdTe with very high purity and structure quality as required for detector-grade material. Therefore, directly converting detectors being limited too low X-ray energies could be overcome, and photon energies well above $100\,$keV are efficiently detected.

Energy Integrating and Photon-Counting Detectors

Energy integrating detectors, as their name suggests, continuously sum up the charge gathered from the semiconductor sensor material during the integration time over the entire incident spectrum. Because there is no processing time needed between subsequent photons, integrating devices can basically handle an unlimited amount of flux and there is no minimum detectable photon energy, of course provided that the photon is first absorbed in the sensor. Drawbacks arise from the fact that each absorbed X-ray or light photon generates an amount of charge carriers proportional to its energy. This in turn leads to the issue that a photon with lower energy contributes less to the integrated signal than a photon with higher energy. Therefore, integrating detectors underestimate the contribution of lower energy photons, which actually carry a higher contrast and additional effects, for instance beam hardening, even worsen the situation. Further, integrating detectors accumulate not only the charge generated by the absorbed photon, but also the thermally generated charge carriers, commonly known as dark current, which manifests in additional noise. This is in particular problematic in cases with low X-ray flux and low energy photons. Additional electronic noise generated during signal amplification and readout, accumulates to the overall noise and increases with increasing frame rates. Thus, for an optimal operation of an integrating detector, a trade-off between the total integration time and the readout speed needs to be found, which depends on the energy and the intensity of the X-ray beam. Therefore, since the early 90s, detectors with photon-counting ability have been developed to overcome the mentioned drawbacks

of the integrating detectors. This kind of detector processes and counts each individual X-ray photon. The detailed concept of photon-counting detectors and their advantages and disadvantages will be described after an introduction to the most important energy integrating detector types.

Note that the given classification of detectors into direct/indirect and integrating/photon-counting detectors is more or less independent from each other. For example, an integrating CCD detector can be equipped with either a directly or — more commonly — an indirectly conversive sensor.

2.5.3 Integrating detectors | CCD, CMOS and Flat Panel

Detectors made from charge coupled devices (CCD) and complimentary metal oxide semi-conductor (CMOS) detectors have both been around since the 70s. CCD detectors started their triumphal procession soon after their invention by W. Boyle and G. Smith (2009 Nobel Prize Winners) at the Bell Laboratories, USA. While they can be found nowadays in almost every electronic imaging system, CMOS detectors have always lagged behind due to the semiconductor technology, which at that time was difficult to manufacture. However, even though CCDs were the first semiconductor detectors with a reasonable good fill factor, sensitivity and spatial resolution, CMOS detectors have always been a potential and fast developing alternative, because of the CCDs disadvantages such as high cost, higher power consumption and complex support electronics. Since the early 90s, when CMOS detectors became commercially available, the decision between the one or the other detector type was mainly determined by a trade-off between the good image quality of the CCDs and the lower price and power consumption of the CMOS detectors. Nowadays, improved CMOS architectures nearly overcome the early weaknesses, mainly noise and sensitivity, resulting in almost the same image quality as with CCD sensors. In addition, CMOS detectors have the advantage to be manufactured with a nowadays well established manufacturing process also used for many other semiconductor devices, a in general smaller device size and much lower power consumption. This for instance makes CMOS sensors, in combination with lower costs, suitable for high-volume consumers and mobile applications.

In the following sections, the technology principles for image acquisition and readout, as well as the advantages and disadvantages of CCDs compared to CMOS detectors will be highlighted.

2.5.3.1 Integrating Detectors: CCD

A schematic cross section of a typical CCD pixel, which was first theoretically and experimentally described in [28, 29], can be seen as buried-channel metal oxide semiconductor (MOS) capacitor [30] and is shown in Fig. 2.6 (a). It consists of a thick p-type silicon substrate, a smaller n-type silicon layer, a thin silicon dioxide layer and a metal electrode. A positive voltage, which is applied to the top electrode, enlarges the depletion region in the p–n junction and forms a potential well below the silicon dioxide layer. When photons are absorbed in the depletion region, an amount of electron-hole pairs is generated that is proportional to the energy of the absorbed photons. Because of the applied voltage, the
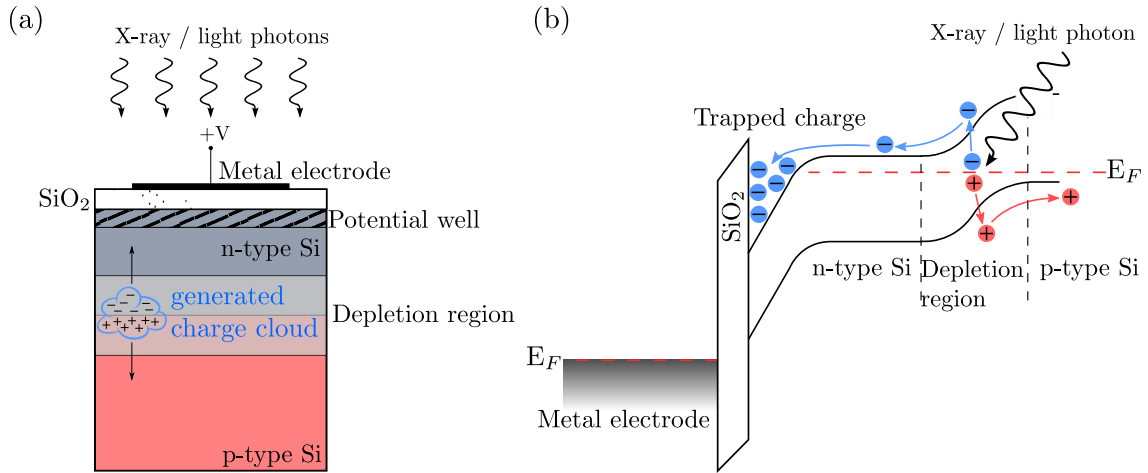
Figure 2.6: (a) Sketch of a CCD pixel. The applied voltage generates a potential well just below the SiO$_2$ insulator. The photons are absorbed in the depletion region generating charge carriers proportional to the energy of the photon. The electrons drift upwards to the n-type silicon and get trapped in the potential well. (b) Band structure model of the pixel.

holes drift downwards to the p-type silicon, where they recombine. The electrons travel upwards through the n-type silicon and get trapped in the potential well, as depicted in the band structure schematic given in Fig. 2.6 (b). The total amount of trapped charges is thus proportional to the number and the energy of the light absorbed by the pixel. At the end of the exposure time the trapped charge is transferred out of the CCD and is converted with an analog-digital-converter (ADC) into a corresponding digital signal. The readout procedure, which is illustrated in Fig. 2.7 (a) to (e), goes as follows:

(a) When the integration time has elapsed, the potential well of a certain pixel denoted by pixel 1, contains an amount of charge, which is proportional to the incident light, as described above. (b) The first step of the readout process is to transfer the charge of pixel 1 into the adjacent pixel 2 by forming an equally deep well by increasing the applied voltage of pixel 2. After this step, pixel 1 and pixel 2 share the charge equally (c). In the next step, the height of the well in pixel 1 is decreased, by decreasing the applied voltage. During this step, the charge in pixel 1 'swaps' completely into pixel 2 (d) and (e), respectively. By repeating those steps, the charge 'flows' from pixel to pixel towards the external readout register, which transports the charge to the ADC. Note, that the readout needs to be repeated consecutively for each pixel row, while all other pixels are in a 'wait state'. During this wait time, the pixels would still integrate the charge that meanwhile still beeing generated by absorbed photons. The easiest way to avoid this issue is to close a mechanical shutter during the readout period, which prevents the CCD from being exposed to the incident light.
The main advantages of CCD detectors are their sensitivity, the large dynamic range and the linear response. A great benefit of the read-out concept arises from the fact that
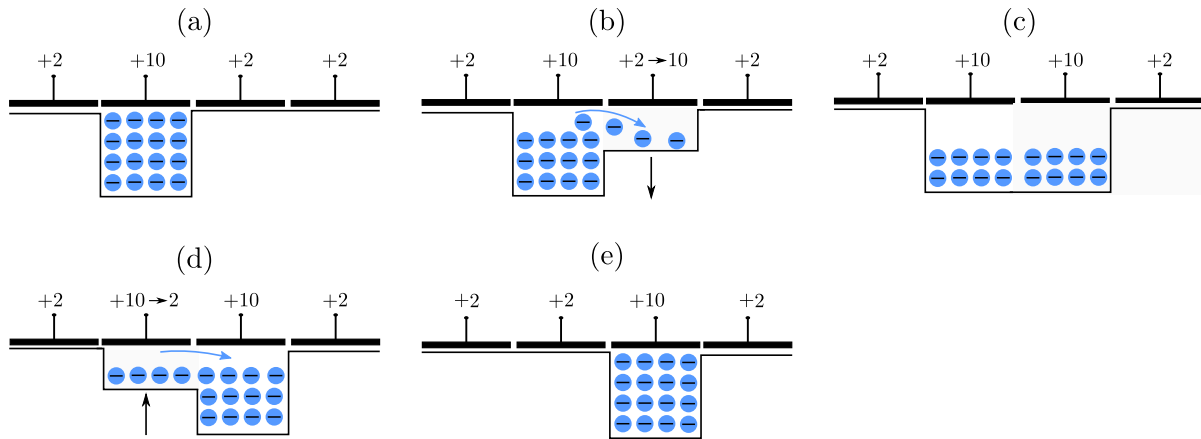
Figure 2.7: Illustration of the readout process from a CCD. (a) Initially the electrons are trapped in the potential well of one pixel. (b) Increasing the applied voltage of the adjacent pixel enlarged the corresponding potential well and the electrons start to spill over. (c) The electrons are equally distributed between both pixels. (d) Decreasing the applied voltage of the starting pixel lowers its potential well causing the remaining electrons to swap into the second pixel. (e) All electrons moved by one pixel.

the charge transport takes place below the light-sensitive area of the pixel, and that no light insensitive components are needed, beside the small metal electrodes. This leads to an extremely high fill factor, which can be close to 100 % for some devices. Further, since no complicated bulky processing components need to be manufactured onto the pixel, it is possible to make the physical size of a CCD pixel extremely small with edge lengths down to only $1\,\mu$m. Drawbacks of the charge beeing transferred from pixel to pixel are the limited frame rate, the complex clocking concept and the high operational power consumption. Moreover, one defect pixel can lead to entire non-functional rows or columns. Further, each charge transfer goes along with some losses, due to leakage, and adds noise to the signal. Therefore, the image quality varies across the image, since the rows of pixels that are closest to the readout register undergo fewer transfers than those on the opposite side of the array. This fact and the low readout speed limits the practical size of CCD detectors to about 1 to maximal 8 cm across. Larger active areas are obtained by combining several chips to one larger grid. Another drawback of the concept is known as 'blooming'; it happens if the potential well is completely filled and electrons start to overflow into wells from the neighbouring pixels. This typically happens, if strong absorption differences are present in the object, and pixels in the bright regions become saturated during the exposure time. Since one overflowing pixel well can affect many pixels in its neighbourhood, this can result in saturation of an entire area. Different concepts exist to avoid the blooming effect, but all of them involve with a decrease of the fill factor and thus a lower sensitivity.
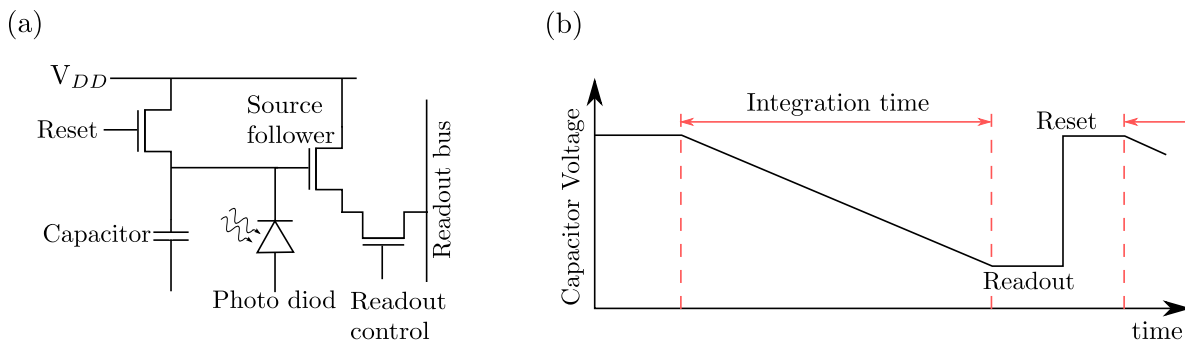
(a)

(b)

Figure 2.8: (a) Wiring diagram of a three-transistor CMOS pixel. The current, which is generated in the photo diode due to the absorption of X-ray photons, discharges (or charges) the capacitor during the integration time. The rate of discharging/charging is proportional to the amount of generated charge carriers and thus, to the energy of the X-ray photon. (b) Basic diagram of the capacitor voltage before, during and after the integration time. When the integration time has elapsed, the remaining voltage is read out and digitized.

2.5.3.2 Integrating Detectors: CMOS

As in the case of CCD detectors, each complimentary metal oxide semiconductor (CMOS) pixel converts the photons into electric charge using a semiconductor sensor. The actual difference between the two detector types is the way how the charge is produced and how it is converted into a digital value that is proportional to the amount of absorbed light. As explained above, a CCD pixel absorbs the photon in a biased p-n junction, which creates a potential well to accumulate the charge during the integration period. Subsequently the charge is read out and externally converted into a digital signal by an analog-to-digital converter. On the other hand, the CMOS detector employs a photo diode, a capacitor, and a number of at least three MOSFET [1] transistors for controlling the acquisition and read-out, as shown in the electrical circuit given in Fig. 2.8 (a). The working principle of a CMOS detector is shown in Fig. 2.8 (b).

Before starting the acquisition, the capacitor is precharged to a certain reset voltage. During the integration time, the capacitor is discharged by the current that is caused in the photo diode due to the generation of charge carriers by incident photons. Note that it is also possible to charge the capacitor during integration time, instead of discharging it. At the end of the integration time, the charge remaining in the capacitor is read out, amplified and digitized. For the amplification and digitization of the charge, two types of concepts exist: the passive-pixel and the active-pixel concept, which are both illustrated in Fig. 2.9 (a) and (b), respectively. The passive-pixel detector only has charge amplifiers at the bottom of each pixel column. The pixels of active-pixel detectors, on the other hand, individually contain their own dedicated charge amplifier.

In contrast to CCD detectors, CMOS devices do not read out the data by shifting it from pixel to pixel, but via dedicated data lines, which are also shown in Fig. 2.9. Each pixel

---

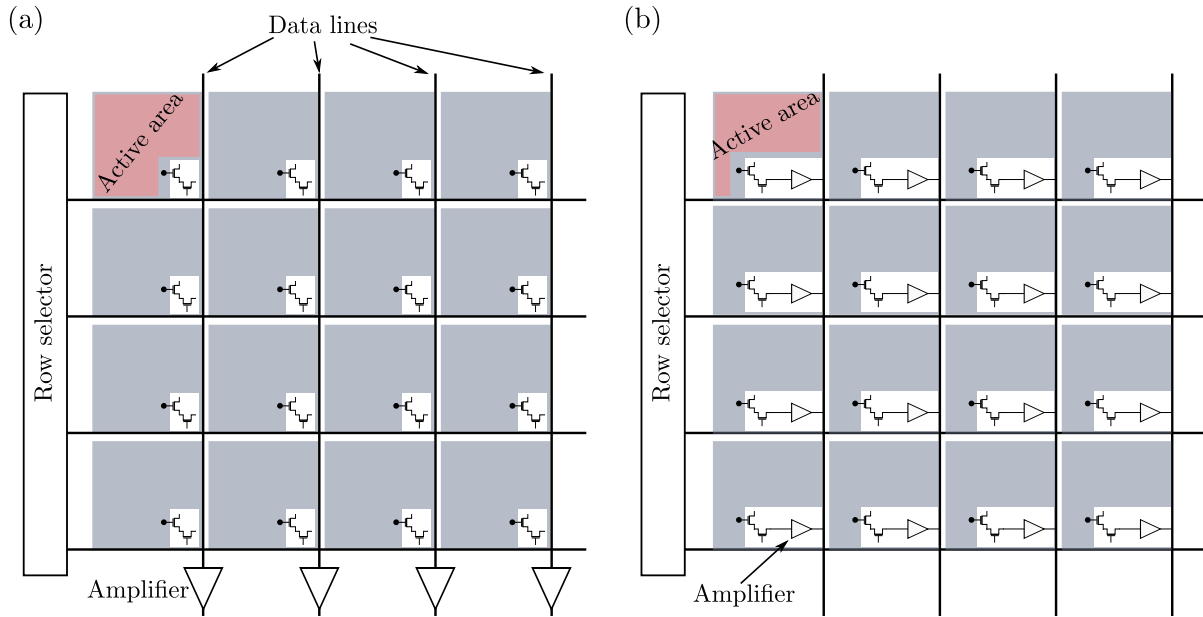[1]metal-oxide-semiconductor field-effect transistor

Figure 2.9: (a) Basic concept of a passive CMOS detector, where each data line contains an amplifier common for the whole pixel column. (b) Basic concept of an active CMOS detector, where each pixel contains its own amplifier. An active CMOS detector has a lower fill factor, because the area that is sensitive to X-ray photons is smaller due to the additional components, that are not sensitive to light.

column contains one data line to which the respective pixels are connected via switching transistors that control the data read out. Row selectors are used to control the switching transistor for a specific row of pixels to transfer the data to the data line. Thus, the full image is read out sequentially, row by row. However, it is also possible to read out only parts of the detector, which allows much higher frame rates as compared to the CCD detectors. Another transistor typically named 'source follower' prevents discharge during the readout, which makes it possible to re-read the same pixel several times. In this concept a certain area of the sensor is occupied by the transistors as well as the control and data lines, which are all not sensitive to the photons. This in turn leads to the typically lower fill factors and a lower sensitivity compared to CCDs. Although, micro-lenses can be used to partially compensate this effect and improve the sensitivity, CMOS detectors remain still less sensitive compared to most CCDs. Note that in the new concept of hybrid-pixel detectors, which is explained in section 2.5.5, the conversion process in the sensor and the subsequent charge processing are separated. Thus the issue of a limited fill factor, but at the cost of a more complicated manufacturing process, resulting in different issues and drawbacks. Further, since in the active CMOS detector the capacitor and amplifier of each pixel differs in behaviour because of component tolerances, active CMOS pixel arrays tend to be less uniform than those of a CCD detector. Hereby fixed pattern noise is introduced due to the mismatch between the pixels. Beside the advantage of low power consumption of a CMOS detector compared to a CCD, they also do not suffer from blooming or the high losses during the charge transfer, because the data is directly
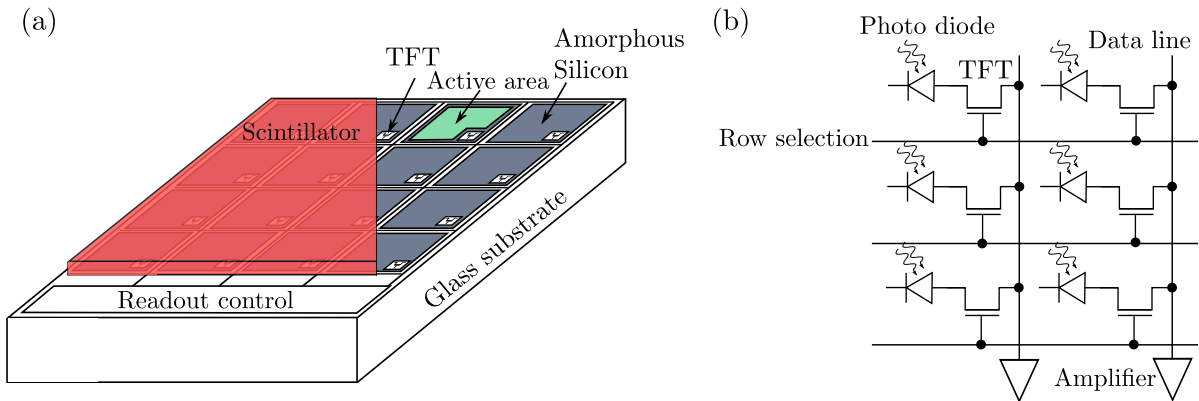
Figure 2.10: (a) Sketch of an indirect Flat Panel detector. The scintillator converts the energy of the X-ray photon into visible light, which is subsequently absorbed in the active area (green) of the photo-diode and stored in the capacitor of the pixel. The thin-film-transistor (TFT) acts as a switch to transfer the generated electrons to the data line. (b) Wiring diagram from a Flat Panel pixel. The row of pixels, which shall be read out is selected by the 'Row selection' line.

transferred out of the pixel array. Lastly, since the CMOS technology is well established in industry, the manufacturing costs of a CMOS detector are much lower compared to CCDs.

2.5.3.3 Integrating Detectors: Flat Panel

Because it was not possible with the CCD technology to produce affordable large-area image sensors, and because both CCD and CMOS detectors are susceptible to radiation damage, they were for a long time not suitable for medical imaging. This changed in the early 90s, when the first flat-panel detectors became commercially available. Like CCD and CMOS detectors, flat-panel devices convert photons into electric charges using a semiconductor material. However, they make use of the cheap and uncomplicated liquid crystal display (LCD) technology, which already lead to the replacement of monitors based on cathode ray tubes. Based on simple glass substrates, flat-panel detectors utilize radiation-hard amorphous sensor materials. The choke of materials is suitable to produce large active areas of several million pixels and sizes exceeding $40 \times 40 \, \text{cm}^2$, at comparatively low costs. These features made those devices interesting for x-ray imaging in medical applications, for instance radiography, mammography, angiography, and fluoroscopy, as well as for non-destructive testing. Because of their importance in industrial and medical disciplines, the main concept and benefits of indirect flat-panel devices are highlighted in the following. The cross section of an indirect flat-panel device is schematically shown in Fig. 2.10 (a).

Note that the distinct concepts for direct and indirect conversion, exist also for this kind of detector. The indirect flat-panel detector is more common and uses typically structured CsI(Tl) or $Gd_2O_2S(Tb)$ (Gadox) as scintillator material to convert the X-ray photons into visible light. The direct flat panel typically has a sensor made from amorphous selenium.

The indirect flat-panel detector converts the visible light photons from the scintillator into electron-hole pairs, using a sensor typically made of amorphous silicon (a-Si:H). The amorphous silicon has the advantage that it is cheap and it can be manufactured into thin layers while still maintaining a high absorption efficiency. Moreover it is radiation hard and allows to produce electrical components such as the thin-film transistors (TFTs), which were developed in the early 60s by Paul K. Weimer in the RCA Laboratories [31]. The acquisition and read-out procedure is similar to the concept of a CMOS detector described above. A schematic of the electric circuit for a TFT-based pixel structure is shown in Fig. 2.10 (b). In a flat-panel pixel, the sensor, which is basically a photo diode, simultaneously acts as a capacitor. Before acquisition, the capacitor is precharged and gets partially discharged during integration time, due to the collected electron-hole pairs. When the integration time has elapsed, the remaining charge is read out by switching the TFT to the state in which it lets the charge carriers pass to the readout bus. This causes the charge to be transferred via the data line to the readout electronics, which measures the amount of discharge and converts the analog signal into a digital signal. As can be seen from Fig. 2.10 (a), the fill factor of the pixel is lowered due to the additional components, in particular the thin-film-transistor and the data and control lines, as it is the case for the CMOS detectors. The drawbacks of amorphous silicon compared to single-crystal silicon, as it is used in CCDs and CMOS detectors, arise from the 100 to 1000 times higher amount of defects. Those reduce the mobility of the charge carriers and thus the switching speed of the TFT transistor, ultimately limiting the maximal frame rate of the detector. In addition, the defects come along with a complicated lag and offset behaviour, which makes a careful offset calibration and correction essential to obtain a homogeneous image. The main advantages of flat-panel detectors are the comparatively low costs, the possible large field of view, the high dynamic range with a good signal-to-noise ratio (SNR) and the maintenance of a good image quality over a wide range of X-ray energies.

2.5.4 Photon-counting detector

To overcome the drawbacks of integrating detectors, in particular the underestimation of low-energy photons and the noise accumulation during integration and read out, a new concept of detectors was developed: the single-photon–counting detector. The basic principle of a photon-counting detector is to detect, process, and count each X-ray photon individually. A schematic of a pixel from a the typical photon-counting concept is shown in Fig. 2.11 (a). The X-ray or visible-light photon is absorbed in the photo-diode causes the generation of a charge pulse proportional to the energy of the photon, which is fed into a pulse shaper. In order to reduce the electronic noise, the pulse shaper converts the narrow charge pulse into a broad voltage or current pulse, which can be processed by the subsequent electronics. The peak height of the shaped signal is ideally still directly proportional to the energy of the incident photon. Note that the pulse-shaper output delivers an analog signal over time that contains not only the actual signal, but also the noise-signal arising from thermal excitation of charge carriers. A subsequent discriminator provides a binary signal for each pulse above an adjustable threshold level, which incre-
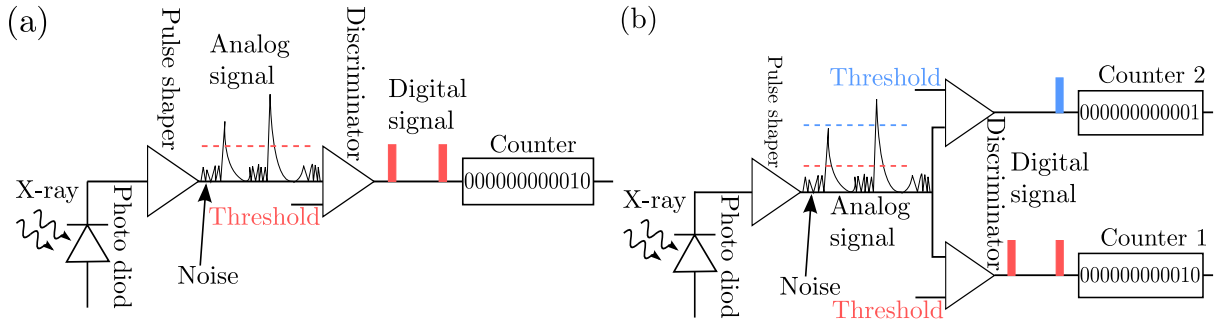
Figure 2.11: (a) Sketch of the photon-counting concept. The charge package generated in the photo diode is fed into a pulse shaper. The discriminator converts each analog pulse above an adjustable threshold into a digital signal, which increments the counter. (b) Concept of the energy discriminating photon-counting detector. Each counter only counts the analog pulses above the threshold of the corresponding counter. The difference between the counter values gives the number of analog pulses between the two thresholds. Thus, after a threshold-to-energy calibration the number of X-ray photons within the corresponding energy window —defined by the two individual thresholds— of the X-ray spectrum can be measured.

ments a digital counter. Thus, if the threshold value of the discriminator is set just above the noise level of the photo diode and the electronics, only the X-ray signal generates a binary pulse while the noise signal is effectively removed. This in turn leads to a noise behaviour that is only quantum-limited by the statistical nature of the impinging photons and the detection mechanism itself. When the counting time has elapsed, the counters are read out. Thus, instead of delivering a digitized voltage as a relative value for the amount of energy deposited by the photons that have been detected, as it is the case for integrating detectors, photon-counting detectors de facto deliver the actual number of photons with energies above the set threshold that have been absorbed. In the case of photon-counting detectors, the minimum detectable photon energy is limited by the electronic noise, and the dynamic range is determined by the number of counter bits. Since the X-ray photons are counted, each photon contributes equally regardless of its energy. Thus, the low-energy photons, which carry high contrast are not suppressed as in integrating detectors. Further, as described above, the pulse shaper delivers a broad voltage or current pulse, of which both the width as well as the peak amplitude are proportional to the amount of input charge carriers and therefore a measure of the energy of the X-ray photon.

Therefore, if multiple discriminators and counters are used in each pixel, it is possible to sort incoming X-ray photons based on their energy. This principle is shown in Fig. 2.11 (b). Each counter counts only the photons above the energy-threshold level of its corresponding discriminator, which is defined by the user. Thus, subtracting two counter values delivers the number of X-ray photons between the two threshold values and a prior energy calibration of the discriminator threshold makes it possible to perform energy discriminating measurements. Note that other energy discriminating photon-counting

concepts called time-over-threshold (TOT), for example realized in the Timepix detector [32], measure the width of the shaper-output pulse. Since this is also proportional to the input charge pulse, the energy of the X-ray photon can be determined.

The ability for classical-noise free and energy-resolved measurements has several benefits in clinical applications and imaging for industrial non-destructive testing [33, 34]. First, the improved spectral modelling and the narrower energy spectra, which is effectively measured in each energy bin allow for the reduction of beam hardening and metal artifacts [35–37]. An appropriate energy weighting of each individual X-ray photon can achieve an improved signal-to-noise ratio at lower dose [38, 39]. Further, it allows for quantitative imaging, material- or tissue type specific imaging, accurate K-edge imaging and simultaneous multi-agent imaging [40].

A major drawback of the photon-counting concept is that each charge package generated from the X-ray photons needs to be processed individually. This limits the maximal detectable photon flux, since two consecutive photons must not arrive within the processing time of the counting logic. In particular, the shaping time needed to generate a proper output pulse is in the order of about 100 ns. Therefore, if two photons hit the sensor within this shaping time, they cause to overlap actually separated output pulses. Consequently, the two photons are effectively counted as one, but with their energies superimposed. This is called pile-up effect and causes the photon counting to deviate from its linear behaviour. Therefore, for each detector system a characteristic time constant exists, called the 'dead time', which must separate two consequent photon hits in order for the events to be counted individually. Additionally, other electronic components also increase the dead time, which is then usually in the order of a few microseconds. Practically, the maximal detectable photon flux without pile-up effects and with correct count rate is in the order of 10^6 photons/(s mm^2) to 10^8 photons/(s mm^2) for most standard photon-counting detectors, depending on the physical pixel size and the actual dead-time. This is still too low for modern clinical CT sources, which deliver a high X-ray flux in the order of 10^9 photons/(s mm^2). Further, since each pixel contains its own readout chain, photon counting devices face the issue of a strong non-uniform pixel sensitivity due to component tolerances. This requires a work-intensive and complicated pixel equalization and calibration process. In addition, the large amount of components that is needed in each pixel for data processing restricts the minimal possible size of the pixel. Currently, the smallest pixels are in the order of $50 \times 50 \, \mu\text{m}^2$. The photon-counting concept can be manufactured with the standard CMOS technology, which was introduced in section 2.5.3.2. However, since the additional components i.e. pulse-shaper, discriminator, counter, as well as the readout and control lines are not sensitive to X-rays, the fill factors are typically not higher than about 80 %. An alternative concept is given in the form of a hybrid-pixel design, which will be highlighted in the following.

2.5.5 Hybrid-pixel detector

The cross section of a hybrid pixel device is shown in Fig. 2.12. The term 'hybrid' illustrates the fact that the sensor and the readout ASIC (Application-Specific Integrated Circuit) are two independent components that are physically and electronically connected
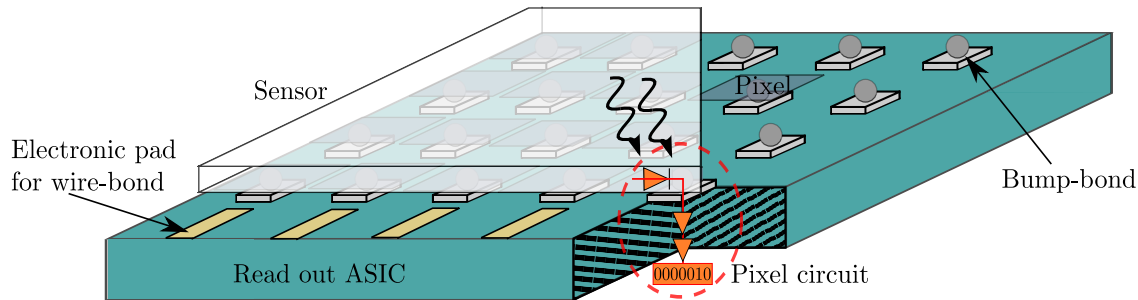
Figure 2.12: Cross section of a hybrid-pixel photon-counting detector. The sensor and the readout ASIC (Application-Specific Integrated Circuit) are separated, which allows an independent optimization. The sensor is physically and electronically connected to the ASIC via bump-bonds. The pads for the wire-bonds are used to transfer the data to the subsequent readout electronics like an FPGA or PC.

via bump bonds. The decoupling of the sensor from the readout ASIC has the advantages that the light-insensitive components do not affect the fill factor and sensitivity of the sensor, and that each component can be optimized independently. For instance, this concept allows, under certain conditions, that the same ASIC can be equipped with different semiconductor sensor materials such as Si, CdTe, GaAs, and Ge, depending on the energy range that the detector shall be operated in. In order to transfer the data (i.e. the counter values) from the ASIC to the data-processing unit (FPGA, PC, ...), the ASIC is connected to the read-out board via wire bonds. The data acquisition as such is similar to the acquisition process of the other solid-state detectors, which were described in this chapter. The X-ray photons are absorbed in the p-n junction of the sensor by the photo electric effect and the generated charge carriers drift along the electric field and, via the bump-bonds, to the readout ASIC. The data processing with amplification, pulse shaping, discriminating, and counting has already been described. When the exposure time has elapsed, the counter values, which represent the number of photons that have been absorbed, are read out. For this process, all counters from one pixel column are daisy-chained to form a large clocked shift-register. The counter values are then shifted to a dedicated read-out shift-register, which transfers the data via the wire bonds to the read-out board for further processing.

In chapter 3, the energy discriminating hybrid photon-counting pixel detector 'LAMBDA', which was used in this work, will be explained in more detail.

2.5.6 New detector concepts

New applications and radiation sources such as the free electron lasers (FEL), which deliver an enormous X-ray flux of 10^{12} photons/s within an ultrashort pulse of less than 1 ps, pose challenges to the current detector concepts. The combination of an extremely large dynamic range of up to 10^4 photons (12 keV) with single-photon resolution and extremely high frame rates brings the current concepts to its limits. Thus, new concepts like the Adaptive Gain Integrating Pixel Detector (AGIPD) [41] are currently being developed

in collaboration between the Deutsches Elektronen-Synchrotron (DESY) and the Conseil Europen pour la Recherche Nuclaire (CERN). This special kind of integrating detector uses the principle of automatic adaptive gain switching. It allows to expand the dynamic range of a charge-integrating detector while keeping the electronic noise below the Poisson limit, which is given by the number of detected photons. The concept balances the opposing requirements for obtaining single-photon sensitivity (i.e. a high gain and a low amplifier noise), on the one hand, and for a high dynamic range (i.e. a low gain), on the other hand, by employing a self-regulating, adaptive gain switching mechanism. During exposure, the generated charge is integrated on a capacitor as in the case of a regular CMOS detector. If the output of the amplifier and thus the maximal detectable charge reaches a certain level, additional capacitors are switched in, which effectively lowers the output of the amplifier. When the exposure time has elapsed, both the analog voltage from the capacitor as well as the digital information about the gain are read-out. With a prior channel-by-channel calibration, the number of photons absorbed in each channel can be reconstructed. This concept makes it possible to maintain a single-photon–counting resolution (in the first gain level) with a dynamic range of up to 10^4 photons per channel and a maximal frame rate of 4.5 MHz.

2.6 Grating-based X-ray phase imaging

2.6.1 Introduction

X-rays can provide an image of the inner structure of matter, if the outcome of the interaction processes (i.e. photoelectric absorption, Compton and Rayleigh scattering) is recorded with an appropriate position-sensitive X-ray detector. To do so, the number N_o of X-ray photons behind the specimen is measured in each pixel of the X-ray detector. Thereby a 'shadow image' of the inner structure is obtained. Further, if the number N_i of initial X-ray photons is known from measuring an image without specimen, the linear attenuation coefficient μ can be extracted from eq. (2.14). However, in particular if specimens with low Z values need to be measured, such as soft tissue, the attenuation of X-rays (i.e. the difference between N_o and N_i) can be very low. Therefore, it is very difficult or often impossible to obtain sufficient contrast in the attenuation image to distinguish different materials or tissues in the specimen. In those cases, it is often more efficient not to measure primarily the absorption of the X-ray photons, but their deflection caused by elastic Rayleigh scattering. This approach is typically known as phase-contrast imaging.

The following sections provide a concise description of this novel imaging modality. First, the physical principles are explained followed by a description of the technique of grating-based phase-contrast imaging.

2.6.2 Refractive index

For the understanding of grating-based differential phase-contrast imaging, it is appropriate to treat the X-rays as electromagnetic waves and consider the object to be a continuum characterized by its complex index of refraction

$$n = 1 - \delta + i\beta. \tag{2.17}$$

The physical effect of δ and β on an X-ray wavefront propagating in z-direction through the specimen can be seen in an easy manner, when applying (2.17) to the expression of a planar wave (2.3):

$$\Psi(\mathbf{r}) = \mathbf{E}_0 \, e^{in(\mathbf{k} \cdot \mathbf{r})} = \mathbf{E}_0 \, e^{i(1-\delta+i\beta)(\mathbf{k} \cdot \mathbf{r})} = \mathbf{E}_0 \, e^{i(1-\delta)(\mathbf{k} \cdot \mathbf{r})} \, e^{-\beta(\mathbf{k} \cdot \mathbf{r})}. \tag{2.18}$$

Obviously, equation (2.18) states, that β causes an attenuation of the X-ray wavefront which is related to the the linear absorption coefficient μ as given in (2.21b). Further, δ causes a phase-shift $\Delta\phi$ of the X-ray wavefront given by [42]

$$\Delta\phi(x) = \frac{2\pi}{\lambda} \int \delta(x, z) \, dz, \tag{2.19}$$

which is caused by the elastic Rayleigh scattering, as described in in section 2.4, With the microscopic atomic values, which are introduced in sec. 2.4, one can express the macroscopic index of refraction n by [17]:

$$n = 1 - \frac{r_0 \varrho_A \lambda^2}{2\pi} f = 1 - \frac{r_e \varrho_A \lambda^2}{2\pi} [f^0(Q) + f'(\lambda) + i f''(\lambda)], \quad (2.20)$$

where $f^0(Q)$ and the dispersion corrections $f'(E)$ and $f''(E)$ are quantifying the scatter strength, λ is the X-ray wavelength, $r_0 = 2.82 \times 10^{-15}$ m is the Thomson scattering length or classical electron radius, $\varrho_A = \varrho_M N_A / M$ is the atomic number density of the material containing the Avogadro number N_A, mass density ϱ_M and the molar mass M of the material. Far away from an absorption edge, $f'(\lambda)$ vanishes and in the limit of $Q \to 0$, i.e. all atoms scatter in phase, the atomic form factor equals the number of electrons in the atom, i.e. $f^0(Q) = Z$, which is assumed through out this thesis. From comparing (2.17) and (2.20) together with (2.15) and (2.18) it follows:

$$\delta = \frac{\lambda^2}{2\pi} \varrho_A r_0 Z, \quad (2.21a)$$

$$\beta = -\frac{\lambda}{4\pi} \varrho_A f'' = \frac{\lambda}{4\pi} \varrho_A \sigma_{\text{sum}} = \frac{\lambda}{4\pi} \mu. \quad (2.21b)$$

The phase shift (2.19) translates further into an angular deviation α of the X-ray beam given by:

$$\alpha(x) = \frac{\lambda}{2\pi} \frac{\partial \phi}{\partial x} = \frac{\partial}{\partial x} \int \delta(x, z) \, \mathrm{d}z, \quad (2.22)$$

as shown in Fig. 2.13.

Comparing (2.21a) with (2.21b) and (2.15) leads to the dependencies of δ and β on the X-ray energy and the atomic number:

$$\delta \propto \frac{Z}{E^2}, \quad \beta \propto \frac{Z^5}{E^{3\dots5}}. \quad (2.23)$$

From (2.23) it its obvious, that in particular for objects with low Z values and high X-ray energies, δ becomes much larger compared to β. Therefore, in cases where the measurement of the X-ray wavefront attenuation is too weak, the measurement of the wavefront phase-shift can still yield a strong difference and contrast. Further, as long as the linear absorption coefficient μ is dominated by the photo-electric absorption (i.e. $\mu \approx \tau$) the measurement of the phase-shift delivers complementary information, since δ is proportional to the electron density $\varrho_e = \varrho_A Z$ of the material and β only to the atomic number Z. A method to indirectly measure the wavefront phase shift, typically called grating-based phase-contrast imaging, is given in the following sections.

2.6.3 The grating interferometer

2.6.3.1 Introduction

As introduced in section 2.4.2.3 the coherent Rayleigh scattering leads to a phase-shift of the X-ray wavefront, which results in an angular deviation α of the beam. Therefore,
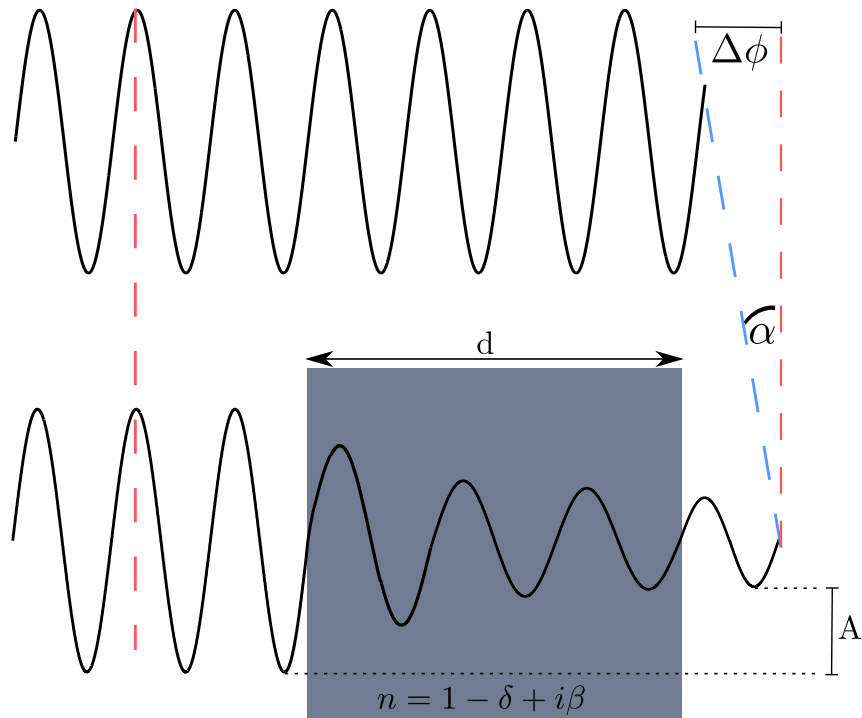
Figure 2.13: A wavefront that travels through an object characterized be the complex refractive index $n = 1 - \delta + i\beta$ experiences an attenuation A of the amplitude and phase shift $\Delta\phi$. The phase shift causes a change in propagation direction by an angle α.

measuring the angular deviation would allow to extract the amount of phase shift and consequently the electron density of the object. However, the typical angular deviation is in the order of micro degrees and thus, typically too small to be directly resolved with the pixels of the X-ray detector. One method to measure the angular deviation is the grating-based phase-contrast imaging modality. It makes use of the wave structure of X-rays and exploits a coherence effect, namely the Talbot effect, to translate the undetectable angular deviation α into a detectable shift of an interference pattern. In the following, the Talbot- and Lau-effect are described and followed by a description of the interferometer and the signal- and image-extraction processes.

The Talbot Effect

Placing a periodic structure, such as a grating with period p_1, into a plane and coherent light- or X-ray wavefront leads to a repeated self image of the periodic structure at certain distances d_T:

$$d_T = 2m\frac{p_1^2}{\lambda}, \tag{2.24}$$

with $m = 1, 2, 3, ...$ Because Sir Henry F. Talbot was the first to discover this effect with coherent light in 1836, the distances d_T are known as the Talbot lengths. The reason for
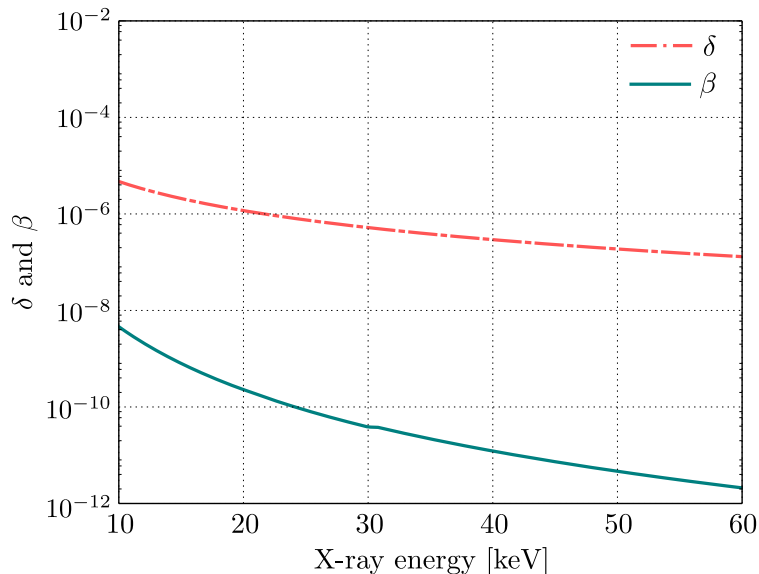
Figure 2.14: Calculated δ and β values for carbon as a function of the X-ray energy in the range from $10\,\text{keV}$ to $60\,\text{keV}$.

the self-image effect is the periodic distortion of the wavefront due the periodic structure placed in the X-ray beam. Since the X-ray beam is coherent, those periodic distortions interfere further downstream and form an interference pattern as shown in Fig. 2.15. Even though the self-image effect would in principle occur with any periodic structure in the beam that changes the phase or the amplitude of the X-ray wavefront, in the following only so called phase-gratings shall be considered that purely shift the phase but leave the amplitude unchanged. Further, only ideal gratings with a duty cycle of 0.5 (i.e. only half of the grating period introduces a phase shift while the other half does not) shall be considered. In practice, typically phase-gratings that introduce a π- or $\pi/2$-shift are used to generate self-images with period p_{self} at intermediate distances d_f [43], with

$$p_{\text{self}} = \frac{p_1}{\eta}, \tag{2.25a}$$

$$d_f = \frac{n}{2}\frac{p_{\text{self}}^2}{\lambda}. \tag{2.25b}$$

The distances d_f are known as fractional Talbot distance with $n = 1, 2, 3, ...$ and $\eta = 1$ for a $\pi/2$-shift grating and $\eta = 2$ for a π-shift grating, respectively. As (2.25a) and (2.25b) state, π-shift phase gratings generate self-images with half the period of the phase grating and with a (fractional) periodicity of $d_{f\pi} = 1/8\,d_T$. A binary or box shaped intensity pattern is generated at distances $d_{\text{bin},\pi} = b_\pi/16\,d_T$ with $b_\pi = 1, 3, 5, ...$ On the other hand, $\pi/2$-shift phase gratings produce self-images with the same period as the phase grating with a (fractional) periodicity of $d_f = 1/2\,d_T$ and a binary intensity pattern at distances $d_{\text{bin},\pi/2} = b_{\pi/2}/16\,d_T$ with $b_{\pi/2} = 2, 4, 6, ...$
How those Talbot carpets are used to measure the wavefront phase-shift within the sample

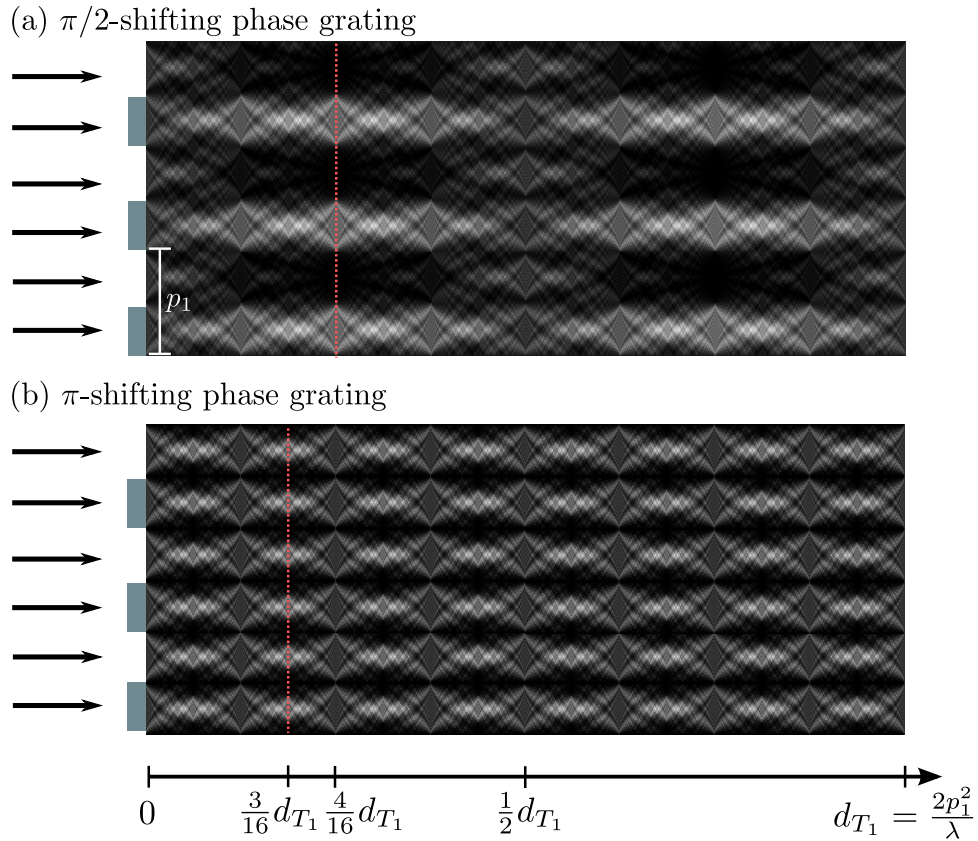(a) $\pi/2$-shifting phase grating

(b) π-shifting phase grating

Figure 2.15: Simulations of the intensity pattern called Talbot carpet that are generated behind phase gratings that introduce (a) a $\pi/2$-shift, and (b) a π-shift to the X-rays passing through the gratings, respectively. The red dashed lines indicate the distances where a binary intensity pattern can be observed. (Image adapted from [19])

is described in the next section.

Interferometer and Stepping Procedure

As described above, a periodic phase-shift grating referred to as G_1, which is placed in a coherent X-ray beam, generates a regular intensity pattern further downstream, with a lateral period p_{self} given by (2.25a), see Fig. 2.16(a), black dashed curve. If an object is placed just in front of the phase grating, the X-ray wavefront experiences a phase shift $\Delta\phi$ depending on the material properties given by (2.19). Consequently the beam is deflected by an angle α given by (2.22) which further translates to a lateral shift S of the intensity pattern given by:

$$S = \tan(\alpha)\, d \approx \alpha\, d. \tag{2.26}$$

Here, the small-angle approximation was used due to the small scattering angle α which is in the order of micro-degrees. Thus, measuring the lateral shift S makes it possible to extract the introduced spatial derivative of the phase shift $\Delta\phi$ by combining (2.26) and
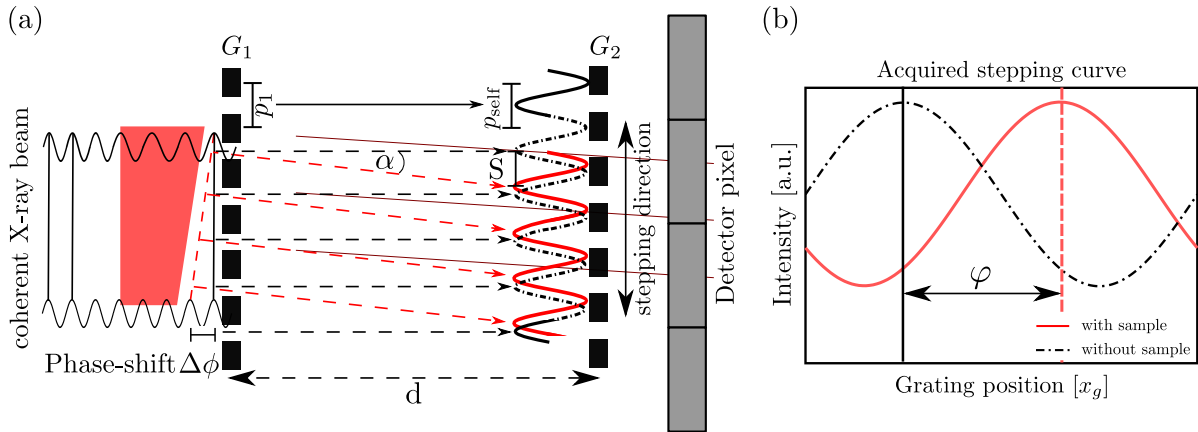
Figure 2.16: (a) Sketch of a Talbot interferometer consisting of a phase grating G_1 with period p_1 and an analyzer grating G_2 with period p_2 separated by a distance d. It is illustrated how the interferometer translates the phase shift $\Delta\phi$ introduced by the object into a shift S of the intensity modulation of the interference pattern. (b) Plot of two idealized sinusoidal intensity curves (stepping curves) with and without an object in the beam, observed when images are taken at different stepping positions x_g of the analyser grating. The phase shift $\Delta\phi$ manifests in a phase shift φ between the two stepping curves.

(2.22):

$$\frac{\partial\phi}{\partial x} = \frac{2\pi}{\lambda}\frac{S}{d}. \tag{2.27a}$$

Because the deflection angle and thus the lateral shift S are typically so small, that they can not directly be measured with the X-ray sensitive detector an absorption grating G_2 is typically placed in a Talbot distance $d_T = d$ from the phase grating. This grating is called phase grating and has a period p_2 which matches the periodicity p_{self} of the interference pattern. By laterally shifting (i.e. stepping) one of the gratings over one period, perpendicular to the grating lines (x-direction), and simultaneously acquiring an image at each position x_g effectively samples the intensity pattern and leads to a periodic intensity signal I. To first order, one can approximate the so-called stepping curve by a sinusoidal function

$$I(x_g) = a_0 + a_1\,\sin(\frac{2\pi}{p_2}x_g + \Phi), \tag{2.28}$$

with mean intensity a_0, the amplitude of the interference pattern a_1 and a interferometer phase shift Φ.
The physical meaning of those parameters is given in the next section.
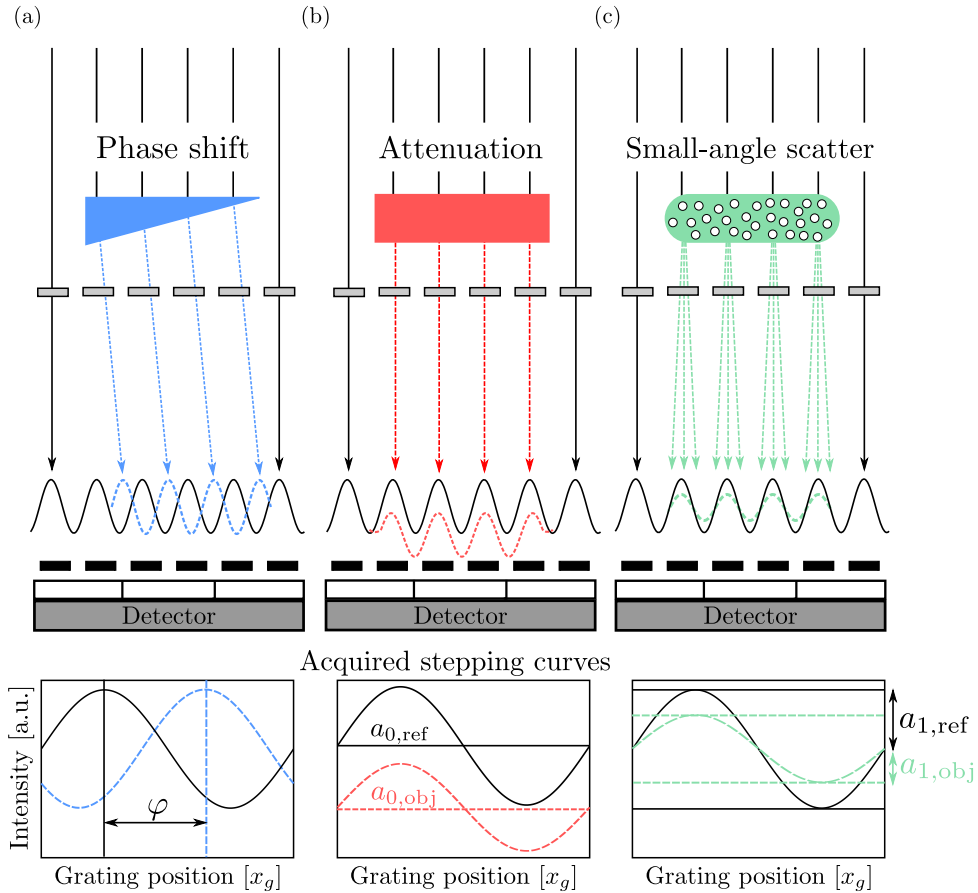
Figure 2.17: Illustration of the interaction processes within the object and how they manifest in the interference pattern. (a) X-ray phase shift, (b) X-ray attenuation, (c) X-ray scatter.

2.6.4 Signal and image extraction

From the description of the stepping curve derived above, one can extract three different image signals as it is explained in the following.

Measuring the stepping curve (2.28) with and without the sample in the beam, leads to periodic intensity signals I_{Obj} and I_{ref}, respectively. Due to the lateral shift S, the two intensity signals have a phase shift φ relative to each other, as illustrated in fig 2.16 (b). After extracting Φ for both stepping curves, with and without the sample, for example by a least-squares fit, one can calculate the relative phase-shift φ between the two curves for each pixel given by:

$$\varphi = \Phi_{obj} - \Phi_{ref}. \tag{2.29}$$

With (2.29), the transverse shift S is given by

$$S = \frac{p_2}{2\pi} \varphi. \tag{2.30}$$

Combining (2.27a) and (2.30) leads to the differential phase shift of the wavefront after traveling through an object [44]:

$$\frac{\partial \phi}{\partial x} = \frac{p_2}{\lambda} \frac{\varphi}{d},$$

(2.31)

as it is shown in Fig. 2.17 (a). Note that since the spatial derivative of the phase shift is extracted, this imaging modality is called differential phase-contrast imaging.

The fit parameter a_0 corresponds to the intensity transmitted through the sample, which therefore leads to the relative transmission T as:

$$T = \frac{a_{0,\text{obj}}}{a_{0,\text{ref}}}.$$

(2.32)

T is shown in Fig. 2.17 (b) and is related to the conventional attenuation signal.

Finally, the decrease of the oscillation amplitude, which is caused by the small angle scattering at microstructures within the sample, shown in Fig. 2.17 (c), with and without the object in the beam, is given by [45]:

$$D = \frac{a_{0,\text{ref}}}{a_{0,\text{obj}}} \frac{a_{1,obj}}{a_{1,ref}},$$

(2.33)

and is typically known as dark-field signal.

Energy dependent Visibility

The 'quality' of the stepping curve depends on many factors such as the grating quality, the interferometer alignment, coherence, finite transmission of G_2, and other influences. Since the quality of the stepping curve directly correlates with the quality of the extracted images, one introduces the performance measure [45]

$$V = \frac{I_{\max} - I_{\min}}{I_{\max} + I_{\min}} = \frac{a_0}{a_1},$$

(2.34)

referred to as visibility. Here, $I_{\max}$ is the maximum and $I_{\min}$ the minimum of the stepping curve, respectively and a_0 and a_1 are the fit parameters introduced in eq. (2.28). Note that in some cases the visibility is normalized to the mean intensity I_{mean}, which results in the alternative definition:

$$V_{alt} = \frac{I_{\max} - I_{\min}}{I_{\text{mean}}} = \frac{2a_0}{a_1}.$$

(2.35)

The visibility is energy dependent and shows a oscillating behaviour with an increasing number of maxima at higher fractional Talbot orders [46]. For polychromatic X-ray sources, the superposition of all contributing energies with relative intensity $w(E)$ leads to an effective mean visibility [47]

$$\bar{V} = \sum_E V(E) w(E).$$

(2.36)

This can potentially be exploited to increase the performance of the X-ray interferometer when using an energy sensitive detector [12] as investigated in the diploma thesis by S. Ehn [48].

Talbot-Lau Interferometer

In order to generate the periodic self-image as described above, the X-ray source with size s, located at a distance l from the phase grating with period p_1, needs to provide a minimal transversal coherence c_t that fullfills [49]:

$$c_t = \lambda\frac{l}{s} > p_1. \tag{2.37}$$

This, in turn, limits the source size s to [19]

$$s < \frac{p_2 l}{2d}, \tag{2.38}$$

which cannot be achieved when using conventional polychromatic X-ray sources. Therefore, an additional absorption grating G_0, referred to as source grating, is placed in front of G_1 and G_2. The source grating effectively divides the extended focal spot into a number of individually coherent (i.e. sufficient to fullfill eq. (2.37)), but mutually incoherent line sources. Each line source generates an interference pattern behind G_1. In order to achieve a constructive overlap of those patterns at the analyzer grating G_2, the period p_0 of the source grating needs to be [49]

$$p_0 = \frac{l}{d}p_2. \tag{2.39}$$

The source grating thereby does not effect the spatial resolution, which is still given by $r = d/l\, s$.

2.7 Tomographic reconstruction | Filtered backprojection

The technique of computed tomography makes it possible to reconstruct the three dimensional image of an object, or more precisely the 3D distribution of its material attenuation properties, from two dimensional projection data taken at many different angles. In the following the mathematical basis for 3D reconstruction of the three image modalities that are obtained with grating-based differential phase-contrast imaging, attenuation, differential phase, and dark field is given for a parallel beam geometry. Further details and a derivation for fan-beam geometry can be found in [50, 51].

Lets describe the physical quantity of an object, for instance the linear attenuation coefficient μ, with an object-function $f(x, y)$. As illustrated in Fig. 2.18 (a), each image taken at an angle θ, referred to as projection $P_\theta(t)$, effectively corresponds to the integration of the values of $f(x, y)$ along the X-rays path through the object at this particular angle. Mathematically, such a projection represents a line integral and can be described by the Radon transform

$$P_\theta(t) = \int \int f(x, y) \, \delta(x \cos(\theta) + y \sin(\theta) - t) \, \mathrm{d}x \, \mathrm{d}y \tag{2.40}$$

with δ being the Dirac delta function and $t = x \cos(\theta) + y \sin(\theta)$. As stated by the Fourier slice theorem, the one-dimensional Fourier transform of (2.40) given by

$$\mathcal{FT}\{P_\theta(t)\} = \tilde{P}_\theta(\omega) = \int P_\theta(t) \exp(-i2\pi\omega t) \mathrm{d}t \tag{2.41}$$

corresponds to a (one-dimensional) slice of the two-dimensional image spectrum

$$\mathcal{FT}\{f(x, y)\} = \tilde{f}(\omega \cos(\theta), \omega \sin(\theta)) = \int \int f(x, y) \, \exp\{-i2\pi[\omega\cos(\theta)x + \omega\sin(\theta)y]\} \, \mathrm{d}x \, \mathrm{d}y, \tag{2.42}$$

as illustrated in in Fig. 2.18 (b). Mathematically this is yields:

$$\tilde{P}_\theta(\omega) = \tilde{f}(\omega \cos(\theta), \omega \sin(\theta)). \tag{2.43}$$

Therefore, the full image spectrum $\tilde{f}(u, v)$, with $(u, v) = (\omega \cos(\theta), \omega \sin(\theta))$, is obtained from Fourier transforms of an infinite amount of projections $P_\theta(t)$ acquired at all angles θ. By calculating the two-dimensional inverse Fourier transform of the image spectrum it is possible to reconstruct the spatial distribution of the object function:

$$f(x, y) = \mathcal{FT}^{-1}\{\tilde{f}(u, v)\}. \tag{2.44}$$

However, in reality, only a finite amount of projections and ray paths can be acquired and thus only a finite set of slices in the frequency domain are available. Because the projections are effectively acquired in a polar coordinate system, while the frequency domain is represented in cartesian coordinates, a lower sampling density appears towards
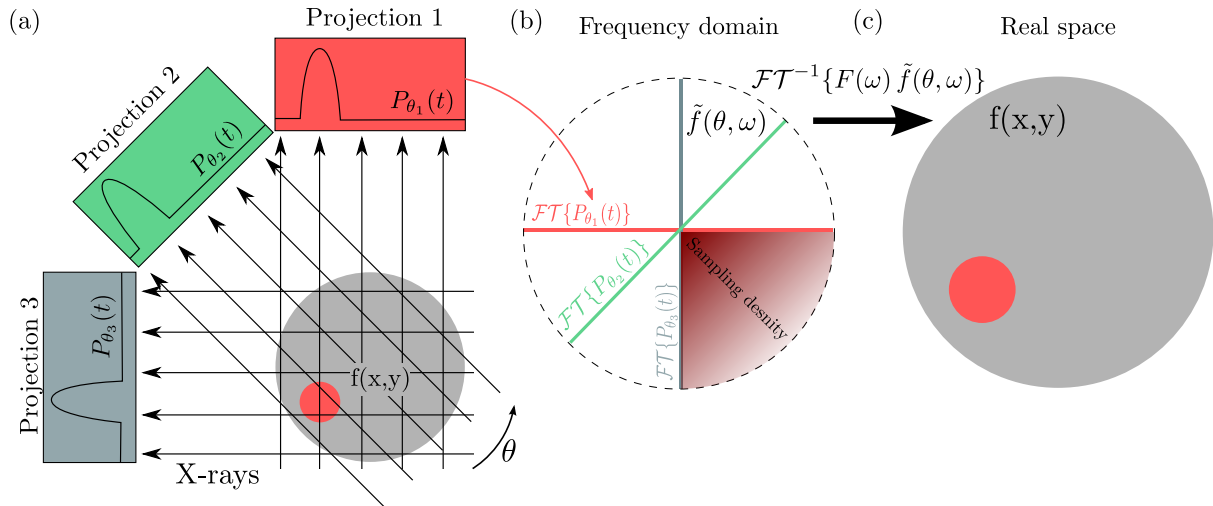
Figure 2.18: Fourier slice theorem and Filtered backprojection. (a) The detector acquires projections $P_\theta(t)$ from the object function $f(x,y)$ at angles θ. This corresponds to the Radon transform $P_\theta(t)$ of the object function $f(x',y')$ in the rotated coordinate system (x',y'). (b) Due to the Fourier slice theorem, the Fourier transform of each projection corresponds to a one-dimensional slice of the two-dimensional image spectrum $\tilde{f}(\theta,\omega)$ in the frequency domain. As illustrated, a lower sampling density is obtained towards the outside of the image spectrum, because the acquisition of the projections effectively takes place in a polar coordinate system. (c) Filtered backprojection: The object-function is reconstructed with an inverse two-dimensional Fourier transform from the image spectrum applying an additional filter function $F(\omega)$, which compensates for the different sampling density.

the outside of the frequency domain, see Fig. 2.18(b). This results in a blurring of the reconstructed image and makes an interpolation necessary, which accounts for the 'stretching' during the coordinate transformation. The interpolation is done with the Jacobian of the transformation, referred to as filter function $F(\omega)$ and finally leads to:

$$f(x,y) = \int \mathcal{FT}^{-1}\{F(\omega)\,\tilde{P}_\theta(\omega)\}\,\mathrm{d}\theta. \qquad (2.45)$$

as illustrated in Fig. 2.18(c).

Attenuation data:
In the conventional attenuation based X-ray imaging, the effectively measured quantity is the linear attenuation coefficient $\mu(x,y)$. The detector measures the transmission image at an angle θ, which is after flat field correction, given as:

$$T_\theta(x') = \exp(-\int_0 \mu(x',y')dy'), \qquad (2.46)$$

where (x',y') are the coordinates of the rotated system. In order to reconstruct $\mu(x,y)$

from those measurements, the Fourier transform of the negative natural logarithm needs to be taken for each projection

$$\tilde{T}_\theta(\omega) = \mathcal{FT}\{-\log(T_\theta(x'))\}. \tag{2.47}$$

Finally, according to (2.45), the spatial distribution $\mu(x, y)$ is reconstructed by:

$$\mu(x, y) = \int_0^\pi \mathcal{FT}^{-1}\{F(\omega)\,\tilde{T}_\theta(\omega)\}\,\mathrm{d}\theta, \tag{2.48}$$

with the filter $F(\omega) = |\omega|$.

Differential phase data:
The refraction angle $\alpha_\theta(x')$ for a coordinate system (x', y'), which is rotated by an angle θ, is given by (2.22):

$$\alpha_\theta(x') = \int \frac{\partial}{\partial x'}\,\delta(x', y')\,\mathrm{d}y'. \tag{2.49}$$

After Fourier transforming (2.49)

$$\tilde{\alpha}_\theta(\omega) = \mathcal{FT}\{\alpha_\theta(x')\} \tag{2.50}$$

one can reconstruct the spatial δ-value distribution

$$\delta(x, y) = \int_0^\pi \mathcal{FT}^{-1}\{H(\omega)\,\tilde{\alpha}_\theta(\omega)\}\,\mathrm{d}\theta. \tag{2.51}$$

In this case, the imaginary Hilbert filter $H(\omega) = i\,\mathrm{sgn}(\omega)/2\pi$ [52], with sgn() being the sign-function, needs to be taken. It accounts for the differential nature of the phase projection and effectively performs an integration in Fourier space.

Dark-field data:
For the dark field, the measured projection $V_\theta(x')$ for a coordinate system (x', y'), which is rotated by an angle θ, is given by:

$$V_\theta(x') = \exp(-\frac{2\pi^2 d^2}{p_2^2} \int \epsilon(x', y')\,\mathrm{d}y'), \tag{2.52}$$

with the linear scattering (or 'diffusion') coefficient $\epsilon(x', y')$ describing the local small-angle scattering strength. The tomographic reconstruction of $\epsilon(x, y)$ is obtained after a Fourier transformation of (2.52):

$$\tilde{V}_\theta(\omega) = \mathcal{FT}\{-\log(V_\theta(x'))\}, \tag{2.53}$$

applying eq. (2.45) with the filter function $F(\omega) = |\omega|$:

$$\epsilon(x, y) = -\frac{p_2^2}{2\pi^2 d^2} \int \mathcal{FT}^{-1}\{F(\omega)\tilde{V}_\theta(\omega)\}\,\mathrm{d}\theta. \tag{2.54}$$

Chapter 3

Large Area Medipix3-Based Detector Array | LAMBDA

3.1 Introduction

In the context of this work, the Large-Area Medipix3-Based Detector Array (LAMBDA) [53] has been used as a spectral X-ray imaging detector. LAMBDA, currently being developed at DESY, is based on the Medipix3 photon-counting hybrid-pixel readout ASIC. It comes with a number of novel features such as charge sharing correction, a high frame rate, continuous photon counting and, a high spatial resolution and the capability for spectral discrimination of X-ray photons. This chapter first describes the Medipix3 readout ASIC (Application-Specific Integrated Circuit) and its features in more detail [54]. Subsequently, an overview of the LAMBDA detector is given, followed by a summary of the preliminary FPGA high-speed readout implementation, which has been realized as part of this work.

3.2 Medipix3 | Hybrid-pixel photon-counting detector

3.2.1 Medipix3 | ASIC

A single Medipix3 photon-counting readout ASIC consists of 256×256 pixels with a size of $55 \times 55 \ \mu m^2$, which are designed and fabricated using the standard $0.13 \ \mu m$ CMOS technology [55]. A single ASIC module has the physical dimensions of $14.1 \times 15.9 \ mm^2$ including the wire bonds located at the longer chip side. A photograph of a single Medipix3 chip connected to a Si sensor is shown in Fig. 3.1 (a). Currently, for the electronic connection of the Medipix3 ASIC to the readout electronics a standard wire-bonding process is used. However, with some minor modifications, the 'through-silicon via' technology (TSV) can be used, which is currently being investigated and developed by different groups within the Medipix3 collaboration. This would allow to tiling together multiple ASICs to form a
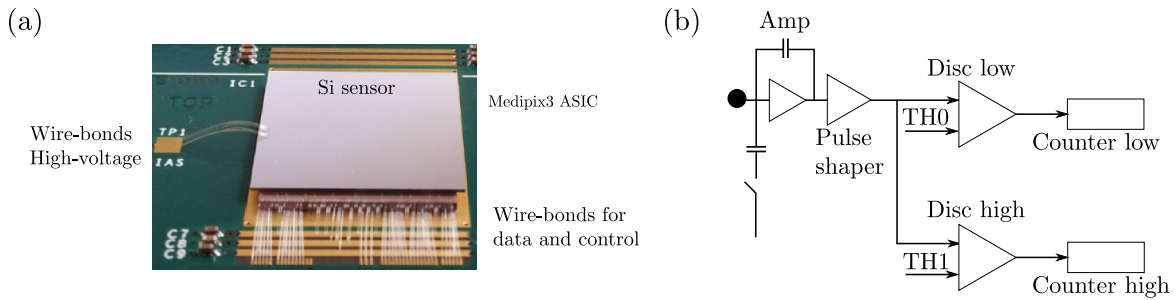
(a)

(b)

Figure 3.1: (a) Single Medipix3 chip equipped with a $300\,\mu$m Si sensor. Image adapted from [54]. (b) Electronic components of a single Medipix3 pixel, configured in 'Single Pixel Mode'. The charge generated in the sensor is amplified, and subsequently shaped by the pulse shaper. The two distinct discriminators 'Disc low' and 'Disc high' compare the current to the adjustable thresholds 'TH0' and 'TH1', respectively. The counter is incremented if the shaper pulse crosses the threshold of the respective discriminator. The two counters and thresholds make it possible to extract only the number of photons between the two threshold values (i.e. the energy bin).

large field of view (FOV) with only very small dead area between the modules compared to the large space required by the wire bonds.

The electronic architecture of a single pixel is shown in Fig. 3.1 (b). It consists of an analog charge-processing part that includes a pre-amplifier and a pulse shaper, as well as a digital part comprised of two discriminators with adjustable thresholds and two 12-bit pseudo-random counters. The common working principles of those components are described in 2.5.4, and are summarized in the following. The pre-amplifier amplifies the generated charge pulse, which is stored in the input capacitance. The pulse shaper subsequently converts the narrow charge pulse into a broad current pulse with a peak amplitude proportional to the energy of the X-ray photon. The two distinct discriminators compare the current pulse 'height' to threshold currents 'TH0 and 'TH1', respectively, which can be adjusted with a 9-bit global digital-to-analog converter. The discriminators are realized with standard CMOS comparators, which send a logical signal each time the shaper pulse crosses the reference value. Finally, the digital pulse increments the counter. The counters are realized with ordinary flip-flop shift registers, which are electronically connected to form a quasi-random counter. This kind of counter does not simply increment the counter value each time a photon is detected, but generates a 'random' counter value following a predictable pattern. This simplifies the implementation of the counter, but makes a decoding of the counter value necessary. Since each pixel contains two discriminators and counters, the Medipix3 chip allows for an energy discriminated measurement. In order to transfer the counter values to the data processing unit, the counters from each column are daisy-chained to form a large 256-bit wide shift register. Then, the counter bits are shifted to a dedicated readout shift register in a parallel manner. The register transmits the bits to the external readout board via 1, 2, 4, or 8 output ports.

A unique feature of the Medipix3 ASIC is the possibility for on-chip charge-sharing correction. This is realized as a two-step process: First, the total charge generated by an
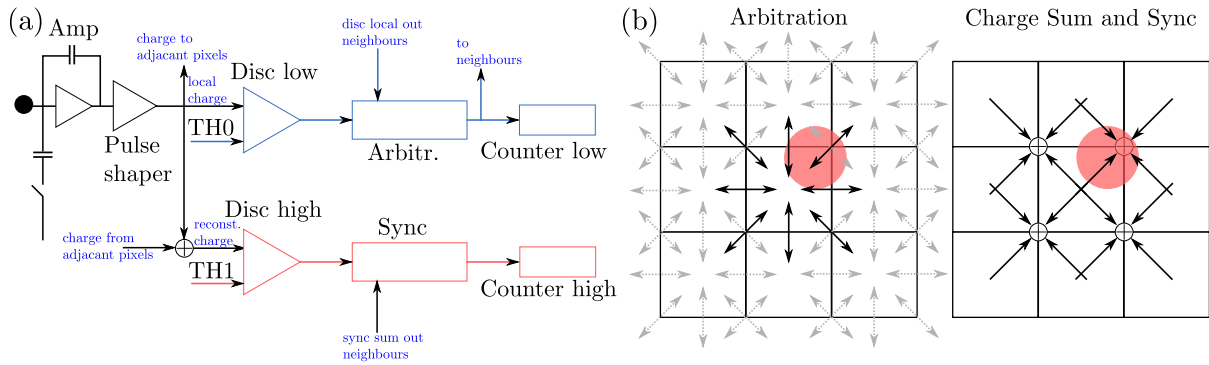
Figure 3.2: (a) Electronic components of a single Medipix3 pixel, configured in 'Charge Summing Mode'. (b) Sketch of the charge summing procedure. In the arbitration process, the lower counter from a pixel in the cluster is only incremented, if the pixel received the highest amount of charge. The summing node, on the other hand, combines all currents from the adjacent pixels, and thereby reconstructs the complete charge that was generated by the absorbed X-ray, but had been distributed between the adjacent pixels due to charge sharing. The higher counter is only incremented, if the corresponding pixel received the largest of the deposited charge (determined by the arbitration process), and if the total amount of charge is larger than the adjusted threshold.

absorbed X-ray photon in the semiconductor sensor is reconstructed in 2×2 pixel clusters as the sum of the signals in the individual pixels. Second, the local charge in each individual pixel is compared to a reference discriminator threshold. An arbitration network determines for all neighbouring pixels which one of them received the largest charge package. Finally, the counter in the pixel with the largest charge package is incremented, if the reconstructed total charge exceeds the programmed threshold.

Further, the Medipix3 ASIC is designed to be equipped with different sensor materials like Si, CdTe, GaAs, or Ge making it possible to manufacture a detector optimized for a specific energy range.

3.2.2 Medipix3 | Modes of operation

The Medipix3 ASIC features several modes of operation, which make it possible to employ this detector for a wide range of applications. The most important operation modes are described in the following.

Single-pixel mode

In this operation mode, the outputs from the two shaper in each pixel are only connected to the corresponding discriminators and counters within the pixel as it is shown in Fig. 3.1 (b). Thus, each pixel is independent with respect to its neighbouring pixels.

Charge-summing mode

The block schematic of this mode is shown in Fig. 3.2 (a). It activates the charge-sharing correction mechanism, schematically shown in Fig. 3.2 (b). Hereby, each four adjacent pixels are electronically clustered, enabling them to correct for the charge sharing that has occurred among them. The charge sharing correction works as follows:
First the current from each pixel is compared to the local threshold of the lower discriminator and counter (TH0). At the same time, the current is sent to the adjacent arbitration logic and the summing node. The arbitration logic, on the other hand, compares the local signals from the corresponding neighbouring pixels to each other. If the local pixel is determined as the one with the largest energy deposit the lower counter of this local pixel is incremented. This effectively increases the spatial resolution, since blurring effects due to charge sharing are avoided.
The summing node, on the other hand, combines all currents from the adjacent pixels and thus reconstructs the total charge generated by the absorbed X-ray, which has been distributed (i.e. shared) between the adjacent pixels due to charge sharing. Then, the reconstructed signal is compared to the threshold from the discriminator corresponding to higher counter (TH1) in each of the four pixels from the group. Finally, the internal logic increases the higher counter of that pixel only, if first, the hit was allocated to it and, if second, the reconstructed charge in one of the adjacent summing circuits exceeds the programmed threshold (TH1). In short words, the higher counters are only incremented, if the corresponding pixel received the largest portion of the deposited charge, as determined by the arbitration process, and if the total amount of charge is higher than the adjusted threshold. This increases both, the spatial resolution, as it was the case for the lower counter, but also the energy resolution.

Fine-pitch mode

In this mode, the pixel pitch of the detector matches the $55\,\mu m$ pitch of the readout ASIC. This makes a high spatial resolution possible and is advantageous for high flux applications. Because of the two counters and discriminators, an energy window can be defined by the user, which effectively corresponds to two energy bins.

Spectroscopic mode

In spectroscopic mode, only one out of four pixels on the readout ASIC is connected to the sensor via bump bonds. To process the signals, only the pre-amplifier and shaper of this specific pixel is used. The shaper outputs of the three adjacent and not bump-bonded pixels are bypassed, and the signals from the bump-bonded pixel are directly sent to the discriminators of all four pixels. Therefore, the four pixels effectively form a larger pixel with $110\,\mu m \times 110\,\mu m$ and thus provide more energy thresholds. If the spectroscopic mode is operated in single-pixel mode, eight individual thresholds are available. Operated in charge summing mode, four thresholds are available, which are fully charge-sharing corrected. In addition, four thresholds with the locally deposited charge information are available. Note that operation of the ASIC in a combination of spectroscopic and
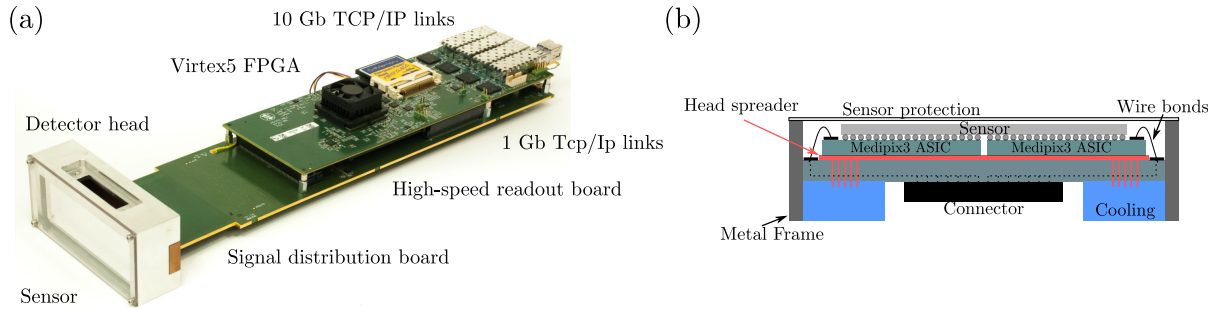
Figure 3.3: (a) Picture of a LAMBDA module without a housing. (b) Cross section of the LAMBDA detector head.

charge summing mode requires a sensor structure and bonding different from fine-pitch mode. However, spectroscopic mode without charge-sharing correction works also with the standard 55 μm sensors, where all pixels are bump-bonded, but effectively looses 75 % of the active sensor area since the inputs of three out of four pixels are bypassed.

Therefore, the decision of operating the detector in spectroscopic mode should be made prior to sensor production.

Continuous read/write mode

The continuous read/write mode makes a dead-time free measurement possible. Note that in this context, dead time refers to the time needed for the readout of the counter data to the FPGA (Field Programmable Gate Array), during which the shutter has to be closed and no counting is possible. In this mode, one counter is incremented while the other one is being read out. Therefore, no break time is needed, during which the counters are read out.

3.3 LAMBDA | Concept and control

The detector group at DESY is developing the large-area Medipix3-based detector array (LAMBDA), which consists of two by six Medipix3 chips with 1536×512 pixels mounted onto a ceramic carrier board and bump-bonded to a semiconductor sensor. A picture of the whole detector is shown in Fig. 3.3 (a).

One module consists of a detector head with a semiconductor sensor and a readout board that fits behind the carrier board to allow module tiling. In the following, the different components are described in more detail as published in [56].

LAMBDA | Sensor and detector head

A cross section of a LAMBDA detector head is shown in Fig. 3.3 (b). The Medipix3 chips are mounted on a ceramic board in an two by six array. A semiconductor sensor with a field of view of about $85.6 \, \text{mm} \times 28.4 \, \text{mm}$ is bump-bonded onto the readout ASIC.

As described earlier, the Medipix3 ASIC is designed to be equipped with different sensor materials so that the LAMBDA module will be available with ordinary 300 μm Si sensors as well as high-Z sensors like CdTe, GaAs, or Ge. Since especially the high-Z sensors require sufficient cooling, the ceramic is mounted on a head spreader that is thermally connected to a metal cooling block cooled by Peltier elements. For high-speed readout, each chip transmits the image data via eight LVDS output signal pairs. The signal lines for control and data read-out, and the power planes are connected to the signal lines on the ceramic board via ordinary wire bonds. For the tiled modules, this means that there will be a 3.6 mm gap between the individual modules, necessary for the wire-bond connections. In a future version, silicon-through-vias will reduce the insensitive gap to about 1 mm.

LAMBDA | Signal distribution and high-speed readout board

The detector head is mounted to a signal distribution and high-speed readout 'Mezzanine' board via a 500-pin high-density right-angle connector. The readout board is equipped with a Virtex-5 FPGA which allows to read the data from all twelve Medipix3 chips in parallel. A CPU with Power-PC (PPC) architecture is used for the configuration of the detector. For the operation in slow mode, meaning up to a frame rate of about 60 fps, the images are transferred to the PC via a 1 Gb TCP/IP link. For high-speed readout, three 10 Gb UDP/IP links allow a continuous operation at 2000 fps, which, however, requires also a large subsequent computing infrastructure. Thus, during burst-mode operation, images are acquired at a high frame rate and temporarily buffered in the one or 2 GB on-board RAM. Subsequently, the images are transmitted on lower rate via a single 10 Gb link or by using only the standard 1 Gb link.

The high-speed readout 'Mezzanine' board is mounted on a signal-distribution board which transfers signals between the detector head and the FPGA. Further, it provides voltage regulators to power the detector head as well as the converters that are used to monitor the Medipix3 chips and supplies certain control voltages.

Since the Ge sensor needs to be cooled by liquid nitrogen and must be operated in a vacuum chamber, there is an open space close to the detector head where a vacuum barrier can be glued. This allows the detector head to operate in vacuum while most of the readout electronics remain in air.

3.4 LAMBDA | High-speed readout — VHDL design and implementation

As explained in the previous section, the configuration of the LAMBDA detector is achieved and controlled with the PPC on the FPGA. Details about the PPC programming can be found in Somljanin et al. [57]. However, for reaching the target frame rate of up to 2000 fps, it is necessary to operate the detector with a clock frequency of 200 MHz and to transfer the image data via 96 parallel data lines. At full speed, the LAMBDA detector produces about 2.4 GB/s, which need to be transferred reliably to the PC controlled by

the FPGA. The main part of the FPGA programming, in particular the implementation of the 10 Gb UDP/IP high speed readout, and the PPC programming have been done by Electronics Development Group and the detector group at DESY [58]. In the context of this work, the preliminary implementation of the parallel image readout and of the bit reordering on the FPGA has been realized, and the concept and implementation is summarized in the following sections.

3.4.1 High-speed readout architecture

Figure 3.4 shows a block diagram with the most important modules.
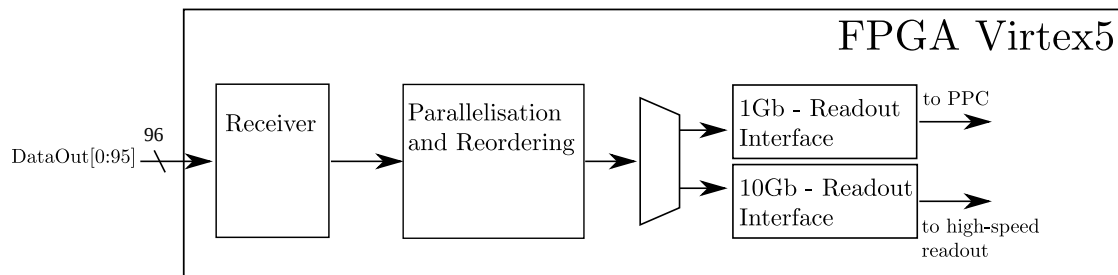

Figure 3.4: General readout architecture. The **Receiver** module samples the incoming image data and synchronizes the signals with the global clock source on the FPGA. The **Parallelisation and Reordering** module reverses the serialization that occurs on the Medipix3 chip during readout and reorders the counter bits. Finally the data is stored in the selected readout interface for 10 Gb UDP/IP high speed or 1 Gb TCP/IP readout.

The **Receiver** module samples the transferred image data, synchronizes it to the global clock on the FPGA, and compensates for phase and run time differences between the signals. The main purpose of the **Parallelisation and Reordering** module is to reorder the counter values from each pixel that get scrambled during the readout process. Subsequently, the image data is transferred either to the ordinary 1 Gb TCP/IP interface or to the 10 Gb UDP/IP high-speed readout interface. In this chapter, details on the specific design and the final implementation of the mentioned components will be given.

3.4.2 Receiver architecture

As the Medipix3 chip does not have a clock source on its own, it needs to be provided by the readout system (i.e. the FPGA) via the clock input port 'MDX_ClockIn'. Within the chip, this clock signal is looped back and serves then as the readout clock signal 'MDX_ClockOut'. The image data is then transferred via eight parallel LVDS connections, which are synchronized with the falling edge of the readout clock 'MDX_ClockOut' [59]. This concept ensures that the readout clock of the Medipix3 chips, and with it the image data, is in phase with the global system clock 'system_clk' on the FPGA. However, as the LAMBDA module consists of twelve individual Medipix3 chips and there exist structural tolerances within one chip, variances in the voltage

levels and/or slightly different wire lengths on the signal-distribution board cause phase differences (i.e. clock skews) between the twelve readout clock signals and slightly different arrival times between the 96 image data signals. Those delays, de-synchronizing the signals, are the main problem at high clock frequencies and prevent the FPGA from a correct data sampling. The main purpose of the **Receiver** module is to compensate for those differences in order to ensure a correct data sampling and to synchronize the incoming signals with the global clock on the FPGA. Since the differences in the arrival time increase with higher clock frequencies, different strategies were tested to provide a correct data sampling.

Up to approximately 100 MHz:
For frequencies below approximately 100 MHz the clock skews and the difference in the arrival times of the data signals are small enough to sample the data directly with a two-flip–flops synchronizer [60]. That is clocked with the same clock source as it is provided to the Medipix3 chips. In order to ensure sampling at a stable bit state, even if small skews are present, the data was taken synchronously with the rising edge of the system clock. The strategy of using a two-flip–flops synchronizer reduces the chance of metastable and/or unpredictable states within the FPGA arising from run-time differences due to a different signal routing. This easy to implement and resource-conservative approach can be used if the timing differences between the sampling clocks and the data signals are much smaller than 180 degree.

Frequencies above 140 MHz:
Provided that the different readout clocks have skews of multiple full clock cycles, the presented offset correction, which adjusts the lengths of dynamic shift registers, is sufficient. In the same way, the presented signal sampling strategies are successful if the time of arrival differences between the signals from one chip are such that they can be sampled with the readout clock of the same chip. Both requirements are not fullfilled at frequencies above approximately 140 MHz. Instead, the timing difference between the readout clock and the data signals vary for each signal and are just a fraction of a clock cycle. Further, fast variations of the signal edge location with respect to its reference position, called jitter, are present [61, 62]. This shrinks the data-valid window and requires the position of the sampling edge close to the center between two bit transitions. Both effects make it necessary to delay each incoming signal individually in order to ensure a correct data sampling. For this reason, the I/O blocks in the Virtex5 FPGA, which are organized in banks with 40 I/O blocks each, contain programmable 64-tap input delay elements called **IDELAY** with a calibrated tap resolution. This module makes it possible to delay the incoming signals on the required individual basis by adding delays to the data paths [63]. An IDELAY calibration procedure for a DDR memory device is presented in Burton et al. [64], which can be adopted and modified to the case of the LAMBDA detector and the general design idea is given in the following. However, the final implementation was not completed at the time of submission.
The block diagram of the **Receiver** module is shown in Fig. 3.5.

For each FPGA bank used for the 96 LVDS input connections one **IDELAYCTRL**
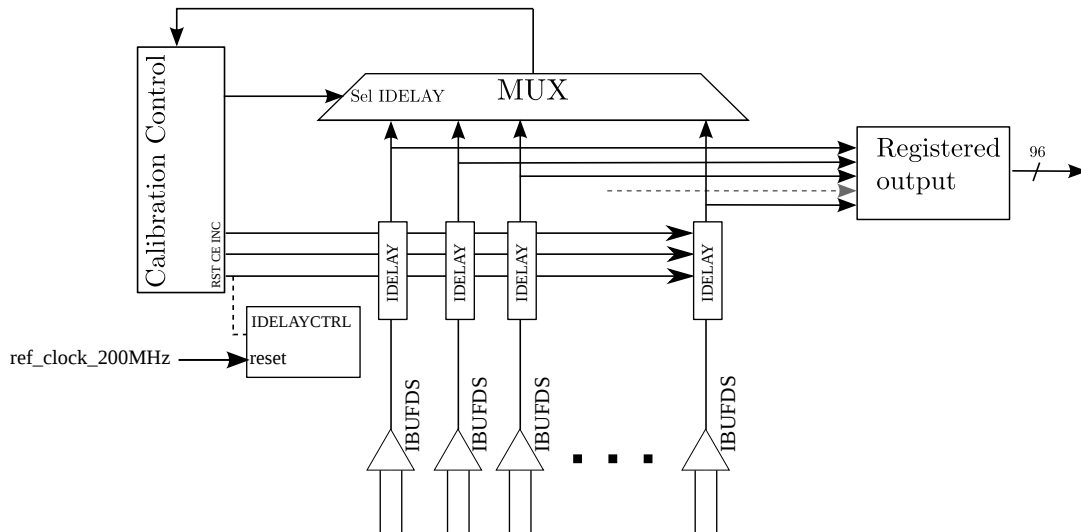
Figure 3.5: Block diagram of the calibration module for frequencies above approximately 140 MHz. The **IDELAY** elements make it possible to calibrate each incoming signal by an individual amount, controlled by the **IDELAYCTRL** module. The **Calibration Control** manages the procedure to determine the delay necessary for each signal. For the calibration of the delay length, a training pattern is used. For saving FPGA resources, the **Calibration Control** can be instantiated once and the successive calibration of the **IDELAY** components is controlled with the multiplexer component **MUX**.

module, clocked with a 200 MHz reference clock, is needed to calibrate the delay elements. In the case where all connections would be in the same bank, one **IDELAYCTRL** module is sufficient and the incoming clock signal could be distributed by a regional clock buffer 'BUFR'. However, in the case of the LAMBDA module, the LVDS input channels are spread over several banks, which makes the usage of multiple **IDELAYCTRL** modules and global clock buffers 'BUFG' necessary. The core module of the **Receiver** is the **IDELAY Calibration Machine**, which performs a four step procedure to calibrate the **IDELAY** elements:

1. Step: Find the position of the first bit transition.
   The position of a bit transition needs to be found by increasing the amount of delay within the **IDELAY** module. The number j of tap increments is counted, starting from tab 0.

2. Step: Find the end the first bit transition.
   The end of the first bit transition needs to be found by further increasing and counting the tab delay j.

3. Step: Find the next bit transition.
   The next bit transition needs to be found by a further increase of the tab-delay. The number i of tab increments is counted.
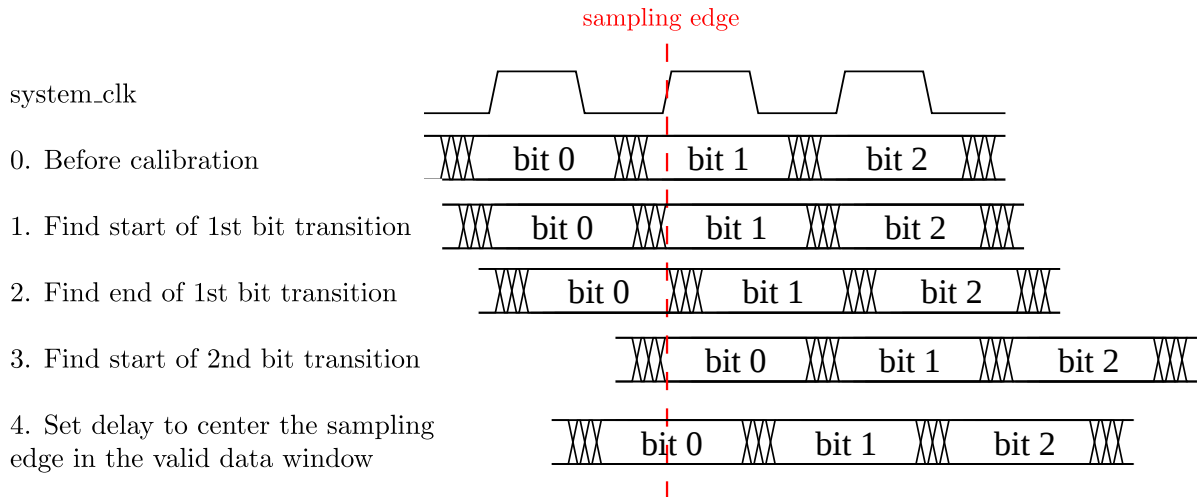
Figure 3.6: Schematic of the four step procedure performed to determine the necessary delay of an **IDELAY** element.

4. Step: Configure the IDELAY such that the clock samples the bit in the center of the valid data window.
   The final tab delay value $d = j + i/2$ of the IDELAY is calculated and set.

Finding the end of the first bit transition respects the jitter in the signal and lowers the risk of finding an eventually wrong second transition. Figure 3.6 illustrates the calibration process. Of course, the 2nd step could be omitted in the case where no jitter is present. For the calibration process, a known training pattern needs to be transmitted from the detector. The training pattern is chosen to be 10101010 (0xAA), which should allow an easy and secure determination of the first and second bit transitions. However, the particular training pattern is rather arbitrary and any other pattern could be used as well. The state diagram of the **IDELAY_Calibration** state machine, which executes the calibration algorithm of the input delay elements, is shown in Fig. 3.7. Each IDELAY output is connected to the **MUX** which is also controlled by the **IDELAY Calibration Machine**. By successively selecting the IDELAY elements for calibration, only one instantiation of the **IDELAY Calibration Machine** is necessary, which saves FPGA resources.
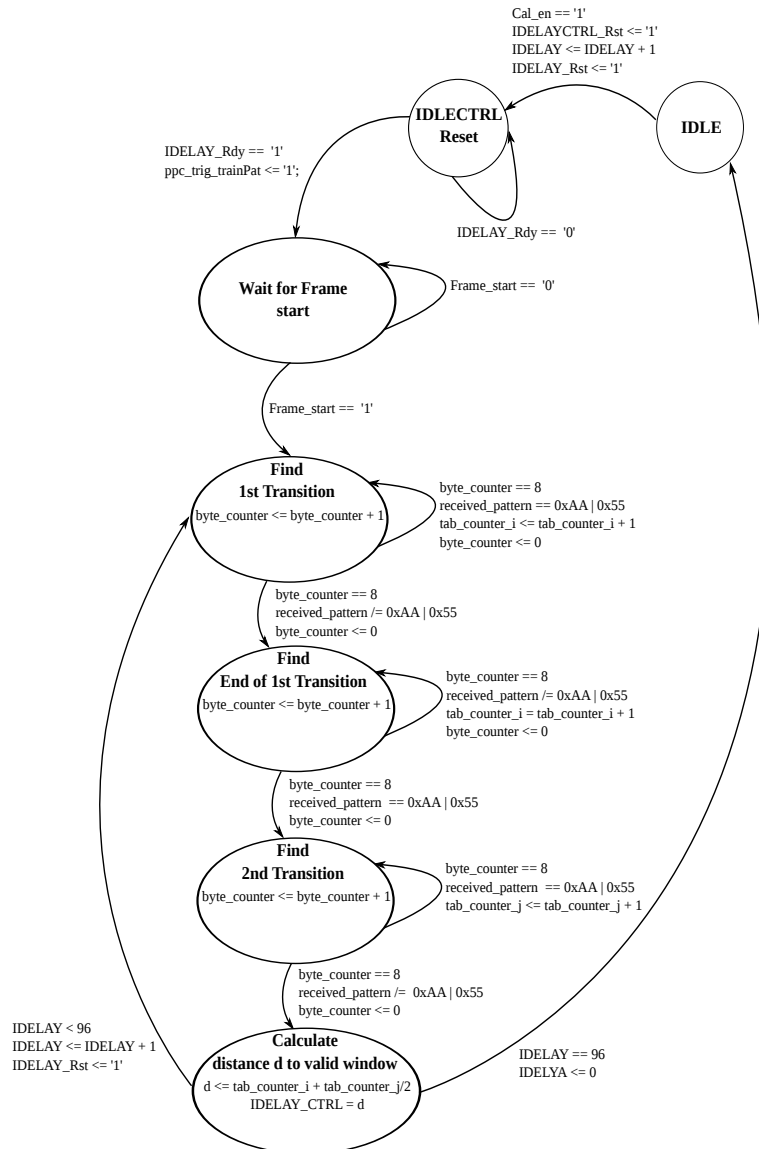
Figure 3.7: State flow diagram from the state machine of the **Calibration Control**, which performs the calibration procedure of the **IDELAY** elements.

3.4.3 Data processing

The transferred bits of all counters in the Medipix3 pixel matrix are unsorted due to the readout architecture, which is illustrated in Fig. 3.8. Each pixel in the pixel matrix contains two 12 bit counters c_l and C_h. After the image is recorded, for instance with counter C_l, all counters from one pixel column C_x with $x = 0, 1, 2, 3, ...255$ are daisy-chained to build a clocked 256 bit wide parallel shift register. Subsequently, the readout process is performed as follows:

1. The first bit in each column is shifted into a clocked serial shift register (SSR).
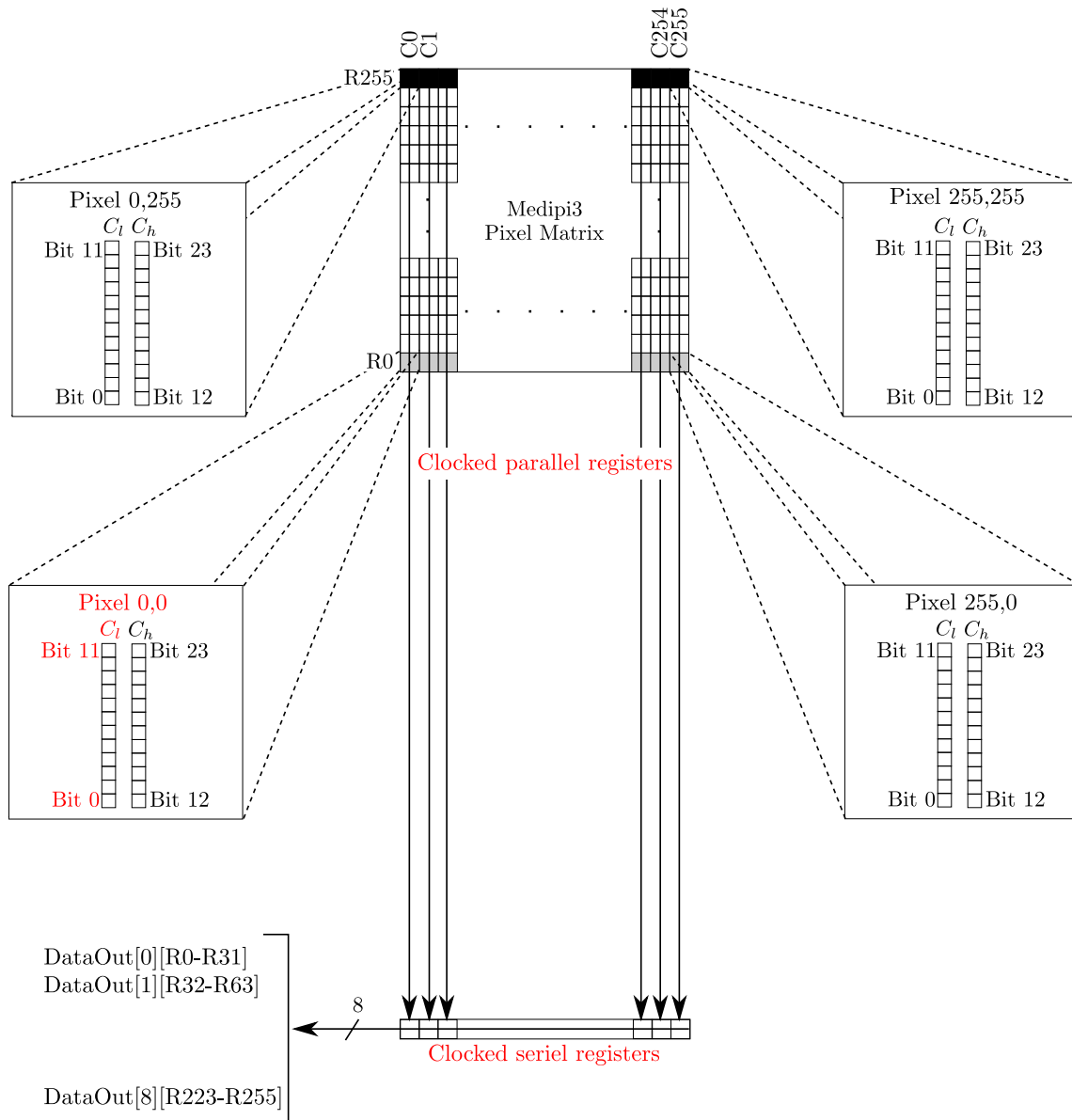
Figure 3.8: Simplified sketch of the readout process of the Medipix3 pixel matrix. Each pixel contains two counters C_l and C_h. For the readout, all counters from one pixel column are daisy chained and the pixel matrix practically corresponds to a 256 bit wide and 3072 bit deep parallel shift register. The counter bits are successively shifted (illustrated by the vertical arrows) into the clocked serial shift register. The serial shift register transmits the data via eight parallel output ports DataOut[0:7] to the FPGA. This readout process leads to a disorder of the counter bits.

2. The bits in the SSR are transferred via eight parallel output ports DataOut[0:7].

3. If the SSR is empty after 32 clock cycles, the next bit in the pixel matrix is shifted into the SSR.

a)

b)

Figure 3.9: Illustration from the position of the counter bits as they are transmitted to the FPGA via 8 parallel output ports. Shown are the ports DataOut[0], DataOut[1] and DataOut[7]. a) Bit positions after 384 clock cycles, which corresponds to a complete readout of the all counters from one pixel row. b) Bit positions after another 384 clock cycles corresponding to the data from the next full pixel row.
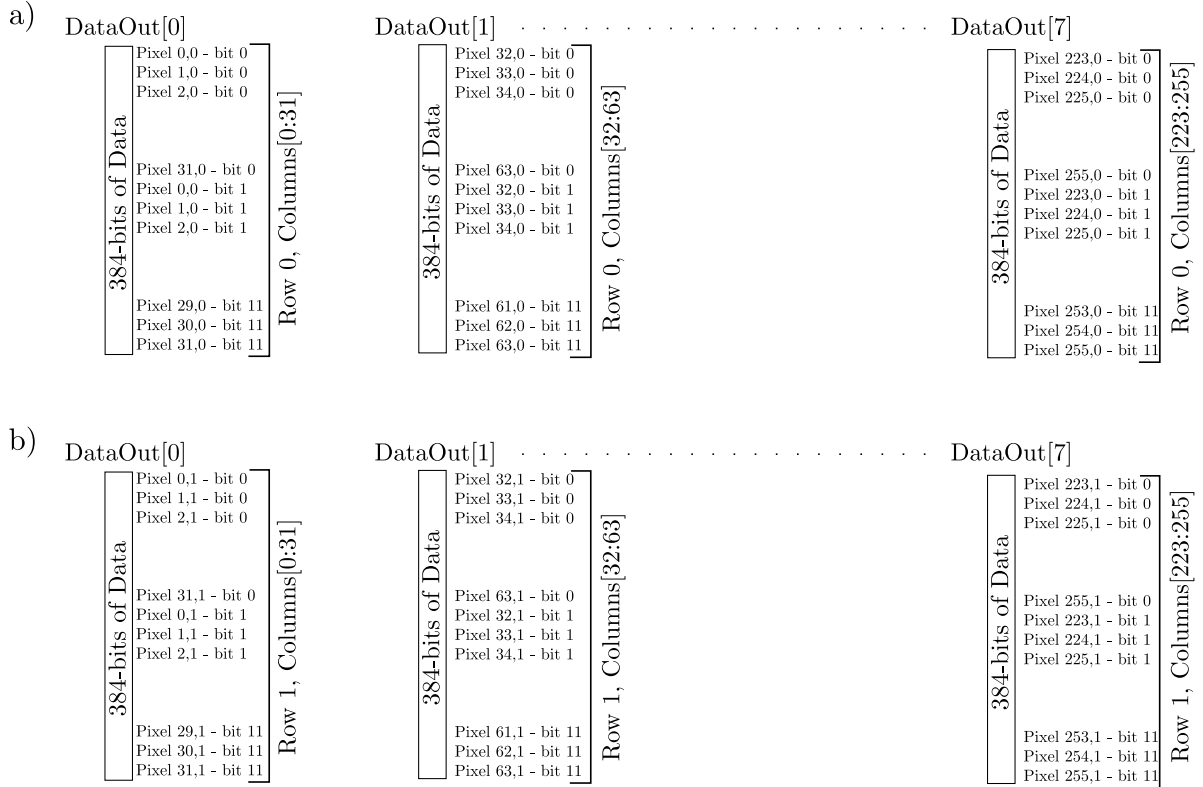
4. The steps 2 and 3 are iterated until the whole pixel matrix has been read out.

Since eight output ports are used, all 12 bits from the counters in row R0 are completely transmitted to the FPGA after $32 \times 12 = 384$ clock cycles. By that time, the FPGA has received the data pattern that is shown in Fig. 3.9 (a) for the ports DataOut[0], DataOut[1] and DataOut[7]. Figure 3.9 (b) shows the data pattern after another 384 clock cycles, when the data bits from the counters in R1 have been fully transmitted. To transfer the whole pixel matrix, $12 \times 256 \times 256/8 = 98304$ clock cycles are needed. Of course, the bit reordering of the counter values could be done later on the PC. However, with respect to the high frame rate, it is appropriate to reassemble the image data directly on the FPGA to reduce the work load on the computer. For the design of the reordering module, it had to be accounted for that the size of a full LAMBDA image with approximately 1.2 MB exceeds the memory resources (Block RAM, Distributed RAM, Flip-Flops, ...) on the Virtex5 FPGA, and that the two external DDR memories are reserved for the PPC operation and the high-speed 10 Gb readout. Therefore, it is not possible to store the whole image data on the FPGA and the reordering has to be done on the fly, counter row by counter row, in a fully parallel manner. To reorder the bits of the

Figure 3.10: Block diagram of the process that reorders the transmitted counter bits, controlled by the **Control** logic. The **Frame start/stop** logic determines the start and the end of each image frame. The **Header generator** builds a global 32 byte header. The **Ser-Par 8×32** module performs a 32 bit serial to parallel conversion for each of the input ports. The actual reordering is done by the **Reordering** module. After reordering, the data is stored in the interface Fifo selected by the 'Readout_Sel' signal.

counters of one pixel row, it is necessary to buffer at least the 12 bit from each counter on the FPGA, which sums up to $256 \times 12 = 3072$ bit. Since the twelve chips on the LAMBDA module shall be read out in parallel an amount of $3072 \times 12 = 36864$ bit needs to be buffered on the FPGA in total. The used common flip flops to store this amount of data would exceed the resources of the FPGA. Moreover, as mentioned above, the amount of utilized BRAMs had to be kept as small as possible, because the implementation of the 10 Gb readout requires those resources. Therefore, the reordering was designed to use a minimum amount of distributed RAM for the data buffering, and SRL16E shift registers, synthesized from look-up tables, were used for the reordering process itself. The block diagram shown in Fig. 3.10 illustrates the main components of the reordering module, which are explained below. The figure neglects the control signals for the purpose of a better readability. Instead of one large reordering module for the reordering of all twelve chips, the parts within the green shaded area are instantiated once for each Medipix3 chip. This makes the design more modular and allows a fast and easy implementation of additional features such as a 'chip-of-interest readout'. In the following, the components needed to reorder the counter values of one Medipix3 chip are explained:

The **Frame start/stop** logic determines the start and the end of each image frame and enables the **Control** logic, which manages the processes of the reordering module, as well as the **Header generator**. The start of each frame is determined by a 0xA0 pre-sync sequence, and the end is determined by detecting the 1-to-0 transition of the EnableOut signal provided by the Medipix3 chip. If the start of an image frame is detected, the **Header generator** builds a global 32 byte header, in which the first byte is reserved for preserving the 0xA0 pre-sync sequence and the remaining bytes might be used to store dedicated image information such as the image number. More complex image information, such as the exposure time and the counter threshold value, could be provided by the PPC processor in form of an additional information signal. After the header is constructed, it is stored in the interface Fifo for the 1 Gb or 10 Gb readout, selected with the 'Readout_sel' signal. As explained above, the 256 bits from one pixel row are transmitted serially via eight parallel output ports 'DataOut[0:7]', and, thus, are split into eight chunks, each containing 32 bits. Thereby, the first step of the reordering process reverses the serialisation and the splitting with the **Ser-Par 8×32** module, which performs a 32 bit serial-to-parallel conversion for each of the input ports. After the conversion, the 256 bit data is buffered in parallel with a Fifo, synthesized from distributed RAM, with a 256 bit write/read width and a minimal write depth of 16 bit. Note, that, a buffer Fifo is necessary at this point, because the SRL16E shift registers that are used for the actual reordering process do not allow a parallel reading. Therefore, the reading of the complete SRL16E data requires more than the 32 clock cycles that are necessary for the parallelisation of the incoming data. This leads to a short-term bottle neck and makes a temporary buffering of the incoming data mandatory. The calculation of the minimal Fifo depth that is necessary to buffer the incoming data is given below. After buffering the data, it is parallely shifted into 256 SRL16E shift registers, which are configured to have a shift length of 12 bit (or 6 bit) depending on the selected counter depth on the Medipix3 chip. In the case of 12 bit counters, after $32 \times 12 = 384$ clock cycles each of the SRL16E shift registers contains the 12 bit counter value of one corresponding pixel on the Medipix3 chip. Since the SRL16E shift registers do not allow a parallel, but only a serial reading, the content of 64 SRL16E shift registers are written simultaneously into 64 connected 12 bit serial to parallel conversion modules. Those modules are connected to generate a 768 bit long data structure corresponding to 64 reordered counter values from 64 consecutive pixels on the Medipix3 chip. Finally, the reordered data is buffered in the Fifo that corresponds to the selected readout interface. Since both interface Fifos have a 256 bit wide read width, three clock cycles are necessary to store the 768 bits (64 pixels) of one chip and $3 \times 12 = 36$ clock cycles are needed for all twelve chips. After the data from all twelve chips is stored in the Fifo, the next 64 pixels are reordered. This method makes a fast, parallel reordering possible, but has the drawback that the 256 pixel rows from each chip are not transmitted at once, but are split into chunks of 64 pixel (768 bit). As mentioned above, the buffer Fifo is necessary because the reading of the complete SRL16E data requires more than the 32 clock cycles that are mandatory for the parallelisation of the incoming data. Thus, to be able to read out the SRL16E shift registers completely before filling them with new data, a buffer Fifo needs to be instantiated. The depth of the Fifo, which has the same clock frequency on the writing and reading side,

can be determined by calculating the writing rate r_w as well as the reading rate r_r of the SRL16E without the Fifo. In this case, the writing rate is given by the **32 bit SER-PAR** module. It needs 32 clock cycles for the parallelisation of the serial data and thus fills the Fifo with a rate of $r_w = 1/32\,\mathrm{clk}^{-1}$. For the reading rate, the subsequent processes need to be taken into account. The first process that needs to be respected is the simultaneous reading of 64 SRL16E shift registers, which takes $t_{sr} = 12$ clock cycles. For writing the data into one of the interface Fifos another $t_{sf} = 3$ clock cycles are necessary. In principle, after the data is written into the Fifo, the content of the next 64 SRL16E shift registers could be read. Nevertheless, a more conservative design, with the advantage of a simplified control state-machine, waits for the data of all chips to be stored in the Fifo. This requires an additional time of $t_{oc} = 11 \times 3 = 33$ clock cycles. Thus, for the reading of 64 SRL16E shift registers $t = t_{sr} + t_{sf} + t_{oc} = 48$ clock cycles are necessary, and to read all 256 SRL16E shift registers an overall time of $t_o = t \times 3 = 144$ clock cycles is required. Therefore, the SRL16E shift registers are read with a rate of $r_r = 1/t_o$. To buffer the incoming data, a minimal depth of $d = \lceil r_w/r_r \rceil = 5$ is needed. The generated standard Fifos, which are provided by the Xlinix IP, do allow a minimal depth of only 16 bit, and, thus, a resource sharing between two chips can be implemented to reduce FPGA resources.

3.5 Summary

In this chapter, the LAMBDA detector, which has been utilized as imaging detector throughout this work, was introduced. First, the Medipix3 readout ASIC was explained, its features like the charge sharing correction was described, and the various modes of operation were presented. Second, the technical concept of the LAMBDA detector for signal distribution and the implemented high-speed readout architecture were described. The high-speed readout was designed as part of this work in VHDL and was preliminarily implemented on the FPGA for high-speed measurements. The working principle of the various VHDL modules for the data receiving, the data reordering, the data processing, and the data transmission to the computer, as well as the implementation on the FPGA were presented.

The design was proven to work reliable for readout frame rates up to about $750\,\mathrm{fps}$. The bit reordering could be implemented successfully, and was tested for LAMBDA modules that consist of six Medipix3 chips. However, the bit reordering could not be implemented for a full module that consists of twelve chips because of the limited digital resources on the FPGA.

Chapter 4

Spectral Phase Unwrapping

4.1 Motivation

Grating-based differential phase-contrast imaging translates the phase shift of the X-ray wave that is introduced by an object in the beam into a corresponding phase shift of the interference pattern. While the object phase shift can take any value, the measurement of the interference-pattern phase shift is bound the interval $]-\pi, \pi]$. In case the interference-pattern phase shift exceeds this range, an ambiguous measurement is obtained, known as a 'phase-wrapped' signal. Since the phenomenon of phase wrapping leads to strong artefacts in the extracted image, a reconstruction of the true phase shift, referred to as phase-unwrapping, is necessary. This task is challenging and subject to more than 500 publications, each presenting an original unwrapping technique. However, conventional phase-unwrapping algorithms, which are typically dedicated to non-differential phase data as for example obtained in Magnetic Resonance Imaging (MRI) and Synthetic Aperture Radar (SAR), can not directly be applied to the differential phase data given in DPC imaging. Those algorithms require a proper sampling of the phase signal. According to the Nyquist theorem, more than two samples per period of the highest frequency component need to be obtained [65]. This is equivalent to the requirement that the local phase changes are smaller than π. Since DPC imaging delivers positive and negative gradients of the phase, this requirement cannot be satisfied easily. Instead, phase wrapping can even occur within one pixel, which is sometimes called 'phase clipping' [66]. The insufficient phase sampling causes the commonly used unwrapping methods, which rely for example on region growing algorithms, to fail. Therefore, new unwrapping methods that are dedicated to the differential phase measurement are preferable. Some investigations on new algorithms that considers the differential nature of the phase data have been made in the last years. Based on the observation that phase wrapping occurs at locations where the absorption contrast is high and that the behaviour of the gradient of both contrasts is similar, Haas et al. [67] and Jerjen et al. [66] proposed in 2011 to use the attenuation contrast to correct the differential phase-contrast signal for phase wrapping artefacts. One difficulty of this approach lays in the correct determination of correlations strength between the absorption signal and the phase signal. In 2012 Ritschl et al. [68] developed

those unwrapping approaches further and propose to reconstruct the unwrapped phase iteratively using an appropriate cost-function and the the visibility as a weight. A detailed investigation of those unwrapping algorithms has been done by Asbeck et. al [69].

In this chapter, an unwrapping method is derived to correct the systematic phase wrapping by utilizing the spectral information i.e. the energy dependency of the phase shift. First, the phase wrapping problem is introduced as it appears in the context of DPC imaging. Then, the general technique of maximum-likelihood estimation is introduced. After that, the probability density function (pdf) of the noise distribution in DPC imaging is theoretically derived. Since the true pdf is rather complicated, approximations are given and experimentally verified. Subsequently, a method for phase unwrapping is presented that utilizes the information contained in wrapped phase shifts, measured at different X-ray energies to estimate the true phase shift with a maximum-likelihood method. First, the technique is introduced for the particular case of multiple measurements with monochromatic X-rays, as they are available at synchrotron sources [70]. Then, the method is extended to polychromatic X-ray sources combined with an energy-discriminating photon-counting pixel detector [71]. The joined probability density function is derived by using the 'von Mises' distribution introduced in section 4.4, which describes the noise variation of the measured phase shifts including the appearance of statistical phase wrapping. Together with the modelled energy dependency, the method is capable of correcting phase-wrapping artefacts, and reducing beam hardening. It potentially leads to an improved contrast-to-noise ratio in the images.

4.2 Phase wrapping in differential-phase contrast imaging

In general, the phase of the wave or its relative shift, as it is the quantity of interest in DPC imaging, is never detected directly as a real signal, but needs to be extracted from the actually measured signal through a mathematical operation. In DPC imaging the fastest way to see the occurrence of phase wrapping during the phase extraction process is to use the linearised sinusoidal approximation

$$I(x) = A_0 + A_1 \cos(x) + B_1 \sin(x), \tag{4.1}$$

with the fit parameters A_0, A_1, and B_1 as a model to describe the acquired stepping curve. From the measured signal I, the interference-pattern phase shift Ψ can be extracted from the continuous values of A_1 and B_1 by applying the four-quadrant arctangent operator

$$\Psi = \arctan[\frac{B_1}{A_1}]. \tag{4.2}$$

This mathematical operation applied to the measured signal enforces Ψ to be bound to the interval $]-\pi, \pi]$, which introduces the ambiguities in the phase-shift values, known as the phase-wrapping problem. The correction of the extracted phase-shift values for the ambiguities is known as unwrapping. The actual process can be explained by considering the arctangent operator as a non-linear wrapping operator W:

$$\Psi = W[\varphi] \tag{4.3a}$$

$$= \varphi \operatorname{modulo} 2\pi, \tag{4.3b}$$

with φ being the unknown 'true' unwrapped phase shift of the interference pattern. Equation (4.3b) can be rewritten to

$$\Psi = \varphi + z\,2\pi \tag{4.4}$$

with $z \in \mathbb{Z}$ chosen so that

$$-\pi < \Psi \leq \pi. \tag{4.5}$$

Obviously, Ψ is a nonlinear function of φ, and Eq. (4.4) states that the unwrapping procedure consists of finding the correct value for z for each pixel.

The relation between the wavefront phase shift Φ, which is introduced by the object, and the appearance of phase wrapping in the measurement of the interference-pattern phase shift can be understood from the principals given in chapter 2.6. It was shown that the phase-shift Φ of the x-ray wavefront travelling through the specimen causes a deflection of the wavefront by an angle

$$\alpha = \frac{\lambda}{2\pi}\frac{\partial \Phi}{\partial x}, \tag{4.6}$$

where λ is the x-ray wavelength. The deflection leads to a shift S of the interference-pattern at the G_2 grating with period p_2, which causes a phase shift φ of the measured stepping curve given by

$$\varphi = \frac{2\pi}{p_2}S. \tag{4.7}$$

Due to the 2π periodicity of the stepping curve, the phase shift φ can be determined only within the limited interval $[-\pi, \pi[$. Thus, a shift S of the interference pattern larger than $\pm p_2/2$ leads to wrapping in the measured phase shift φ as given in Eq. (4.3b). As phase wrapping leads to strong artefacts in the extracted projection images and especially in the 3D reconstruction its correction is of high interest.

In addition to the systematical phase wrapping that occurs because of a too strong shift of the interference pattern, as described above, there exists the effect of statistical phase wrapping due to presence of noise. In the case of statistical phase wrapping, the wrapped stepping curve does not contain any information, i.e. Eq. (4.3b) cannot be applied, and thus, cannot be corrected.

4.3 Maximum-likelihood estimation of the unwrapped phase

In the following, a method is derived to correct the systematic phase wrapping, appearing in the differential phase data, that is motivated by parameter estimation methods proposed in MRI imaging [72, 73]. For this purpose, a set of phase shifts at different x-ray energies is measured and the maximum-likelihood method is used to estimate the unwrapped phase-shift value from this set of measurements. First, the general concept of the maximum-likelihood method is introduced, while a more detailed explanations can be found here Cowan et al. [74]. Subsequently the proposed unwrapping method is derived for monochromatic energies, as they are available at synchrotron- or compact light sources. After that, the unwrapping procedure is extended to conventional polychromatic x-ray sources, as they are used in laboratory setups, combined with an energy-sensitive detector.

4.3.1 Introduction | The maximum-likelihood method

The maximum-likelihood method is one of the most important techniques to obtain an estimation of an unknown parameter θ (or parameters $\boldsymbol{\theta} = (\theta_1, ..., \theta_m)$) from a known functional distribution $f(x, \theta)$ of a random and independent variable x. The variable x is measured n times generating a set of independent values $x_1, x_2, ..., x_n$. Since the measurement are completely independent from each other, the probability to obtain exactly this sample is given by the product

$$L := f(x_1, x_2, ..., x_n | \theta) = f(x_1 | \theta) \cdot f(x_2 | \theta) \cdot ... \cdot f(x_n | \theta), \qquad (4.8)$$

which is referred to as likelihood function with the parameter θ as an argument. Obviously, if the supposed distribution $f(x, \theta)$ and the parameter values are actually correct, one would expect a high probability for the measured values. A wrong parameter, on the other hand, would yield a low probability for the measurement. The maximum-likelihood method assumes now that a good estimate for the unknown parameter θ is given by the value $\hat{\theta}$ that maximizes the likelihood function given in Eq. (4.8). A necessary condition for L to have a maximum is the vanishing of its derivation with respect to θ:

$$\frac{\partial L}{\partial \theta} = 0. \qquad (4.9)$$

The solution $\hat{\theta}$, which depends on $x_1, x_2, ..., x_n$, is called the maximum-likelihood (ML) estimator of the parameter θ. Note that $\hat{\theta}$ is only an estimate of the true parameter θ, of which the exact value remains unknown because of random fluctuations, i.e. noise.
Instead of maximizing the likelihood function (4.8) it is often appropriate to maximize its logarithm in an equivalent manner:

$$\frac{\partial \ln(L)}{\partial \theta} = 0. \qquad (4.10)$$

Replacing L with $\ln(L)$ is a strictly monotonic increasing transformation, and the parameter value that maximises L also maximises $\ln(L)$. Maximizing the logarithm has the advantage that the product in L is transformed into a sum, and exponential functions in $f(x, \theta)$ are converted to simple factors.

In the following this technique is used to correct the DPC data for phase wrapping artefacts.

4.4 Probability density function in differential phase measurements

For the maximum-likelihood estimation explained in section (4.3.1) the probability density function for the noise distribution in grating-based phase-contrast imaging needs to be known. In general, the noise in a differential phase-contrast (DPC) image does not obey a Gaussian probability density function as it is the case in conventional X-ray attenuation images. In this chapter, an estimation of the true probability density function for the noise in differential phase-contrast images is given. It will be shown that the 'von Mises' distribution can be taken as a good approximation. Further, it will be demonstrated, that the Gaussian probability density function can be applied for DPC images in the limit of a high signal-to-noise ratio.

The sinusoidal approximation of the intensity curve I, Eq. (2.28), with mean value a_0, amplitude a_1 and phase shift φ can be linearised in the following way [75]:

$$I(x) = a_0 + a_1 \sin(x + \varphi), \tag{4.11a}$$
$$= A_0 + A_1 \cos(x) + B_1 \sin(x). \tag{4.11b}$$

The new fit parameters are the mean value A_0 and the amplitudes A_1 and B_1. The initial parameters a_0, a_1 and φ can be regained by:

$$a_0 = A_0, \qquad a_1 = \sqrt{A_1^2 + B_1^2}, \qquad \varphi = \arctan\left(\frac{B_1}{A_1}\right). \tag{4.12}$$

Further, the visibility V can be recovered by:

$$V = \frac{a_1}{a_0} = \frac{\sqrt{A_1^2 + B_1^2}}{A_0}. \tag{4.13}$$

After the linearisation, A_1 and B_1 can be expressed in polar coordinates:

$$A_1 = r\cos(\varphi), \ B_1 = r\sin(\varphi) \text{ with } r = \sqrt{A_1^2 + B_1^2} = V A_0. \tag{4.14}$$

In order to obtain an estimation for the uncertainty of the fit parameters, a sufficient SNR is assumed that allows to approximate the uncertainty of a_1 to be Gaussian distributed with $\sigma_{a_1}^2 = \frac{1}{2}a_0^2$ [76]. It has been shown by Weber et al. [9] that noise in the differential phase image is independent of the absorption and dark-field image. Therefore, the ap-

proximation that also the uncertainties of the fit parameters A_1 and B_1 to be Gaussian distributed can be used, with the probability density functions

$$f_{A_1}(\bar{A}_1, \sigma_{A_1}^2) = \frac{1}{\sqrt{2\pi}\sigma_{A_1}} \exp\left(-\frac{(A_1 - \bar{A}_1)^2}{2\sigma_{A_1}^2}\right), \tag{4.15a}$$

$$f_{B_1}(\bar{B}_1, \sigma_{B_1}^2) = \frac{1}{\sqrt{2\pi}\sigma_{B_1}} \exp\left(-\frac{(B_1 - \bar{B}_1)^2}{2\sigma_{B_1}^2}\right), \tag{4.15b}$$

with the mean values $\bar{A}_1$, $\bar{B}_1$ and the respective variances $\sigma_{A_1}^2 = \frac{1}{4}A_0^2$ and $\sigma_{B_1}^2 = \frac{1}{4}A_0^2$. Using this, one can formulate the joined probability density function (pdf) $f(\bar{A}_1, \sigma_{A_1}^2, \bar{B}_1, \sigma_{B_1}^2)$ and calculate the pdf $f^*(r, \varphi)$ for the introduced polar coordinates:

$$f^*(r, \varphi) = \det J \, f(\bar{A}_1, \sigma_{A_1}^2, \bar{B}_1, \sigma_{B_1}^2) \tag{4.16a}$$

$$= r \frac{1}{2\pi\sigma^2} \exp\left(-\frac{(A_1 - \bar{A}_1)^2}{2\sigma^2}\right) \exp\left(-\frac{(B_1 - \bar{B}_1)^2}{2\sigma^2}\right), \tag{4.16b}$$

where the determinant of the Jacobi matrix $\det J = \sqrt{A_1^2 + B_1^2} = V A_0 = r$ and $\sigma_{A_1}^2 = \sigma_{B_1}^2 = \sigma^2$ was used. Equation (4.16b) can be written as:

$$f^*(r, \varphi) = r \frac{1}{2\pi\sigma^2} \exp\left[-\frac{1}{2\sigma^2}(A_1^2 + B_1^2 + \bar{A}_1^2 + \bar{B}_1^2 - 2(A_1\bar{A}_1 + B_1\bar{B}_1))\right] \tag{4.17a}$$

$$= r \frac{1}{2\pi\sigma^2} \exp\left[-\frac{1}{2\sigma^2}(r^2 + \bar{V}^2\bar{A}_0^{\,2} - 2r(\vec{\mathbf{x}} \cdot \vec{\bar{\mathbf{x}}}))\right], \tag{4.17b}$$

with $\bar{A}_1^2 + \bar{B}_1^2 = \bar{V}^2\bar{A}_0^2$, $\vec{\mathbf{x}} = (\sin(\varphi), \cos(\varphi))^T$, and $\vec{\bar{\mathbf{x}}} = (\bar{B}_1, \bar{A}_1)^T$. Finally, the probability density function for the phase shift φ is obtained by integrating Eq. (4.17b) with respect to r:

$$f^*(\varphi) = \frac{1}{2\pi\sigma^2} \int_0^\infty r \exp\left[-\frac{1}{2\sigma^2}(r^2 + \bar{V}^2\bar{A}_0^{\,2} - 2r(\vec{\mathbf{x}} \cdot \vec{\bar{\mathbf{x}}}))\right] \mathrm{d}r \tag{4.18a}$$

$$= \frac{1}{2\pi} \exp\left(-\frac{\bar{V}^2\bar{A}_0^{\,2}}{2\sigma^2}\right)$$

$$+ \frac{1}{\sqrt{8\pi}}\sqrt{\frac{1}{\sigma^2}}(\vec{\mathbf{x}} \cdot \vec{\bar{\mathbf{x}}}) \exp\left[\frac{1}{2\sigma^2}((\vec{\mathbf{x}} \cdot \vec{\bar{\mathbf{x}}})^2 - \bar{V}^2\bar{A}_0^{\,2})\right]$$

$$+ \frac{1}{\sqrt{8\pi}\sigma}(\vec{\mathbf{x}} \cdot \vec{\bar{\mathbf{x}}}) \exp\left[\frac{1}{2\sigma^2}((\vec{\mathbf{x}} \cdot \vec{\bar{\mathbf{x}}})^2 - \bar{V}^2\bar{A}_0^{\,2})\right] \operatorname{erf}\left(\frac{(\vec{\mathbf{x}} \cdot \vec{\bar{\mathbf{x}}})}{\sqrt{2}\sigma}\right). \tag{4.18b}$$

Here, $\operatorname{erf}(x)$ denotes the error function that is defined as:

$$\operatorname{erf}(x) = \frac{2}{\sqrt{\pi}} \int_0^x \exp(-t^2) \, \mathrm{d}t. \tag{4.19}$$

For a further analysis, without loss of generality, the true phase shift can be set to be $\varphi_0 = 0$, which represents for instance the phase-shift distribution in a flat-field DPC image. This assumption allows to simplify the scalar product to

$$(\vec{\mathbf{x}} \cdot \vec{\mathbf{x}}) = \bar{V} \bar{A}_0 \cos(\varphi), \tag{4.20}$$

and leads to an estimation of the probability density function $f^*(\varphi)$ that is centered around zero:

$$f^*(\varphi) = \frac{1}{2\pi} e^{\left(-\frac{\bar{V}^2 \bar{A}_0^2}{2\sigma^2}\right)} \left[1 + \sqrt{\frac{\pi}{2}} \frac{\bar{V} \bar{A}_0}{\sigma} \cos(\varphi) e^{\left[\frac{1}{2\sigma^2} \bar{V}^2 \bar{A}_0^2 \cos^2(\varphi)\right]} \left(1 + \mathrm{erf}\left(\frac{\bar{V} \bar{A}_0 \cos(\varphi)}{\sqrt{2}\sigma}\right)\right)\right]. \tag{4.21}$$

In the following the probability density function given in Eq. (4.21) is referred to as the 'true probability density function'.

4.4.1 Approximations | 'von Mises' and Normal distribution

The probability density f^* given in Eq. (4.21) is rather complicated for practical use. Therefore, it is demonstrated that the much simpler 'von Mises' distribution f_{vm} can be employed as a good approximation to describe the uncertainty in DPC measurements, as suggested by Weber et al. [9]. Further it is shown that for a sufficient data quality a further simplification can be made by using the Normal distribution f_n, as give in Eq. (4.15a).

Approximation using the 'von Mises' probability density function:
The 'von Mises' distribution f_{vm} is given by

$$f_{vm}(\varphi|\bar{\varphi}, \kappa) = \frac{1}{2\pi I_0(\kappa)} \exp(\kappa \cos(\varphi - \bar{\varphi})), \tag{4.22}$$

with the mean value $\bar{\varphi}$, the modified Bessel function of order zero $I_0(\kappa)$ and κ beeing a measure for the concentration, which is analogous to the variance σ^2 of the Normal distribution f_n. Figure 4.1 depicts the 'von Mises' distribution for different concentration values κ. Figure 4.2 shows the true pdf for different ratios V/σ and its respective approximations by a least squares optimization if the 'von Mises' distribution regarding the parameter κ. It demonstrates that the 'von Mises' distribution approximates the distribution f^* very well for all ratios of V/σ, that are of practical interest in this work, and that both distributions are equal for a sufficient data quality. Further, Fig. 4.3 (a) depicts that a proportional relation between κ and σ^2 is valid for small variances:

$$\frac{1}{\kappa} = \sigma^2 \qquad \text{if} \qquad \sigma^2 \lesssim 0.2. \tag{4.23}$$

Thus, as long as the variance is small enough, it is possible to use the 'von Mises' distribution as an approximation of the probability density function with an inverse concentration $1/\kappa$ equal to the simple-to-determine variance σ^2.
The error between f^* and f_{vm} relative to the total area of f^* as a function of σ^2 is shown
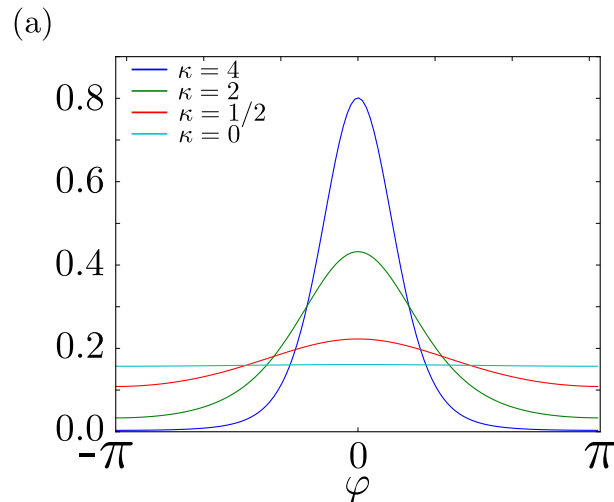
(a)

Figure 4.1: Plot of the 'von Mises' distribution for different concentration values κ.

in Fig. 4.3 (b). The green curve represents the error made with the assumption that Eq. (4.23) is valid for all variances and the blue curve represents the error made with a κ obtained by a least-squares optimization. As expected, the error made is in general small and for variances $\sigma^2 \lesssim 0.2$ sufficiently similar in both cases. For variances $\sigma^2 > 0.2$ the error of the least-squares optimized case increases slower, however in both cases there is a maximal error at a certain noise level. The maximum occurs, since both probability density functions f^* and f_{vm} converge to the uniform distribution

$$U(\varphi) = \frac{1}{2\pi} \approx 0.159 \tag{4.24}$$

for $\sigma^2 \gg 0.2$ or $\kappa \approx 0$, as shown in Fig. 4.1. The maximal error that can be made using the 'von Mises' distribution as an approximation, is 6 % relative to the area of the probability density function. If the κ is used, the maximal error decreases to only 0.3 %, which converges to zero for variances $\sigma^2 \gtrsim 3$.

Approximation with the Normal probability density function:
A further simplification can be made with the Normal distribution given in Eq. (4.15a). Figure 4.4(a) depicts the relative error made when using the Normal distribution with the same σ^2 as for the probability function f^*. The gradient of the relative error shown in Fig. 4.4(b)) has a maximum at at $\sigma^2 \approx 0.5$, which marks the noise level to which the Normal distribution can be used to approximate f^*. While for $\sigma^2 < 0.5$ the Normal distribution is a good approximation with an relative error less than one percent (Fig. 4.4(c)) it is not for larger variances. The main reason for the larger relative error for large variances is that the tails of the 'von Mises' distribution do not converge any more to 0 as can be seen in Fig. 4.4(d). This behaviour can not be modeled with a Normal distribution, which always converges to zero.

With that, one can determine the minimal statistics (counts) that is needed to be able to apply a Normal-distributed model to the data. For the calculation, it is assumed
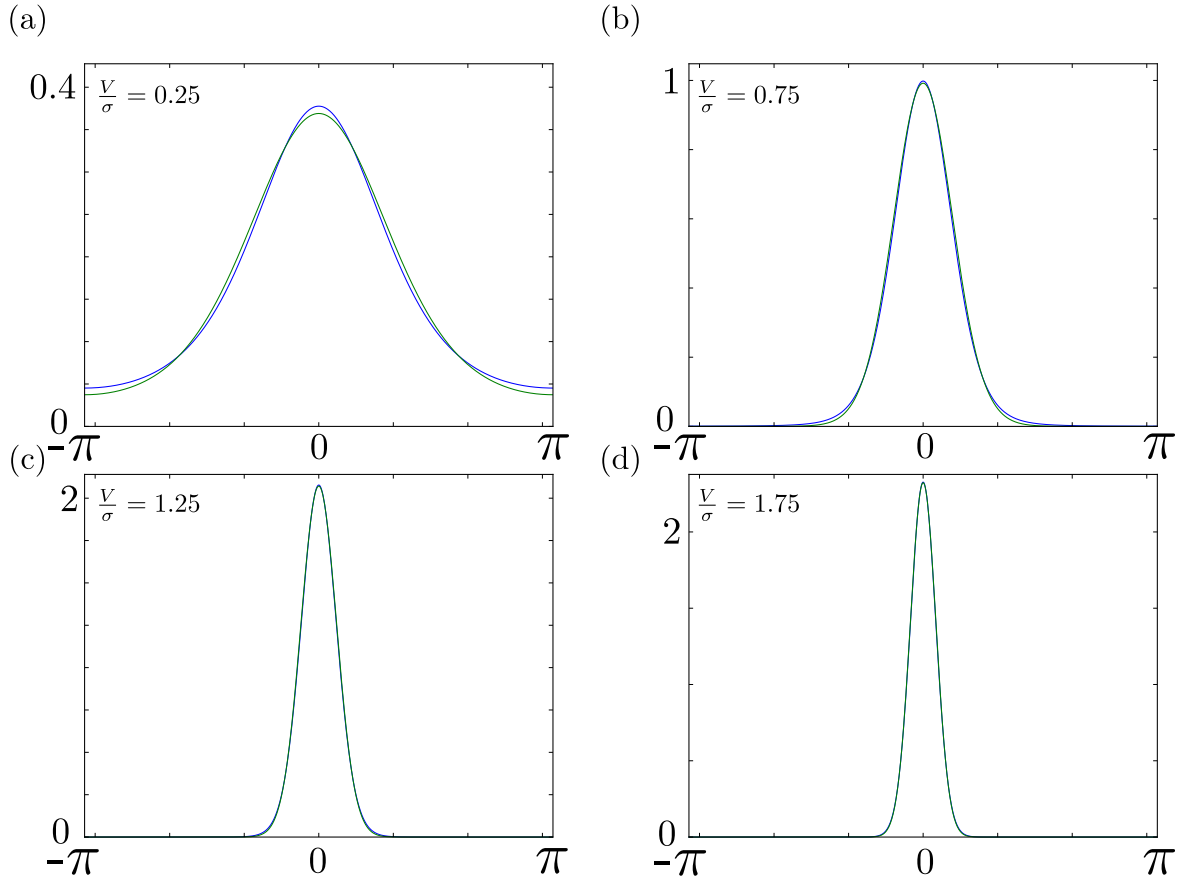
(a)

(b)

(c)

(d)

Figure 4.2: Approximation of the true distribution f^* with the 'von Mises' distribution f_{vm} with a concentration κ determined by a least squares fit for different V/σ values. The 'von Mises' distribution approximates the distribution f^* for all ratios of V/σ relevant for this work.

$\sigma^2 = 1/NV^2$ to be a valid model for the variances in DPC images with N being the number of photons counted with the detector and V the visibility of the interferometer. With an average visibility of $V = 20\,\%$, it is possible to use the Normal distribution as a good approximation, if the detector records $N \gtrsim 250$ counts per pixel.
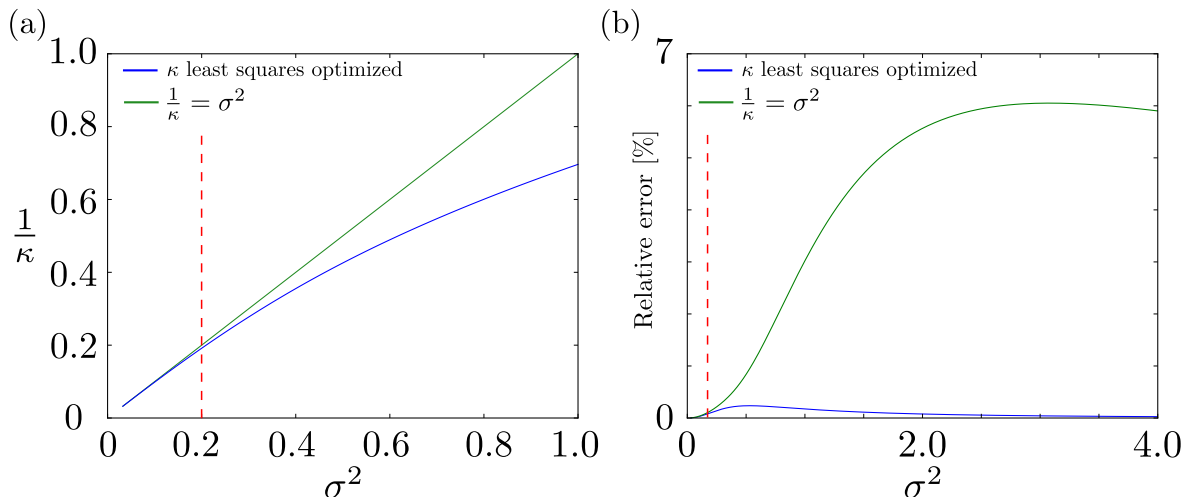
Figure 4.3: Approximation with 'von Mises' distribution. (a) Relation between $1/\kappa$ and σ^2. The green curve shows a linear relation. The blue curve shows the fitted relation using least squares optimization. (b) Relative error between $1/\kappa$ and σ^2 with the least squares optimization. For small variances $\sigma^2 < 0.2$ the von Mises distribution can be used as a good approximation and the inverse concentration $1/\kappa$ can be assumed equal to the simple-to-determine variance σ^2 of a Normal distribution.

4.4.2 Experimental verification

For an experimental verification flat-field (i.e. without object) DPC measurements were performed with varying exposure times to obtain different noise levels σ^2 in the images. The histograms of the DPC images acquired with exposure times of 3.6, 0.1, 0.05 and 0.02 s are shown in Fig. 4.5(a)-(d), respectively. The histograms were fitted with the Normal distribution $f_n(\mu, \sigma)$, the 'von Mises' distribution $f_{vm}(\mu, \kappa)$, and the probability density function $f^*(V, \mu, \sigma)$ with $V = 20\,\%$.

Figure 4.5(a) depicts the case of a very low noise level with $\sigma^2 = 0.04$ were all three pdf's are identical and fit the histogram perfectly. The distribution slightly differs at the tails and the maximum of the distribution, but as long as the noise level is lower than the predicted limit of $\sigma^2 \approx 0.5$, the differences between the Normal and the 'von Mises' distribution are negligible, as illustrated in Fig. 4.5 (b). For variances above $\sigma^2 \approx 0.5$, the Normal distribution is not able to fit the non-zero tails and the maximum value correctly, see Fig. 4.5(c). The 'von Mises' distribution fits the histogram much better but is not able to perfectly describe the maximum and the non-zero tails either. The difference between the 'von Mises' and the true distribution increases with an increasing variance, see Fig. 4.5 (d). Nevertheless, a variance of $\sigma^2 \approx 0.66$ that was obtained with an exposure time of 0.02 s leads to images, which are probably unusable for most applications, see Fig. 4.5 (d). As the differences between the three pdf's are small, one can conclude that a 'von Mises' distribution can be used to approximate the distribution for variances below $\sigma^2 \approx 1$ and that the Normal distribution serves as a very good approximation for variances below $\sigma^2 \approx 0.5$.
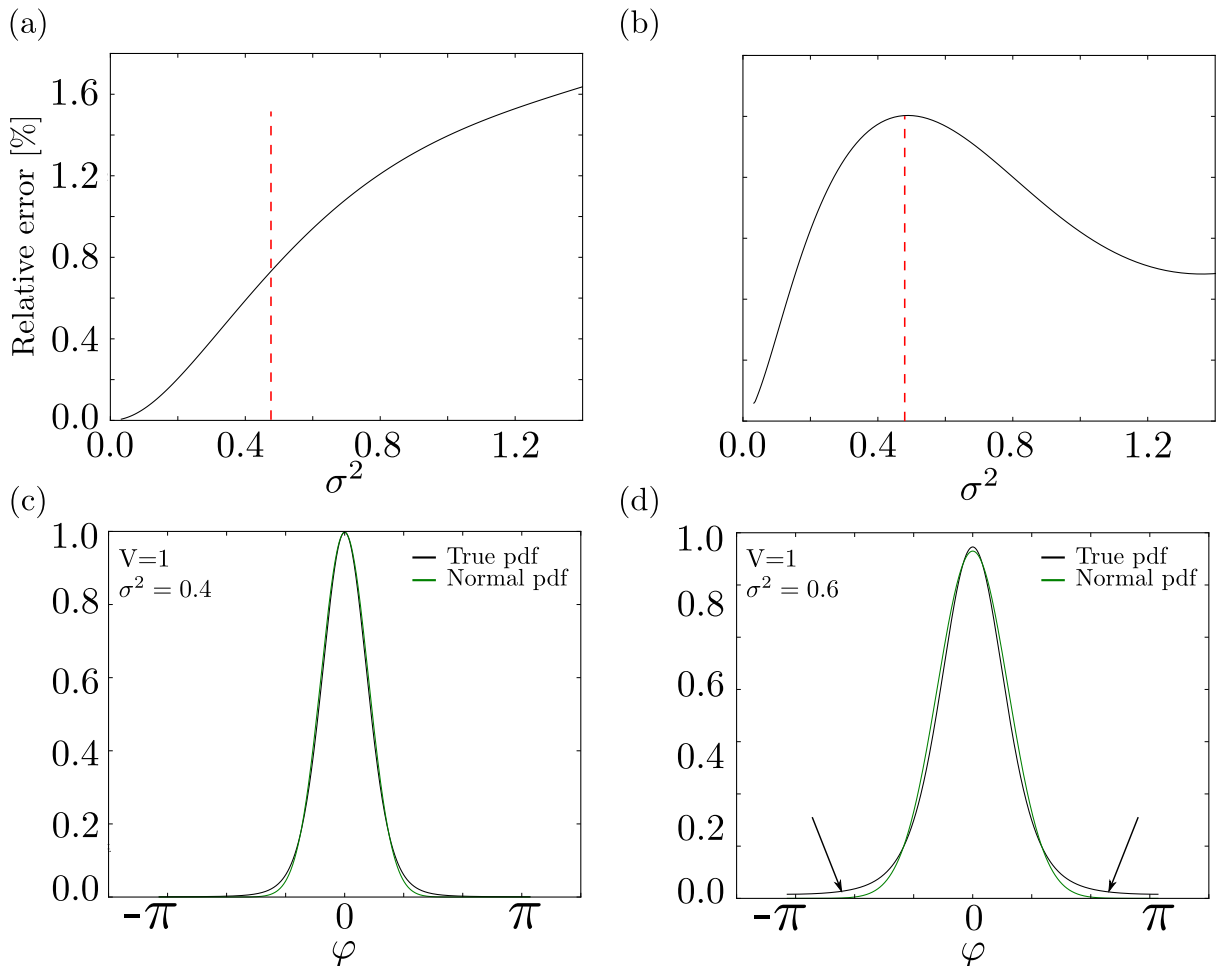
Figure 4.4: Approximaton of the true probability density function with the Normal distribution. (a) Relative error when using the same σ^2 for both distributions. (b) Gradient of the relative error. It has a maximum at $\sigma^2 \approx 0.5$. (c) Approximation with $\sigma^2 < 0.5$, where the Normal distribution approximates the 'von Mises' distribution very well with an relative error less then one percent. (d) Approximation with $\sigma^2 > 0.5$ where the approximation starts to fail due to the non-zero tails of the 'von Mises' distribution that can not be fitted with the Normal distribution.
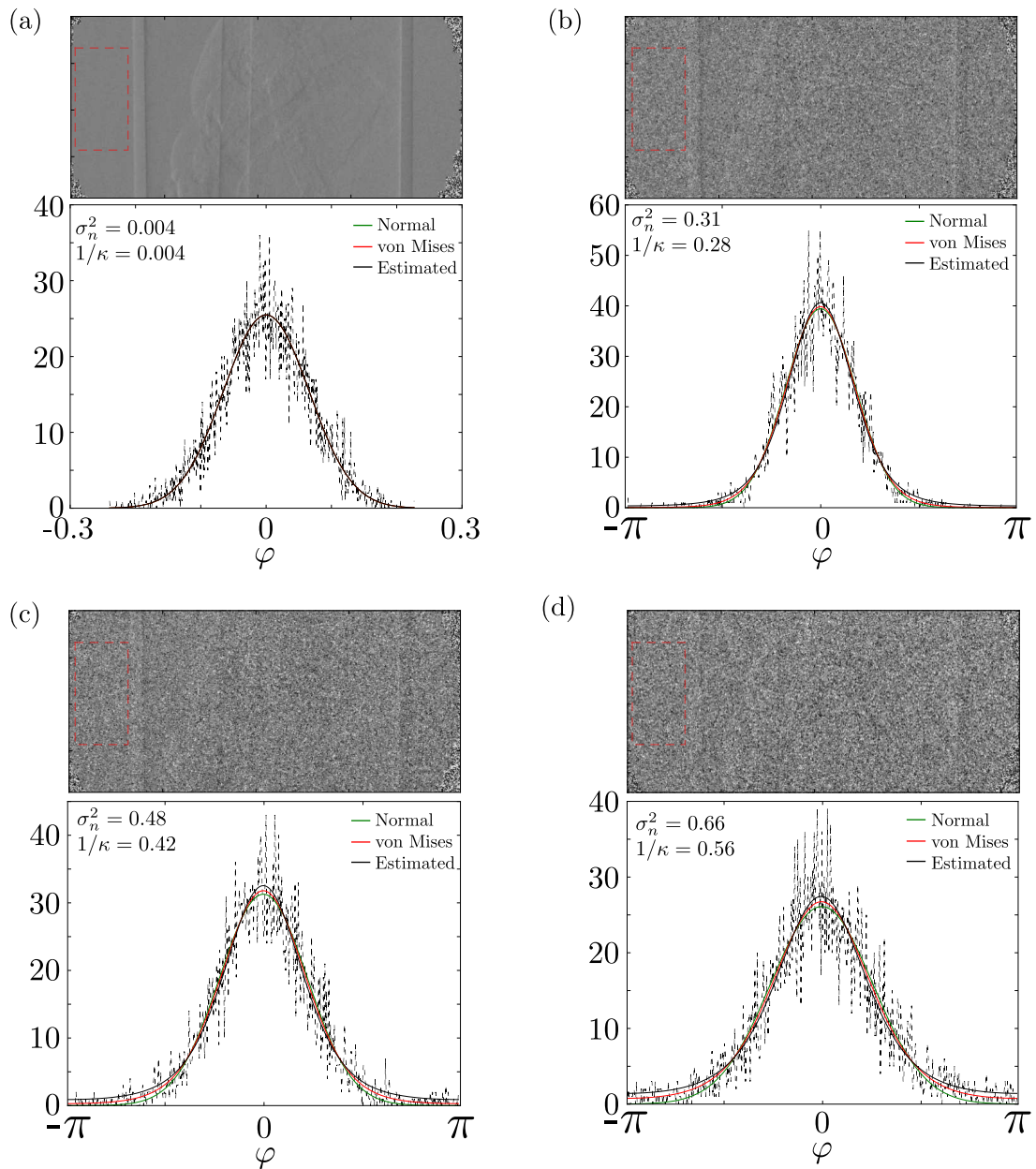
Figure 4.5: Comparison of the true (estimated), the 'von Mises', and the Normal distributions applied to real data sets with different noise levels. (a) - (b) For low and median noise levels, all three distributions fit the real data very well. (c) The Normal distribution is not able to fit the non-zero tails and the maximum value correctly. Also 'von Mises' distribution slightly underestimates the maximum and the non-zero tails. (d) The difference between the 'von Mises' and the true distribution increases with an increasing variance, but the total difference is still small as shown in section 4.4.1.

4.5 Spectral phase unwrapping | With multiple monochromatic X-ray measurements

Synchrotron X-ray sources provide an X-ray beam with with high monochromaticity, i.e. lower band width $\Delta E/E \sim 10^{-1}$. The strength of the phase shift $\varphi(x, y, E)$ varies with E and is given by:

$$\varphi(x, y, E) = \frac{r_e d}{p_2} \left(\frac{hc}{E}\right)^2 \frac{\partial}{\partial x} \int \varrho_e(x, y, z) \, dz. \tag{4.25}$$

A specially designed X-ray interferometer implemented by Herzen at al. [77] allows to repeat the same measurement with different X-ray energies while keeping the interferometer geometry fixed. If the measurement is repeated n times with distinct energies E_i with $i = 1, 2, ..., n$, a data set with n independent phase-shift values $\varphi_1, \varphi_2, ..., \varphi_n$ is obtained. Due to the appearance of noise, the obtained phase shifts obey very well the 'von Mises' distribution $f(\varphi_i, \bar{\varphi}_i, \kappa_i)$, as described in section 4.4, is given by

$$f(\varphi_i, \bar{\varphi}_i, \kappa_i) = \frac{1}{2\pi I_0(\kappa_i)} e^{\kappa_i \cos(\varphi_i - \bar{\varphi}_i)}. \tag{4.26}$$

Here, $\bar{\varphi}_i$ is the expectation value, κ_i the concentration and $I_0(\kappa_i)$ the modified Bessel function of order zero. It is worth to mention that in the case of small variances with $\sigma_i^2 \lesssim 0.2$, the concentration κ_i of the distribution can be approximated by [14]:

$$\frac{1}{\kappa_i} \approx \sigma_i^2 = \frac{2}{N_{0_i} V_{0_i}^2} + \frac{2}{N_{S_i} V_{S_i}^2}, \tag{4.27}$$

as shown in section 4.4. Here, N_{0_i} and V_{0_i} are the number of x-ray photons and the visibility without a sample, respectively and N_{S_i} and V_{S_i} are the corresponding values with a sample in the beam. Note that the variance σ_i^2 depends not only on the number of X-ray photons N, as it is the case for conventional absorption images, but even stronger on the visibility V [78].

The unknown parameter that needs to be estimated is the expectation $\bar{\varphi}_i$, which up to now is an energy dependent value. However, since the energy dependence in Eq. (4.25) appears only as a pre-factor, it follows that the quantity $E^2\varphi$ is an energy invariant. It therefore suffices to define the model as a function of some phase φ^* at some energy E^* (for instance that corresponding to the lowest energy E_1):

$$\varphi^* = \frac{r_e d}{p_2} \left(\frac{hc}{E^*}\right)^2 \frac{\partial}{\partial x} \int \varrho_e(x, y, z) \, dz, \tag{4.28}$$

and to model the expectation for all energies through a rescaling of this phase reference by

$$\bar{\varphi}_i = \frac{E^{*2}}{E_i^2} \varphi^*, \tag{4.29}$$

and the probability distribution with an energy invariant mean:

$$f(\varphi_i, \bar{\varphi}_i, \kappa_i) = \frac{1}{2\pi I_0(\kappa_i)} e^{\kappa_i \cos(\varphi_i - \frac{E^{*2}}{E_i^2}\varphi^*)}. \tag{4.30}$$

As measurements of the phase shifts at the distinct energies are statistically independent, the likelihood function L is given by

$$L = f(\varphi_1, \kappa_1, \varphi_2, \kappa_2, ..., \varphi_n, \kappa_n | \frac{E^{*2}}{E_1^2}\varphi^*, \frac{E^{*2}}{E_2^2}\varphi^*, ..., \frac{E^{*2}}{E_n^2}\varphi^*) \tag{4.31a}$$

$$= \prod_{i=1}^{n} f(\varphi_i, \kappa_i | \frac{E^{*2}}{E_i^2}\varphi^*) \tag{4.31b}$$

$$= \prod_{i=1}^{n} \frac{1}{2\pi I_0(\kappa_i)} \exp\left(\kappa_i \cos(\varphi_i - \frac{E^{*2}}{E_i^2}\varphi^*)\right). \tag{4.31c}$$

As described in section 4.3.1, instead of maximizing Eq. (4.31c), the maximum-likelihood estimator $\hat{\varphi}^*$ can be obtained, which is an estimate of the 'true' unwrapped phase shift, by minimizing its negative logarithm. Neglecting the irrelevant terms, which do not depend on the parameter φ^*, the negative log-likelihood function is obtained:

$$\ell(\varphi^*) = -\log(L) \tag{4.32a}$$

$$\propto -\sum_i \kappa_i \cos\left(\varphi_i - \frac{E^{*2}}{E_i^2}\varphi^*\right), \tag{4.32b}$$

where the product of exponential function changes to a sum of cosines. With that the maximum-likelihood estimator $\hat{\varphi}^*$ can be found by minimizing Eq. (4.32b):

$$\hat{\varphi}^* = \underset{\varphi^*}{\arg\min}(\ell(\varphi^*)). \tag{4.33}$$

Due to the oscillating terms, the log-likelihood function (4.32b) has several local minima with respect to φ^* if the support (i.e. range of possible values of φ^*) allows multiple periods. In this case, the global minimum of Eq. (4.32b) is taken as maximum-likelihood estimator $\hat{\varphi}^*$.

4.5.0.1 Regularization

Empirically, it is found that an estimator $\hat{\varphi}^*$ corresponding to a local minimum at smaller values of φ^* is more probable than one at larger values. This can be violated in the estimation, for example due to the presence of noise, if the number of distinct energies is too small or if the spectral range covered by the energies is too narrow. In order to
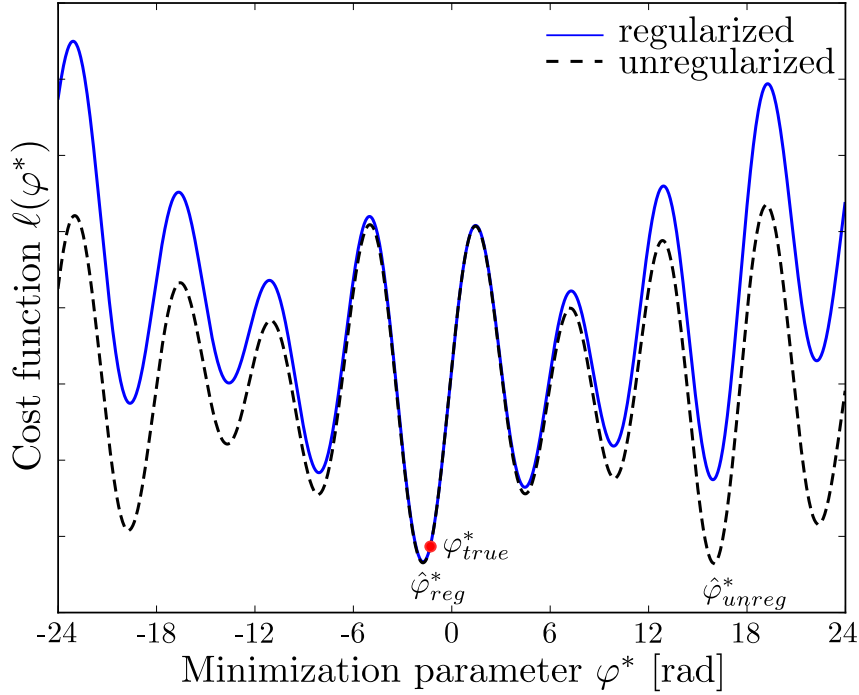
Figure 4.6: Exemplary cost function $\ell(\varphi^*)$ with (continuous line) and without (dashed line) regularization $R(\varphi^*)$. In order to illustrate the effect of the regularization, the cost function from a pixel without phase wrapping is shown. For this pixel a true phase shift of $\varphi^*_{true} = 1.4\,\mathrm{rad}$ (marked with the red dot) should be found. The global minimum at $\varphi^*_{unreg} = 15.9\,\mathrm{rad}$ appearing in the unregularized cost function is wrong, for example, because of the limited number or not optimally chosen energy windows. The regularization $R(\varphi^*)$ adds a preference for small values of φ^* and leads to a minimum at $\varphi^*_{reg} = 1.9\,\mathrm{rad}$.

account for the empirical observation a regularization $R(\varphi^*)$ is added to Eq. (4.32b):

$$\ell(\varphi^*) \propto - \sum_i \kappa_i \cos\left(\varphi_i - \frac{E^{*2}}{E_i^2} \varphi^* \right) + R(\varphi^*). \tag{4.34}$$

In general, different regularization strategies might be possible. For instance, if Eq. (4.34) is minimized restricted to a finite interval of φ^*, the regularization can be chosen to be

$$R(\varphi^*) = \gamma \varphi^{*2} \sum_i \kappa_i. \tag{4.35}$$

Here the factor γ depends on the experimental conditions, while the total range of φ^* and the weighting factors κ_i keep the relative influence of the regularization equal for all pixels. Thus, the final cost function f_c is given by

$$f_c(\varphi^*) = - \sum_i \kappa_i \cos\left(\varphi_i - \frac{E^{*2}}{E_i^2} \varphi^* \right) + \gamma \varphi^{*2} \sum_i \kappa_i, \tag{4.36}$$

which needs to be minimized with respect to φ^* to obtain an estimator $\hat{\varphi}^*$ for the un-wrapped phase shift:

$$\hat{\varphi}^* = \arg\min_{\varphi^*} \left(-\sum_i \kappa_i \cos\left(\varphi_i - \frac{E^{*2}}{E_i^2}\varphi^*\right) + \gamma\varphi^{*2}\sum_i \kappa_i \right). \tag{4.37}$$

In order to illustrate the effect of regularization, an exemplary cost function of a pixel of a DPC image where no phase wrapping appeared, is shown in Fig. 4.6. The pixel has a true, energy-independent phase shift of $\varphi^*_{true} = 1.4\,\text{rad}$. Instead, the unregularized cost function (dashed curve) has its global minimum at $\varphi^*_{unreg} = 15.9\,\text{rad}$. With regularization (continuous curve) a preference is added for small values of φ^*, which leads to an estimated value of $\varphi^*_{reg} = 1.9\,\text{rad}$.

4.5.1 Experimental verification

In order to verify the unwrapping method, we performed tomographic measurements of a plastic (PTFE) cube test sample at different monochromatic X-ray energies at the beamline HARWI II, operated by the Helmholtz-Zentrum Geesthacht, at the synchrotron DESY in Hamburg. The results were published in [70] and are described in the following. Because of the strong edges of the cube, strong phase wrapping occurs, if the angle between the facets of the cube and the incoming x-rays becomes small. This leads to strong artefacts in the reconstruction and consequently, makes a cubic object difficult to measure in a tomographic differential phase-contrast scan. The DPC measurements were performed at a Talbot-Lau interferometer than can be operated at different Talbot orders by changing the x-ray energy but keeping the interferometer geometry constant [77]. The inter-grating distances were $l = 3.0\,\text{m}$ between the source and the phase grating, and $d = 0.32\,\text{m}$ between the phase and the analyzer grating. The periods of the gratings were $p_0 = 22.3\,\mu\text{m}$, $p_1 = 4.33\,\mu\text{m}$ and $p_2 = 2.4\,\mu\text{m}$ for the source, phase, and analyzer grating, respectively. The interferometer showed reasonable performance (i.e. high visibility) at energies of 24 keV, 30 keV, and 48 keV, which were therefore chosen for the measurements. For each tomography scan we took 301 projections, equally spaced over 360°, while each projection was taken with 4 phase steps and an exposure time of 2 s per step. For the image acquisition a 580 μm thick CdWO4 scintillator lens-coupled to a CCD camera with an effective pixel size of 10 μm was used.

Figure 4.7(a)-(d) (second and third row) depicts the projection images and respective line plots of the phase shift φ measured at an x-ray energy of 24 keV for different rotation angles $\alpha = 44.2°, 11.9°, 5.9°, 3.6°$. As can be seen, only the regions indicated with white and black triangles of the cube lead to a positive or negative phase shift, respectively. In the gray region, the object phase shift Φ is constant and thus, no phase shift of the stepping curve occurs as it follows the relation

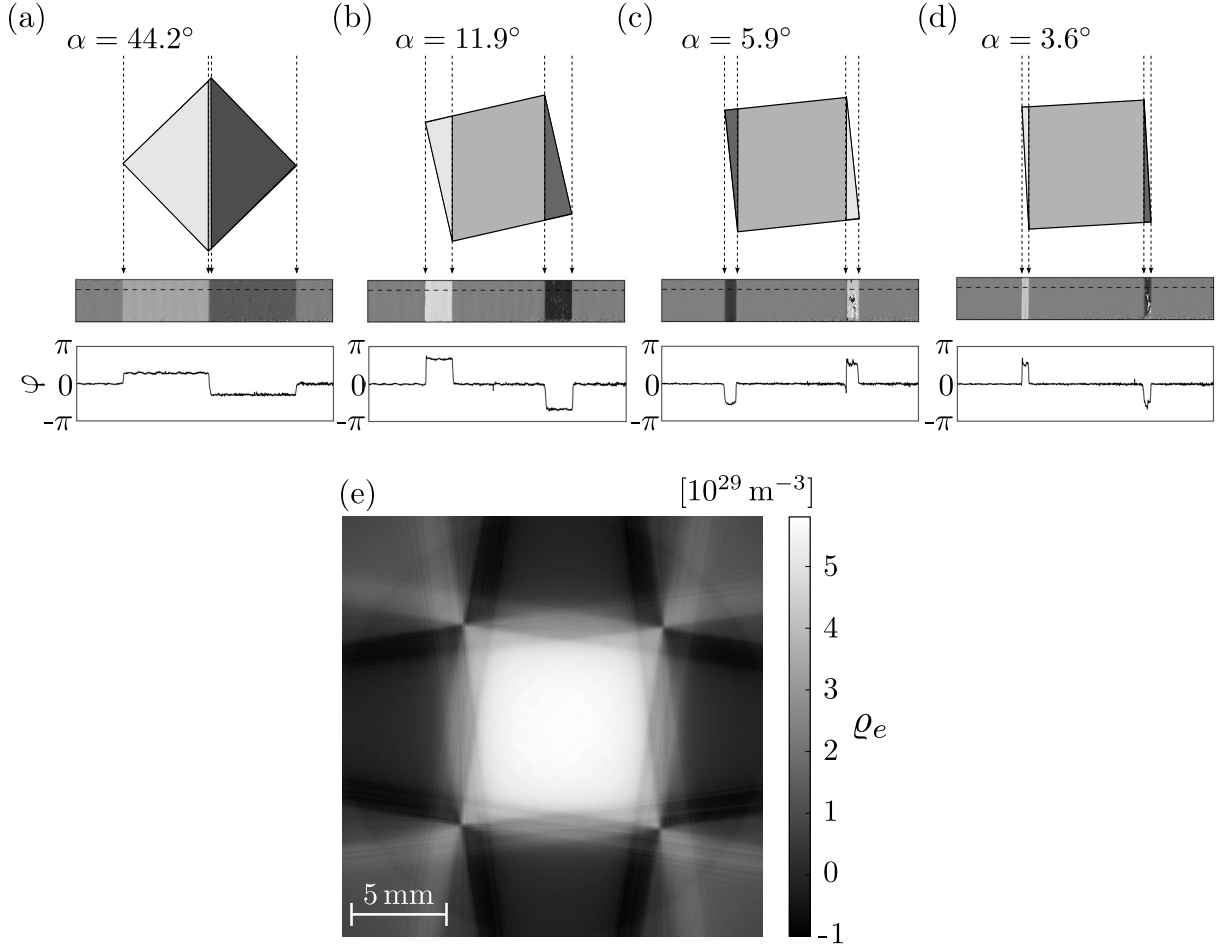$$\varphi = \frac{d\lambda}{p_2}\frac{\partial\Phi}{\partial x}. \tag{4.38}$$

Figure 4.7: The top row in (a)-(d) depicts illustrations from the top view of a cube at different rotation angles α. The middle row show the corresponding differential phase-contrast projection images. The bottom row provides the line plots along the dashed horizontal line in the respective projection. The effect of phase wrapping can be seen in (c) and (d) where the contrast of the left and right facet has flipped in between. (e) shows a slice from the 3D reconstruction, which is strongly corrupted by streak artifacts due to the phase wrapping.

Due to the increasing gradient of the facets the phase shift φ increases as the cube is rotated. Phase wrapping could be observed at rotation angles smaller than $\alpha < 8°$, see Fig. 4.7(c) and (d). At those angles the measured phase shift is not anymore proportional to the actual differential phase shift of the object as expressed by Eq. (4.38). The attempt of a tomographic reconstruction with filtered backprojection of a data set containing such phase wrapping artefacts is corrupted by strong streak artefacts, which leads to a blurring of the edges, as can be seen in Fig. 4.7(e).

In order to correct the projection images for the phase wrapping artefacts we employed the proposed unwrapping technique with 24 keV, 30 keV and 48 keV. Equation (4.37) was minimized by testing regularly spaced values of φ^* so that the range was large enough to
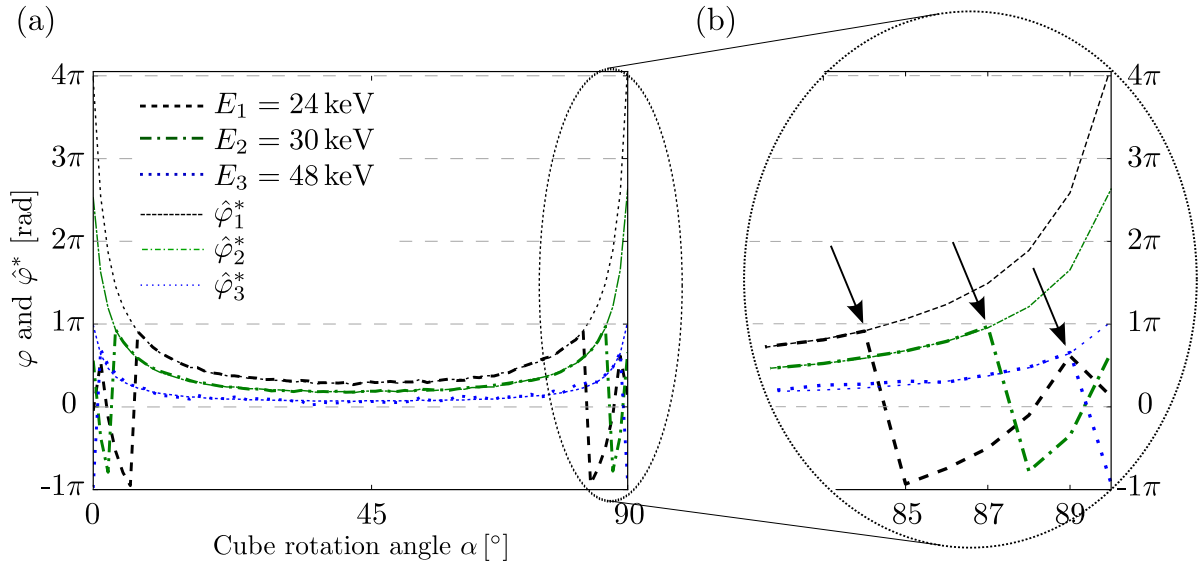
Figure 4.8: The interference-pattern phase shifts φ for $E_1 = 24\,\text{keV}$ (thick black), $E_2 = 30\,\text{keV}$ (thick green), and $E_3 = 48\,\text{keV}$ (thick blue) together with the corresponding estimated interference-pattern phase shifts $\hat{\varphi}_1^*$, $\hat{\varphi}_2^*$, and $\hat{\varphi}_3^*$ (thin lines) for all x-ray wavelengths from a single pixel over a $90°$ rotation of the cube. b) Zoom into the area where phase wrapping, indicated by arrows, occurs. Note that phase wrapping could be corrected even at angles where each individual signal had wrapped.

cover a potential phase-wrapping up to eight periods. The regularization R was implemented as proposed in Eq. (4.35) with a global factor $\gamma = 4 \times 10^5 \,\text{rad}^{-2}$. As an example, in Fig. 4.8 the measured interference pattern phase shift φ_i for all x-ray energies as well as the corresponding estimated values $\hat{\varphi}_i^*$ for a rotation of the cube from $0°$ to $90°$ are depicted for one pixel and the unwrapping result is shown.

The angles, at which phase wrapping occurs, are indicated by arrows. Beside the gradient of the facets, the strength of the interference-pattern phase shift φ depends on the X-ray energy as given in Eq. (4.25). Since φ decreases with increasing energy, phase wrapping tends to occur at smaller angles for higher energies but at a rotation angle of $1.6°$ the signal has wrapped at even the highest energy. Nevertheless, a good estimation $\hat{\varphi}^*$ could be obtained.

Figure 4.9 shows line plots of the measured interference-pattern phase shift φ at $24\,\text{keV}$ and the estimated interference-pattern phase shift $\hat{\varphi}^*$ at 4 different rotation angles. As can be seen, the method is able to estimate the interference pattern phase shift also at angles where the deflection angle exceeds multiple times the maximal directly detectable value of p_2/l. A comparison of the reconstructed electron densities ϱ_e and ϱ_e^* from the measured and estimated phase shifts is shown in Fig. 4.10 (a) and Fig. 4.10 (b), respectively. As can be seen, the estimated reconstruction exhibits the squared profile of the cube much better, and the streak artefacts are clearly reduced. Within the region marked with the dashed square, we extracted a mean electron density of $\varrho_e = (4.79 \pm 0.93) \times 10^{29}\,\text{m}^{-3}$ and $\varrho_e^* = (5.59 \pm 0.61) \times 10^{29}\,\text{m}^{-3}$ from the measured and estimated reconstruction, respectively.
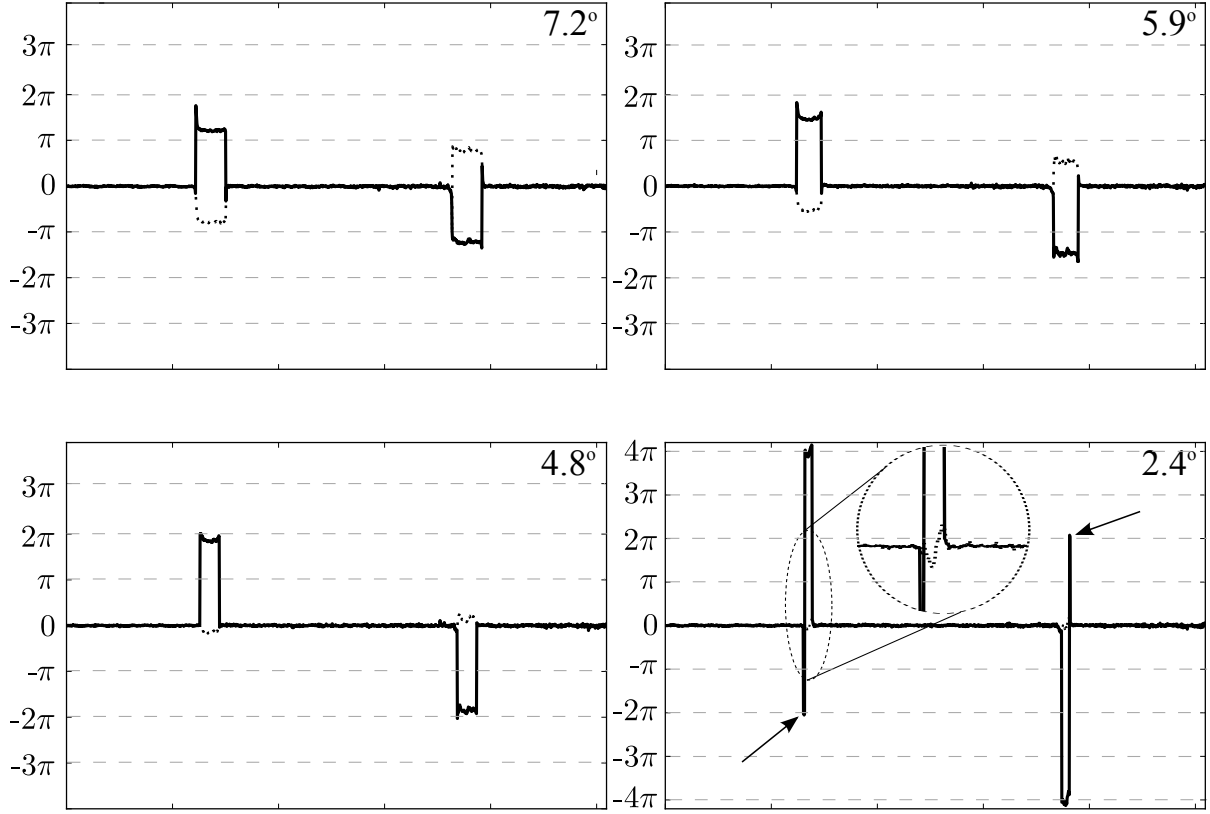
Figure 4.9: Measured (dashed) and estimated (solid) interference-pattern phase shift φ and $\hat{\varphi}^*$ for a reference X-ray energy of $E^* = 24\,\mathrm{keV}$ for 4 different rotation angles of the cube. The arrows in (d) indicates the artefacts that are most likely caused by total external reflection of the X-rays at the surface of the cube.

Compared to the value in literature $\varrho_{lit} = 6.24 \times 10^{29}\mathrm{m}^{-3}$ the error could be reduced by a factor of 2.23 [79]. The line plot through the uncorrected slice (continuous curve in Fig. 4.10(c)) shows that the square profile of the cube is strongly blurred, due to the phase wrapping artifacts. On the other hand, the line plot through the corrected slice (dashed curve in Fig. 4.10 (c)) exhibits nearly the expected square profile of the cube. The derivation from a perfect square profile and the reason for the too low electron density are mainly caused by the remaining streak artifacts. Those are the result of a wrong estimated phase-shift value, which can be seen exemplary in Fig. 4.9(d). Failures in the estimation mainly occurred at the outside of the cube, which indicate that there are different reasons for it than systematical phase wrapping. First, this unwrapping approach reaches its limits at points where the phase gradient becomes too strong, depending on the range of X-ray energies used for the measurements. In addition, at small glancing angles total external reflection of the X-rays might have occurred, which would also falsify the measured phase shift and thus lead to a wrong estimation. Further, the quality of the phase-shift signal is often poor in pixels, which are located at the edge of the object, due to the strong dark-field signal, which in turn decreases the reliability of the DPC signal.

(a) $\varrho_e \, [10^{29} \, \text{m}^{-3}]$ (b) $\hat{\varrho}_e^* [10^{29} \, \text{m}^{-3}]$ (c)
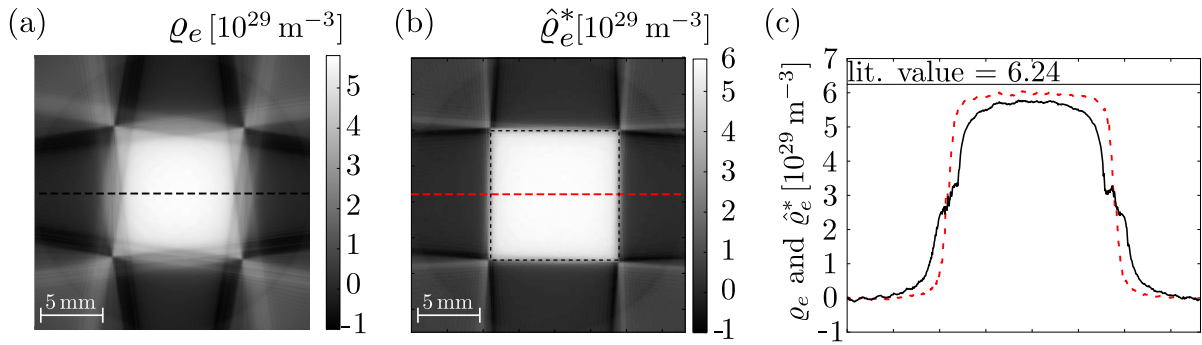

Figure 4.10: Slices through the reconstructed electron density from (a) the measured interference-pattern phase shift at 24 keV, and (b) from the estimated energy-independent interference-pattern phase shift $\hat{\varphi}^*$. The dashed squares indicate the area from which we extracted the mean electron densities of $\varrho_e = (4.79 \pm 0.93) \times 10^{29} \, \text{m}^{-3}$ and $\hat{\varrho}_e^* = (5.59 \pm 0.61) \times 10^{29} \, \text{m}^{-3}$ from the measured and estimated interference-pattern phase shift, respectively. (c) Line plots along the horizontal lines of (a) (continuous) and (b) (dashed).

4.6 Spectral phase unwrapping |
With polychromatic X-ray energy spectrum

Conventional x-ray sources typically used in the laboratory and clinical arena do provide polychromatic X-rays with a broad energy spectrum. Therefore, we cannot directly apply the unwrapping technique as described above. However, advancements in detector technology have contributed to the development of energy-resolving photon counting detectors [80–82]. As described in chapter 3, these kind of detectors have the ability to discriminate incoming x-ray photons based on their energies, hence allowing to exploit the spectral dependency of the phase shift in a single measurement at a constant tube voltage.

The detector provides a certain amount of n distinct energy bins, also referred to as energy windows, determined by respective threshold energies E_{T_i} with $i = 1, 2, ..., n$. By registering, which of the threshold energy is reached by an impinging photon, the detector allows to discriminate the X-rays with respect to their energy. Thus, for each energy window we introduce the effective energy

$$\bar{E}_i = \frac{\int_0^\infty \Phi(E) \, G(E) \, D(E) \, S_i(E) \, E \, \mathrm{d}E}{\int_0^\infty \Phi(E) \, G(E) \, D(E) \, S_i(E) \, \mathrm{d}E}. \tag{4.39}$$

Here, $\Phi(E)$ is the x-ray spectrum impinging on the detector, $G(E)$ describes the loss of X-ray photons due to their absorption by the gratings of the interferometer in the following:

$$G(E) = e^{-(\mu_{G_0}(E) \, t_{G_0} + \mu_{G_2}(E) \, t_{G_2})}, \tag{4.40}$$

with the spectral absorption coefficients $\mu_{G_0}(E)$ and $\mu_{G_2}(E)$ of the absorption gratings G_0 and G_2 with thickness t_{G_0} and t_{G_2}, respectively. Note that in Eq. (4.40), we assumed a perfect phase grating G_1 with negligible x-ray absorption. Further, $D(E)$ describes the absorption efficiency of the detector

$$D(E) = 1 - e^{-\mu_S(E) \, t_S}, \tag{4.41}$$

with the absorption coefficient μ_S of the sensor material, for instance silicon (Si) or cadmium telluride (CdTe), with thickness t_S. Finally, $S_i(E)$ describes the spectral sensitivity of the energy windows, which can be approximated in the simplest case with a rectangular function [83]

$$S_i(E) = \begin{cases} h(E - E_{T_i}) - h(E - E_{T_{i+1}}) & \text{for } i < n, \\ h(E - E_{T_n}) & \text{for } i = n, \end{cases} \tag{4.42}$$

with $E_{T_i} < E_{T_{i+1}} < ... < E_{T_n}$ and the Heaviside function $h(x)$ defined as

$$h(x) = \begin{cases} 1 & \text{for } x \geqslant 0, \\ 0 & \text{otherwise.} \end{cases} \tag{4.43}$$

Combining Eqs. (4.25) and (4.39), the effective phase shift $\varphi_{p_i}(x,y)$ for each energy window is given by:

$$\varphi_{p_i}(x,y) = \frac{r_e d}{p_2} \left(\frac{hc}{\bar{E}_i}\right)^2 \frac{\partial}{\partial x} \int \varrho_e(x,y,z)\,dz. \tag{4.44}$$

Following the same argumentation as earlier in the monochromatic case, i.e. Eq (4.30) to Eq. (4.36), a similar cost function is obtained:

$$f_{cp}(\varphi_p^*) = -\sum_i \kappa_i \cos\left(\varphi_{p_i} - \frac{E^{*2}}{\bar{E}_i^2}\varphi_p^*\right) + \gamma\varphi_p^{*2}\sum_i \kappa_i, \tag{4.45}$$

with the expected phase shift

$$\bar{\varphi}_{p_i} = \frac{E^{*2}}{\bar{E}_i^2}\varphi_p^*. \tag{4.46}$$

Thus, the estimator $\hat{\varphi}_p^*$ for the unwrapped phase shift $\hat{\varphi}_p^*$ in the polychromatic case is obtained by minimizing Eq. (4.45) with respect to φ_p^*:

$$\hat{\varphi}_p^* = \underset{\varphi_p^*}{\arg\min}\left(-\sum_i \kappa_i \cos\left(\varphi_{p_i} - \frac{E^{*2}}{\bar{E}_i^2}\varphi_p^*\right) + \gamma\varphi_p^{*2}\sum_i \kappa_i\right). \tag{4.47}$$

4.6.1 Experimental verification

In order to demonstrate the unwrapping ability of our proposed method in the case of a polychromatic X-ray source and an energy-sensitive detector, two different scenarios were performed providing an evaluation of the robustness of the method and the reliability of the estimation with respect to noise. The plastic rod sample shown in Fig. 4.11 was measured. Region 1 of the sample causes only weak phase wrapping, and a long exposure time of 20 s ensured low statistical noise, which can be seen as the best-case scenario. Region 2, which can be seen as the worst-case scenario, causes strong phase wrapping and the noise in each bin is increased due to a short exposure time of 8 s. Here, the expressions 'weak' and 'strong' phase wrapping is related to the dynamic range (i.e. gray-scale range) of the estimated DPC image. Without phase wrapping, a maximum range of $[-\pi, \pi[$ is sufficient to represent all values. If phase wrapping occurs, this dynamic range needs to be extended after phase unwrapping. If a dynamic range of $[-2\pi, 2\pi[$ is sufficient to represent all phase shift values after the phase unwrapping was done, we refer to it as 'weak phase wrapping'. The expression 'strong phase wrapping' is used if a larger range is needed.

The experiment was performed with a laboratory interferometer equipped with gratings produced by the Karlsruhe Institute of Technology (Karlsruhe, Germany). The source and the analyzer gratings consist of gold with a period of $p_0 = 14.54\,\mu m$ and $p_2 = 2.4\,\mu m$, respectively. The phase grating made of nickel had a period of $p_1 = 4.12\,\mu m$, which introduces a phase shift of approximately π to x-rays with an energy of $E_d = 25.48\,keV$. The inter-grating distances were $l = 92.3\,cm$ and $d = 15.2\,cm$, which corresponds to the
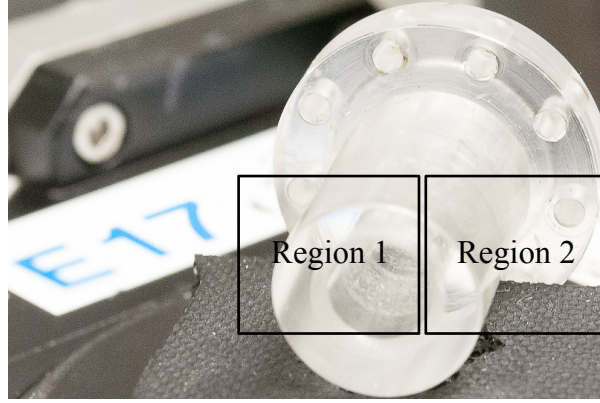
Figure 4.11: Plastic sample used in the experiment. The two regions of interest were measured with weak (**Region 1**) and strong (**Region 2**) phase wrapping appearing in the measurement.

third fractional Talbot order. An X-ray tube (XRD, GE Measurement & Control) with a tungsten anode was used. The stepping procedure was performed with the phase grating mounted to a nano-converter and 10 steps were employed for the stepping curve. The images were acquired with a prototype version of the LAMBDA detector with 128×128 pixels (pixel size = $110\,\mu m \times 110\,\mu m$). Based on the Medipix3 readout ASIC this detector provides (in this large pixel configuration) four counters and four thresholds T_0 to T_3 per pixel, which are for charge-sharing corrected on the chip. The detector was calibrated using the fluorescence lines of silver at $22.2\,keV$ and tin at $25.3\,keV$. After calibration, the energy resolution was determined to be $1.8\,keV$ FWHM at the fluorescence energy of tin. The energy windows w are defined by the thresholds and are obtained by subtracting the counter value, which corresponds to a threshold value T_H, from a counter value corresponding to a threshold value $T_L < T_H$. Four energy windows 1 to 4 were defined, listed in Table 4.1 and 4.2. The effective energies $\bar{E}_i$ were calculated with Eq. (4.39) using a simulated tungsten spectrum and taking the influence of the gratings into account. The contrast-to-noise ratio (CNR) was calculated by:

$$\text{CNR} = \frac{|s_A - s_B|}{\sqrt{\sigma_A^2 + \sigma_B^2}}, \tag{4.48}$$

where s_A, s_B, σ_A^2, and σ_B^2 are the signals and the variances within the regions of interest A and B, respectively.

In the following, we refer to the DPC images processed from the energy windows 1 to 4 as DPC_1 to DPC_4, respectively. This set of images was used for the estimation of the unwrapped phase shift using Eq. (4.34) with a regularization $R(\varphi^*)$ as given in Eq. (4.35). We refer to the estimated image as DPC^*. It is useful to compare the estimated image DPC^* with the conventional DPC image obtained with a photon-counting pixel detector with a single threshold. For this purposes, we processed the image from counter C_0 with threshold set to be $T_0 = 15\,keV$ and refer to it as DPC_r.
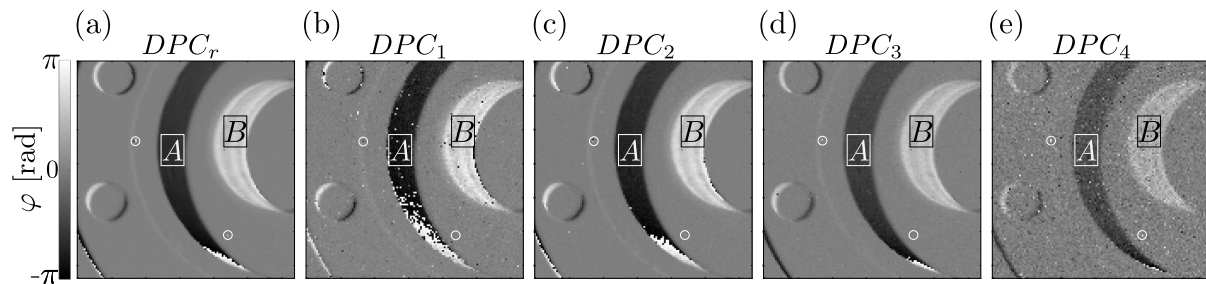
Figure 4.12: (a) Reference image DPC_r processed from counter C_0 with threshold T_0 set to be $15\,\mathrm{keV}$. (b) to (e) show respectively the images DPC_1 to DPC_4 processed from the energy windows 1 to 4, as listed in Table 4.1. The CNR values listed in Table 4.3 are calculated between the regions A and B. The circles mark pixels, which did not work properly during the measurement. As can be seen, the amount of phase wrapping decreases with increasing effective x-ray energy.

Region 1: Weak phase wrapping

The x-ray source was operated at $35\,\mathrm{kVp}$ / $40\,\mathrm{mA}$ and the spectrum was divided in four energy windows 1 to 4 with an equal width of $5\,\mathrm{keV}$. For each window and the corrsponding reference counter C_0, Table 4.1 provides the effective energies E_w, the mean counts N_0, N_s, and the visibility V_0, V_s without and with a sample in the beam, respectively. The variances σ_w^2 are given to verify the applicability of the approximation made in Eq. (4.27). The processed DPC images are shown in Fig. 4.12 (a) to (e). The phase-wrapping artefacts are clearly visible in all images. However, since the strength of the phase shift φ_w depends inversely on the x-ray energy, as derived in Eq. (4.44), the amount of phase wrapping decreases from DPC_1 to DPC_4. The effective energies of window 2 and 3 are close to the design energy of the interferometer and thus have a reasonable visibility, and additionally, a comparably high x-ray flux. The DPC images DPC_2 and DPC_3, therefore, exhibit the lowest noise levels. Due to the

Table 4.1: For each energy window w the table lists, the effective energy E_w, the visibility V_0 and the intensity N_0 without sample, the visibility V_s and the intensity N_s with sample and the variances σ_w^2 (all mean values).

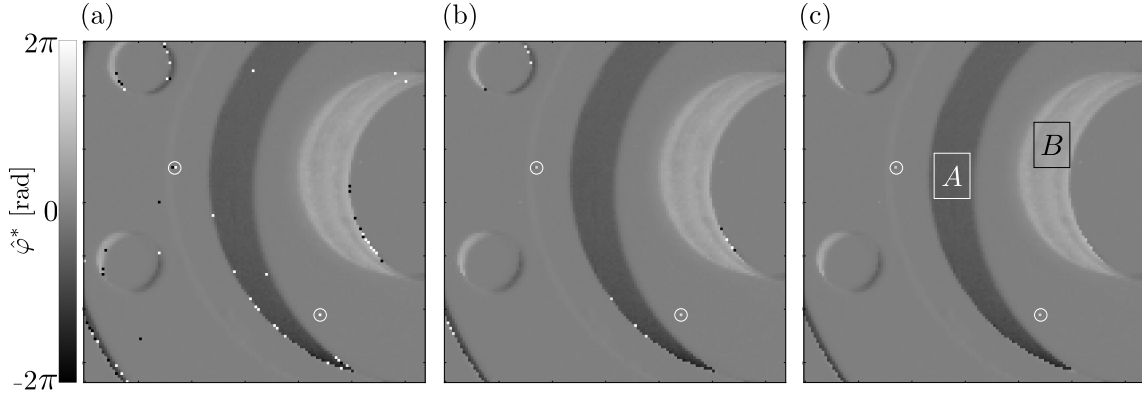| w	$T_L[\mathrm{keV}]$	$T_H[\mathrm{keV}]$	$E_w[\mathrm{keV}]$	V_0 [%]	V_s [%]	$N_0 \,|\, N_s$ [Counts]	σ_w^2
C_0	15	35	22.9	24	21	17452 | 11802	0.15
1	15	20	18.2	18	16	4147 | 2468	0.42
2	20	25	22.1	29	26	6629 | 4363	0.20
3	25	30	26.3	24	21	4318 | 3077	0.29
4	30	35	31.7	9	8	2357 | 1996	1.01

Figure 4.13: Estimated images DPC^* with $E^* = 18.2\,\mathrm{keV}$ obtained by minimizing the log-likelihood function $\ell(\varphi^*)$ with different regularization factors γ. (a) Regularization factor $\gamma = 0\,\mathrm{rad}^{-2}$ (no regularization). (b) Regularization factor $\gamma = 10^5\,\mathrm{rad}^{-2}$. (c) Regularization factor $\gamma = 6 \times 10^5\,\mathrm{rad}^{-2}$. The dynamic range is enhanced to $[-2\pi, 2\pi[$ (Please note that the scaling differs from the scaling in Fig. 4.12).The CNR was calculated between regions A and B and is given in Table 4.3. Pixels that did not work properly during the measurement are marked with circles. Since each pixel is processed individually, they do not corrupt the phase unwrapping procedure.

low x-ray statistics, there exist some randomly distributed pixels in DPC_4, which suffer from statistical phase wrapping. For the estimation of the unwrapped phase shift, the arbitrary reference energy E^* was chosen to be $18.2\,\mathrm{keV}$. The minimization was done by testing regularly spaced values of φ^*, so that the range was large enough to cover a potential phase wrapping up to eight times and, thus, to extend the dynamic range to $[-8\pi, 8\pi[$.

In order to demonstrate the influence of the regularization, we depict estimated images DPC^* that were obtained with three different regularization factors γ in Fig. 4.13 (a) to (c). Obviously, if no regularization is used ($\gamma = 0\,\mathrm{rad}^{-2}$), an incorrect value for $\hat{\varphi}^*$ is estimated for several pixels. The success of the estimation improves clearly by applying the regularization with a global factor of $\gamma = 10^5\,\mathrm{rad}^{-2}$ and the best result is obtained with a regularization factor of $\gamma = 6 \times 10^5\,\mathrm{rad}^{-2}$. In that case, the dynamic range of DPC^* is extended to $[-2\pi, 2\pi[$, and the method was able to unwrap the image with the four energy windows due the reasonably low noise and the weak phase wrapping. Note that the three pixels marked with the circles did not work properly during the measurement. Nevertheless, since each pixel is processed individually and independently from its neighbours, such pixels do not corrupt the unwrapping procedure.

In order to illustrate the effect of phase-wrapping artefacts on an integrated DPC image, we show in Fig. 4.14 (a) and (b) the images DPC_r and DPC^* after a regularized 1D integration [84]. The phase wrapping leads obviously to strong stripe artefacts, making a potential quantitative data analysis impossible. After phase unwrapping those artefacts could be reduced significantly.
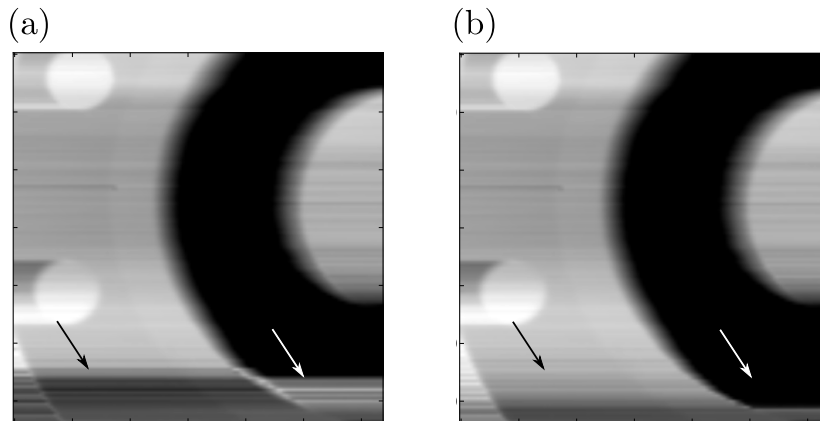
(a)   (b)

Figure 4.14: (a) The 1D integrated image obtained from the reference image DPC_r. (b) The 1-D integrated image obtained from the estimated image DPC^*.

Region 2: Strong phase wrapping

As Region 2 contained stronger gradients and consequently stronger phase wrapping could be expected, we increased the source voltage to 40 kVp / 40 mA and applied four energy windows as listed in Table 4.2. This lowers the visibility, because the mean energy of the source differs by about 3 keV from the design energy of the interferometer. However, it also enlarges the spacing between the effective energies and thus increases the differences between the measured phase shift values and supports the unwrapping. In order to evaluate the performance with higher noise levels, the exposure time was decreased to 8 s per step. Again, the reference image DPC_r shown in Fig. 4.15 (a), is strongly corrupted due to phase wrapping.

Table 4.2: For each energy window w, the table lists the effective energy E_w, the visibility V_0 and the intensity N_0 without sample, the visibility V_s and the intensity N_s with sample and the variances σ_w^2 (all mean values).

w	T_L[keV]	T_H[keV]	E_w[keV]	V_0 [%]	V_s [%]	$N_0 \mid N_s$ [Counts]	σ_w^2
C_0	15	40	26.9	19	16	8455 | 5731	0.28
1	15	22	19.1	15	12	1804 | 1029	0.83
2	22	26	23.6	27	23	2486 | 1628	0.36
3	26	30	27.4	24	21	1818 | 1270	0.46
4	30	40	33.2	9	8	2347 | 1830	1.04

Figure 4.15 (b) shows the estimated image DPC^* with $E^* = 19.1$ keV, which represents the best improvement we could obtain with a regularization factor of $\gamma = 1.3 \times 10^6$ rad^{-2}. The dynamic range is enhanced from $[-\pi, \pi[$ by a factor of 4 to $[-4\pi, 4\pi[$. Evidently, even with these manually-tuned parameters for the processing, there are pixels that still
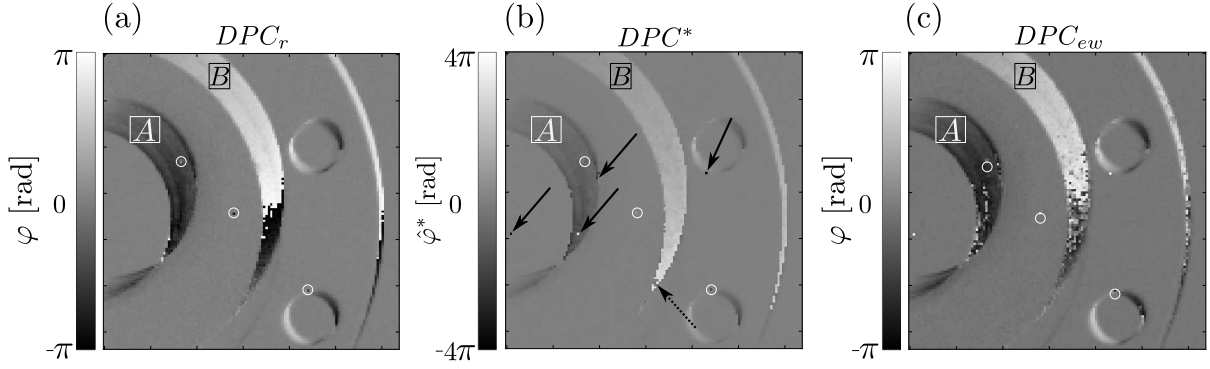
Figure 4.15: (a) The reference image DPC_r obtained from counter C_0, which is strongly corrupted by phase wrapping. (b) Estimated image DPC^* with $E^* = 19.1\,\mathrm{keV}$ representing the best improvement we could obtain using the energy windows 1 to 4, given in Table 4.2. The dynamic range was enhanced to $[-4\pi, 4\pi[$. The solid arrows indicate pixels with a wrong estimation of $\hat{\varphi}^*$, which could not be corrected with the regularization. In all images, the circles indicate pixels, which did not work properly during the measurement. The CNR values listed in Table 4.3 are calculated between the regions A and B. (c) Result as it is obtained with the purely energy-weighted method.

suffer from phase wrapping, for example the region indicated by the dashed arrow. At the same time, due to the high noise levels and the presence of strong statistical phase wrapping, an incorrect $\hat{\varphi}^*$ is estimated for some of the pixels (marked with the solid arrows). If a larger range of possible φ^* would be allowed for the minimization, more pixels could be unwrapped, but also the number of pixels with a wrongly estimated $\hat{\varphi}^*$ would increase. A smaller range, on the other hand, would eliminate the wrongly estimated pixels, but would also lower the number of pixels that are corrected for phase wrapping. Because of these opposing trends, the proposed regularization step could not completely correct for those effects. Thus, for a better unwrapping result, higher effective energies and better statistics would be necessary.

4.7 Spectral contrast-to-noise enhancement

Each energy E_i in the cost function is weighted with the variance $\sigma_i^2 = \kappa_i^{-1}$. Consequently, the CNR of the estimated image can be improved with respect to a normal processed image. Here we show that the method is a generalization of Pelzers method [14] for the case of phase wrapping.

In the case that the variances $\sigma_w^2 = \kappa_w^{-1}$ are small and the true phase shifts are so small that no phase wrapping occurs, the phase shifts obey the Normal distribution

$$f_n(\varphi, \mu) = \frac{1}{\sqrt{2\pi\sigma^2}} \exp\left(-\frac{(\varphi - \frac{E^{*2}}{E^2}\varphi^*)^2}{2\sigma^2}\right), \tag{4.49}$$

with mean value $\mu = \frac{E^{*2}}{E^2}\varphi^*$ and variance σ^2. Following the derivation given above, i.e. Eq (4.30) to Eq. (4.36), the log-likelihood function

$$l_{nw} = \sum_i \frac{1}{\sigma_i^2}\left(\varphi_i - \frac{E^{*2}}{E_i^2}\varphi^*\right)^2 \tag{4.50}$$

is obtained, where the regularization can be dropped in this limiting case. Finding the minimum of Eq. (4.50) is a weighted least-squares optimization problem. The straight forward calculation:

$$\sum_i \frac{1}{\sigma_i^2}\left(\varphi_i - \frac{E^{*2}}{E_i^2}\varphi^*\right)^2 \tag{4.51a}$$

$$= \sum_i \frac{1}{\sigma_i^2}\frac{E^{*4}}{E_i^4}\varphi^{*2} - 2\sum_i \frac{1}{\sigma_i^2}\frac{E^{*2}}{E_i^2}\varphi_i\varphi^* + \sum_i \frac{1}{\sigma_i^2}\varphi_i^2 \tag{4.51b}$$

$$= a\,\varphi^{*2} - b\,\varphi^* + c \tag{4.51c}$$

$$\overset{!}{=} 0 \tag{4.51d}$$

with $a = \sum_i \frac{1}{\sigma_i^2}\frac{E^{*4}}{E_i^4}$, $b = 2\sum_i \frac{1}{\sigma_i^2}\frac{E^{*2}}{E_i^2}\varphi_i$, and $c = \sum_i \frac{1}{\sigma_i^2}\varphi_i^2$, leads – after solving the quadratic equation – to the solution

$$\hat{\varphi}^* = \frac{1}{\sum_i \frac{E^{*4}}{E_i^4\sigma_i^2}} \sum_i \frac{E^{*2}}{E_i^2\sigma_i^2}\varphi_i. \tag{4.52}$$

Besides a scaling factor caused by the choice of E^*, Eq. (4.52) is exactly the CNR optimal weighted average of the measured phases as it is proposed by Pelzer et al. in [14]. Therefore, the proposed unwrapping approach, which estimates the true phase shift with a maximum-likelihood method, also has the advantage that it can potentially improve the contrast-to-noise ratio.

The experimental verification, was performed with the polychromatic data used in section 4.6.1.

Table 4.3: Contrast-to-noise ratios from **Region 1** and **Region 2** obtained between the regions of interest A and B from the reference image DPC_r, the images DPC_1 to DPC_4 from the energy windows 1 to 4, respectively, and the estimated image DPC^*. For comparison also the CNR of the image DPC_{ew} is given, which is obtained with Eq. (4.52).

	Image	DPC_r	DPC_1	DPC_2	DPC_3	DPC_4	DPC^*	DPC_{ew}
Region 1	**CNR**	15.2	5.2	13.4	11.7	3.3	15.5	15.6
Region 2	**CNR**	11.9	1.3	10.5	7.9	3.1	12.7	12.9

In Region 1, the CNR between the regions-of-interest A and B in DPC^* is increased by 2 % compared to the reference image, see top row of Table 4.3. The increase is slightly lower than in the pure energy-weighted image DPC_{ew}, which exhibits an improvement of 3 %. For Region 2, the CNR improvement is gathered in the bottom row of Table 4.3. The CNR in the estimated image DPC^*, is increased by approximately 7 %, again compared to the reference image DPC_r. In the energy-weighted image DPC_{ew}, shown in Fig. 4.15(c), the CNR is improved by 8 %. The difference in the CNR improvement between the derived cost function and the one used in [14] originates most likely from statistical uncertainties, since they should be the same for both methods.

4.8 Summary and discussion

In this chapter, a method to correct for phase-wrapping artefacts was derived that utilizes a set of phase shifts to estimate the unwrapped phase shift by means of the maximum-likelihood method. To serve this purpose, the set can be acquired either with multiple monochromatic measurements, as described in section 4.5, or simultaneously measured with a polychromatic X-ray source combined with an energy-resolving detector, as described in section 4.6. The approach is able to correct for phase-wrapping artifacts, and –due to the modelled energy dependency– it also reduces beam-hardening artifacts. Further, since the measured variances are used for the image weighting in the estimation procedure, it can potentially improve the contrast-to-noise ratio compared to a DPC image that is processed in a conventional way, as discussed in section 4.7.

In the monochromatic case, a dedicated X-ray interferometer is needed that allows to measure at different X-ray energies without changing its geometry (i.e. inter-grating distances, grating periods, etc.). In the polychromatic case, a standard Talbot-Lau interferometer with a conventional X-ray source and an energy-sensitive pixel detector, such as LAMBDA, can be used.

In order to apply the proposed method, no particular prior information about the sample structure or sample material is necessary. Only the x-ray spectrum impinging on the detector, as well as its spectral sensitivity need to be known to calculate the effective energy of each energy window.

With respect to the improved CNR, we could show that our method is a generalization

of Pelzer's method [14] to the case of phase wrapping. In general, the increase of the contrast-to-noise ratio depends on many factors, such as the energy spectrum, the parameters of the X-ray interferometer, the chosen energy windows, and the specimen itself. The experimental results indicate that both methods perform almost equally well with respect to CNR improvement. The ability of the method to correct DPC images pixel-by-pixel for phase-wrapping artefacts provides the advantage that the Nyquist criterion for the phase sampling does not need to be fulfilled. Since the measured quantity in DPC imaging is the spatial gradient of the phase shift, phase wrapping can occur in positive or negative direction within a distance of just a few pixels. Therefore, phase unwrapping methods using neighbouring pixels to calculate the true gradient might struggle to unwrap fine edges. In addition, the proposed method has the advantage that an error occurring during the estimation only affects the corresponding pixel without propagating through the whole image. Region growing algorithms, for example, might set whole parts of the image to a wrong value because of one wrongly determined pixel.

A limitation of the proposed method is that the unwrapping ability depends eventually on the separation of the effective energies and their maximal value, which are both bound to several constraints. First, the performance of the grating interferometer decreases for X-ray energies that differ from the design energy. For that reason, typically only a small fraction of the total spectrum can be used. Second, the limited energy resolution of the detector (and maybe dose or time issues) enforces a minimal width of the applied energy windows allowing only a small number of energy windows to be applied. In the presented experiment, an energy spectrum from 15 keV to 40 keV divided in 4 energy windows made it possible to extend the dynamic range by a factor of 4. Towards larger values, the method started to fail in estimating the unwrapped phase shift, which could not be avoided with the proposed regularization. Another issue arises from the influence of the small angle scattering (dark-field) of the x-rays on the quality of the phase-shift signal. It is well known that a strong dark-field signal decreases the quality of the extracted phase signal due to a decreased visibility [76]. This effect is not included in the model used to derive the cost function and thus leads to wrongly estimated phase-shift values. Unfortunately, there is often a co-occurrence between phase wrapping and a strong dark-field signal, as, for example, the edges of an object might cause phase wrapping, but also show a strong reduction in visibility. However, in many cases this might be correctable with an appropriate energy weighting, which identifies the pixels with a strong scattering influence, and further image processing.

Further improvement of the unwrapping ability might be reached with a different sensor material that has a better quantum efficiency for X-rays with higher energies, such as CdTe or GaAs. Hereby the effective energies of the windows could be shifted towards higher energies, which improve the counting statistics. In general, a different regularization strategy, depending on the particular case, could improve the reliability of the estimation. For example, an asymmetric unwrapping range or taking neighbouring pixels into account could support the estimation. Moreover, we foresee performance improvements of gratings as well as of single-photon–counting detectors that potentially improve the unwrapping results. In the near future, energy-sensitive single-photon–counting pixel detectors will be translated into the clinical arena. In order to evaluate the potential uti-

lization of the proposed unwrapping method for pre-clinical or clinical applications, dose considerations are important. The experiments presented above were performed with exposure times and tube settings that are rather typical for DPC imaging at a laboratory setup, so that no additional dose was needed compared to a standard DPC experiment. In general, the minimal radiation dose required for a reliable unwrapping depends primarily on the actual wrapping strength, the source spectrum, and the applied energy windows. A minimum limit is certainly given by the counting statistics, which should be good enough to avoid statistical phase wrapping in each energy bin.

Chapter 5

K-edge Imaging

In chapter 4 the additional spectral information gained when using energy-discriminating photon-counting pixel detectors was utilized to correct phase-wrapping artefacts in differential phase-contrast imaging. This chapter gives a brief introduction to K-edge imaging, which is another important application for spectrally sensitive detectors and summarizes preliminary results.

5.1 Introduction

In 1897, less than two years after C.W. Roentgen discovered the X-rays, bismuth has been used for the first time as a contrast agent to investigate the otherwise invisible gastric peristalsis [85]. From then on, many different types of materials and substances, for example mercury, lead, and cinnabar were tried among others, to increase the contrast in X-ray images [86]. Therefore, till the 30s, contrast agents to visualize many organs such as kidney, spleen, stomach, and intestines [87] were found. Those contrast agents are based on the principle that they increase the attenuation of X-rays and thereby improve the image contrast between the organ into which the contrast agent has been administered and the surrounding tissue. The next step in the use of contrast agents came up with the principle of K-edge imaging, which was first described in detail by Jacobson in 1953 [88,89]. The term 'K-edge' describes the sudden increase of the attenuation coefficient μ of a material at a certain energy as it is exemplarily shown in fig. 5.1 for the attenuation coefficients of silver and iodine. As explained in chapter 2.4.2.1, the increase is related to the binding energy of the electrons in the K-shell of the atom and appears, if the energy of the X-ray photons exceeds the binding energy allowing the X-rays to interact with the respective shell electrons by the photoelectric effect. This results in a higher probability for X-ray photons to be absorbed.

Therefore, measuring the absorption coefficient μ of a material just above and just below the K-edge, ideally with monochromatic X-ray energies, makes it possible, by subtraction of the two images, to extract an image containing only the contrast material. This is exploited in the so called K-edge imaging technique, where a contrast agent is employed to
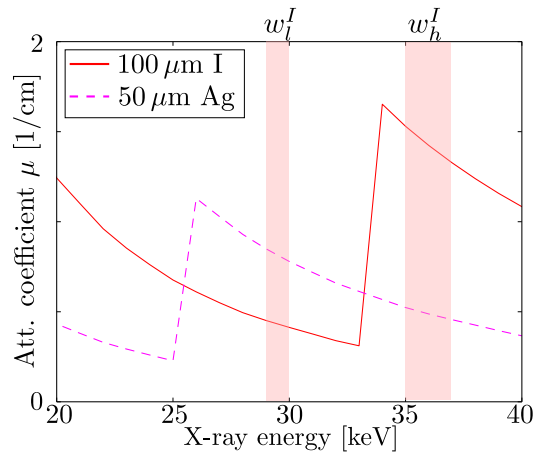
Figure 5.1: Simulated attenuation coefficient μ of silver (Ag) and iodine (I) as a function of the X-ray energy. The K-edges of silver and iodine are located at 25.5 keV and 33.2 keV, respectively. The shaded regions indicate the energy range covered by the applied energy windows w_l and w_h described in the main text.

visualize objects that would otherwise provide a rather low contrast when measured with the conventional attenuation-based imaging modality only. At synchrotron sources, which provide nearly monochromatic energies, the K-edge imaging technique is widely used to investigate for example brain structures [90], or the concentration of high-Z elements [91], and even to investigate chemical elements contained in the color pigmentation of paintings [92]. For clinical application, where only polychromatic X-ray sources are available, often dual-source or kV-switching X-ray tubes are used, which provide two different energy spectra to perform the measurement of the attenuation coefficient above and below the K-edge. However, these techniques have several disadvantages, such as a higher dose, motion artefacts, and different focal spot sizes and locations. Using an energy-sensitive detector, the measurements above and below the K-edge can be performed simultaneously, even with multiple K-edges, using the same spectrum. This approach provides further advantages that will be explained in this chapter. In the following, the K-edge extraction method using a energy-sensitive detector is described.

5.2 K-edge extraction | Log-difference method

For extracting the K-edge image, two measurements of the attenuation coefficients μ_h and μ_l at X-ray energies just above and just below the K-edge of the contrast agent are needed. If an energy-insensitive detector is used, it is necessary that the two images are acquired separately with two different source settings. This increases the applied dose and renders the image registration difficult in cases where the object moves between the two images, for instance due to breathing. Those issues can be overcome by using an energy-sensitive detector. It opens up the possibility to acquire the two images simultaneously by applying two energy windows h and l above and below the K-edge, respectively as it is illustrated

in fig. 5.1. Each energy window delivers a transmission image I_h and I_l given by

$$
\begin{aligned}
I_l &= I_{0_l} e^{-(\mu_l^c d_l^c + \mu_l^b d_l^b)} \\
I_h &= I_{0_h} e^{-(\mu_h^c d_h^c + \mu_h^b d_h^b)}.
\end{aligned} \tag{5.1}
$$

Here, $I_{0_{l,h}}$ depict the incoming X-ray flux provided by the source, $\mu_{l,h}^c$ and $d_{l,h}^c$ are the attenuation coefficient and the thickness of the contrast agent, and $\mu_{l,h}^b$ and $d_{l,h}^b$ are the attenuation coefficient and the thickness of the background material, each within the respective energy window. If the energy windows are chosen to be close to the absorption edge there is a large variation between the attenuation coefficient μ_h^c and μ_l^c but a negligible variation between μ_h^b and μ_l^b. Thus, by subtracting the logarithms of Eq. (5.1), divided by the incoming flux $I_{0_{l,h}}$ within the respective energy window, an image K can be extracted:

$$
K = \log(\frac{I_h}{I_{0_h}}) - \log(\frac{I_l}{I_{0_l}}) \tag{5.2a}
$$

$$
= -\mu_h^c d_h^c - \mu_h^b d_h^b + \mu_l^c d_l^c + \mu_l^b d_l^b \tag{5.2b}
$$

$$
\approx \mu_l^c d_l^c - \mu_h^c d_h^c. \tag{5.2c}
$$

This subtracted image contains contrast only arising from to the K-edge difference.

5.2.1 Experimental verification

In order to evaluate the capability to extract the K-edge with Eq. (5.2c), a phantom was measured that contains 3 mm plastic tubes filled with different concentrations of iodine $(88, 60, 39, 26, 17$ and 12 mg/ml$)$. Additionally, a purely water containing tube, a chicken bone, and a tube containing silver diluted with water were imaged. The attenuation coefficients have a K-edge at 33.2 keV for iodine and at 25.5 keV for silver, respectively. In order to first extract the iodine K-edge two energy windows $w_l^I = 29 - 30$ keV and $w_h^I = 35 - 37$ keV were applied located below and above the iodine K-edge, respectively, as depicted in fig. 5.1.

Figure 5.2 (a) and (b) depict the median-filtered transmission images I_l and I_h, which were acquired with a LAMBDA detector equipped with a 300 μm thick silicon sensor with an exposure time of 10 s. As expected, the image I_h contains stronger iodine contrast, compared to I_l, due to the increased attenuation coefficient. The bad pixels in I_l arise from the low counting statistics and from the fact that the energy-window width, chosen to be 1 keV, is smaller than the actual mean energy resolution of the detector determined to be 1.8 keV FWHM at 25.5 keV. Figure 5.2 (c) shows the median-filtered iodine K-edge image which was extracted by using the introduced log-diff method in Eq. (5.2c).

The iodine samples with concentrations above 17 mg/ml are extracted clearly, whereas the background materials including the plastic tubes and the pure-water sample are removed well. However, the bone and the water-silver solution are visible with an reversed contrast due to the not negligible difference in the attenuation coefficients between the two energy windows. This can be seen from the line plots given in fig. 5.2 (d): The transmission of
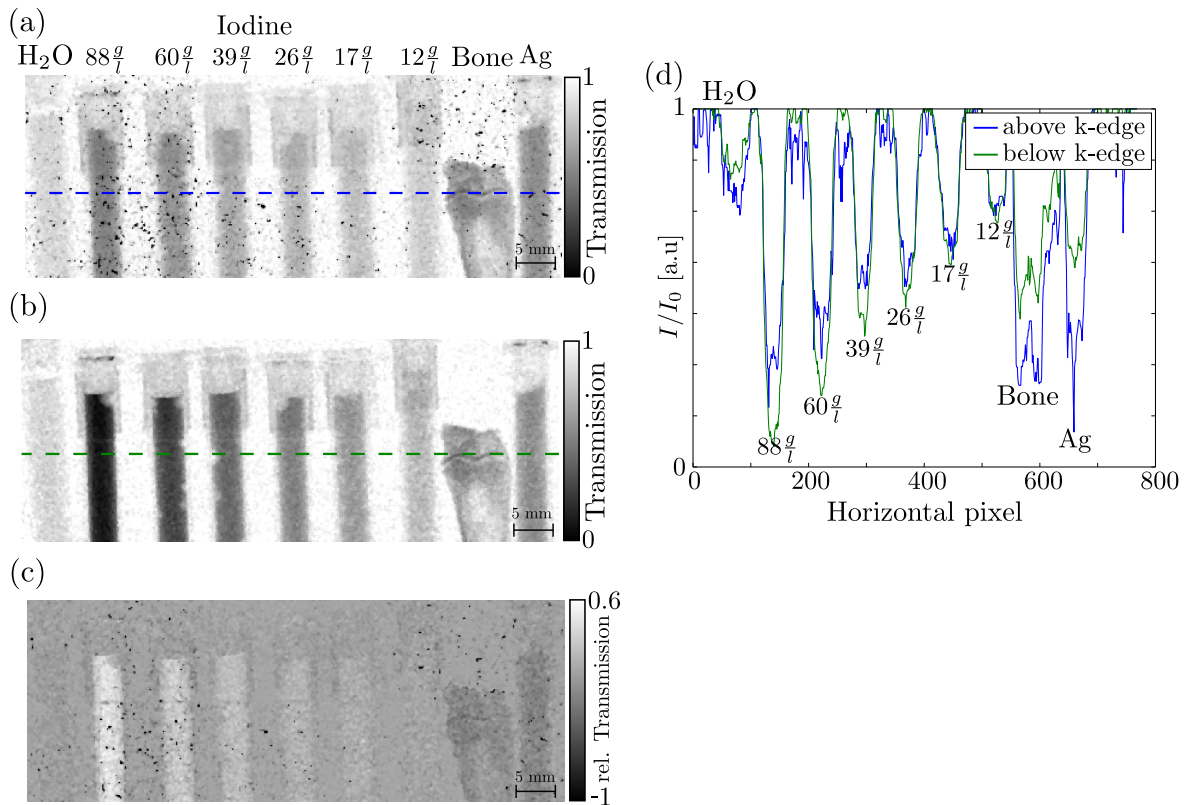
Figure 5.2: (a) and (b) depict the transmission images I_l and I_h of the K-edge phantom obtained from the energy-windows w_l and w_h, defined in the text, below and above the iodine K-edge energy, respectively. The K-edge phantom consists of 3 mm thick plastic tubes containing pure water, different concentrations of iodine (as indicated), silver diluted with water, as well as a chicken bone. (c) The K-edge image extracted with the log-difference method of Eq. (5.2c). (d) Line plots along the dashed lines in the transmission images. In the transmission image (b) the contrast of the iodine sample is higher and the contrast of the other materials is lower compared to transmission image (a).

the X-rays for the pure water sample is almost the same in both energy windows, while it differs for the bone and silver sample. Since the attenuation continuously decreases with increasing X-ray energy, if there is no K-edge present, the difference contrast of the two other high-Z materials have the opposite sign compared to iodine. Another reason for the poor differentiation ability of the low iodine concentrations is the rather thin Si sensor of the detector. Since the photon absorption efficiency of silicon decreases exponentially with increasing X-ray energy, the effectively measured difference across the K-edge of the iodine attenuation coefficient is strongly reduced as shown in fig. 5.3 (a). The dashed line represents the iodine attenuation coefficient without the influence of the Si sensor, while the solid lines show the attenuation coefficient combined with the X-ray absorption efficiency of the silicon sensor. Due to the poor absorption efficiency for the high-energy photons above the K-edge, the ratio between μ_h^{iodine} and μ_l^{iodine} decreases from 3.1 to 1.84. To improve the differentiation capability of the low concentration iodine from the
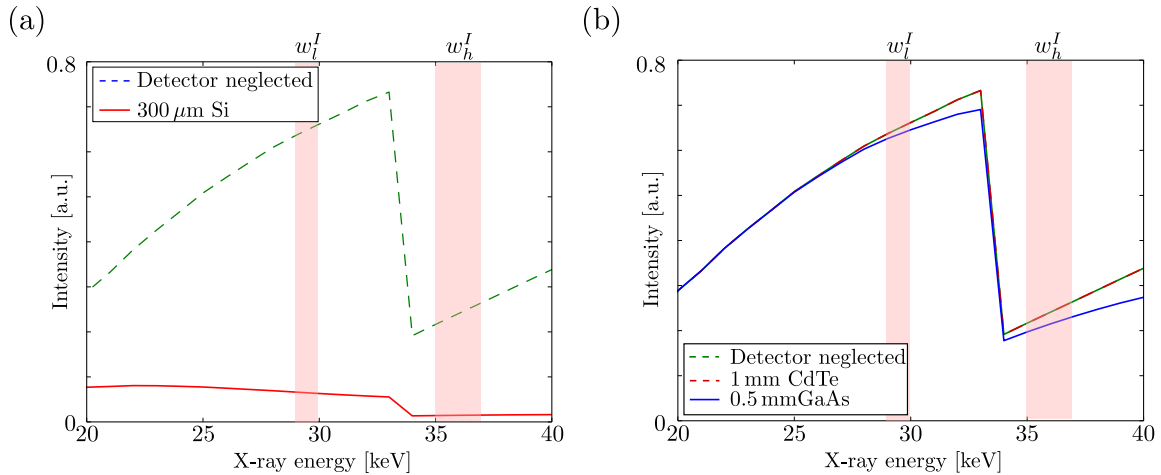
Figure 5.3: Influence of the detector sensor material on the measured intensity and thus on the effectively measured K-edge variance. a) The dashed line depicts the intensity behind a $100\,\mu$m thick iodine phantom without the influence of the silicon sensor. The solid line shows the intensity measured with a $300\,\mu$m thick silicon sensor. b) Using a high-Z sensor material such as CdTe and GaAs improves the absorption efficiency (Fluorescence effects are neglected). Thus, the intensity variation across the K-edge is more pronounced.

background material, it would be necessary to apply a higher dose by either increasing the exposure time or the X-ray flux. If dose or time are restricted, a different sensor material with a higher photon absorption efficiency, for instance CdTe or GaAs, would be helpful, as depicted in fig. 5.3 (b).

However, because of the opposite contrasts between materials with and without a K-edge in between the energy windows it is possible to threshold the K-edge image K such that a positive K-edge image as shown in fig. 5.4 (a) is obtained, where only the iodine contrast remains. This allows an improved visual discrimination of the iodine compared to fig. 5.2 (c). The circles mark the iodine that stayed in the cap of the 88 mg/ml iodine tube during the filling process and the air bubbles entrapped in the phantom. Further, the thresholding technique can be used to color the iodine in the pure transmission image as shown in fig. 5.4 (b). Applying different threshold levels allows to obtain a map of the projected iodine thickness within the sample as depicted in fig. 5.4 (c).

5.2.2 Energy-window width optimization

The log-difference method of Eq. (5.2c) works well for cases with negligible variation between the attenuation coefficients of the background material μ_h^b and μ_l^b is negligible across the energy windows. In addition, narrow windows around the K-edge result in a large difference of the absorption coefficient across the observed edge. This requires the energy windows to be as narrow as possible and to be located very close to the K-edge. However, a narrow energy window provides poor counting statistic and, consequently, increased noise [93]. Furthermore, the energy resolution of the detector limits both, the minimal
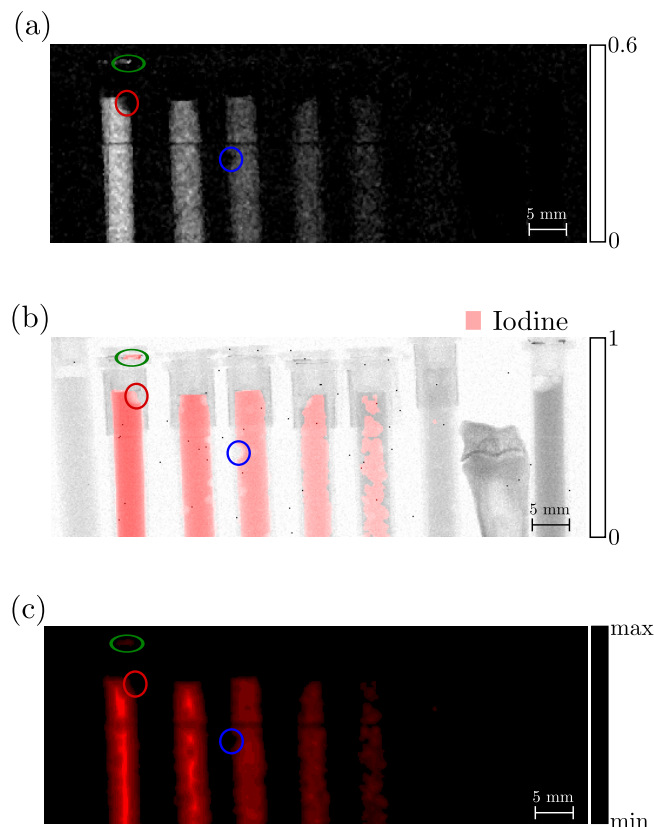
Figure 5.4: a) Positive K-edge image obtained by restricting the K-edge image to above zero values. By this thresholding, all other materials vanish in the image. (b) Transmission image where the iodine content is visualized. (c) Iodine thickness map obtained by using multiple threshold levels. The green circle marks iodine that stayed in the cap of the tube during the filling process. The red and blue circles mark air bubbles.

distance between the energy windows and the K-edge as well as the window width itself. Therefore, for an optimal contrast in the K-edge image K a trade-off between those effects needs to be found. The optimal energy-window width can be found by an optimization of the signal-to-noise ratio (SNR). Figure 5.5 (a) shows the SNRs of the iodine samples with 88 mg/ml and 26 mg/ml as well as of the other samples as a function of the energy-window width. As expected, the SNR of the iodine contrast contains a maximum which is, for this specific case, located at 4 keV. For the materials without a K-edge between the energy windows, there is no such maximum. Instead, the SNR increases continuously with increasing energy-window width, due to the lower noise for broader energy windows. Figure 5.5 (b) shows the corresponding log-diff images for 2 keV, 4 keV ,and 7 keV, respectively, where the coloured squares indicate the regions of interest for the calculation of the SNR. As can be seen, increasing the energy-window width from 2 keV to 4 keV decreases the contrast in the iodine, but even more the background noise, and thus leads to an increased SNR. A further increase, however, leads to a proportionally higher reduction in iodine contrast relative to the reduction in noise, and thus the SNR decreases.
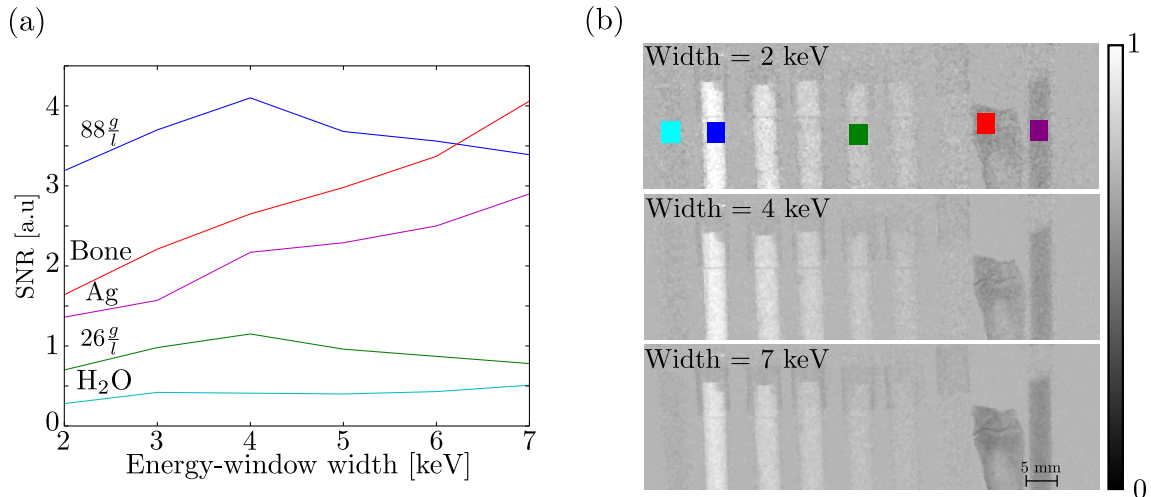
Figure 5.5: a) Signal-to-noise ratio (SNR) as a function of the energy-window width. The SNRs of the iodine samples feature a maximum at 4 keV. b) K-edge images obtained with energy-window widths of 2 keV (upper), 4 keV (middle) and 7 keV (lower). The painted squares mark the regions-of-interest used for the SNR calculation.

5.3 Multiple K-edges imaging

In principle, the extraction of a single K-edge can also be performed with a dual-energy approach using different algorithms. However, by the use of an energy sensitive photon-counting detector one gains the advantage that typically more than two energy windows can be applied. Thereby, multiple K-edges located at different energies can be distinguished simultaneously. Since different contrast agents often accumulate in different parts of the body, more energy windows make it possible to distinguish those parts with a single-shot measurement. The experimental feasibility of multi-energy photon-counting K-edge imaging in pre-clinical computed tomography has been investigated by several groups [83, 94, 95].

In the following, the feasibility of multi K-edge imaging using LAMBDA as imaging detector is investigated. As showed above, a good SNR in the k-edge images requires the energy windows to be set relatively close below and above the investigated edge. Therefore, the number of k-edges that can be detected with a given number of independent energy windows depends on the distribution of the edges across the incident X-ray spectral range. In general, every k-edge needs four thresholds in order to be properly detected (e.g. figure 5.1). The LAMBDA detector, operated in color mode, offers a total amount of eight thresholds and thus a maximum of eight energy windows can be applied. Hence, at least two different K-edges can be discriminated. If, however, the interesting K-edges are located closely together on the energy scale, every second energy window may be shared for the detection of neighbouring edges and so a total of three material could be discriminated. In the presented case with iodine and silver as contrast agents, four energy windows w_1 to w_4 used for the log-diff method were defined as $w_l^{Ag} = 20 - 23$ keV, $w_h^{Ag} = 27 - 29$ keV, $w_l^I = 29 - 32$ keV, and $w_h^I = 35 - 39$ keV. Figure 5.6 (a) to (c) depict

the image of the silver K-edge, the respective positive K-edge image and the silver-marked transmission image of the silver K-edge, which was extracted from w_1 and w_2. Figure 5.6 (d) shows the transmission image where the iodine (red) and the silver (blue) K-edges have been marked with the thresholding approach explained above.
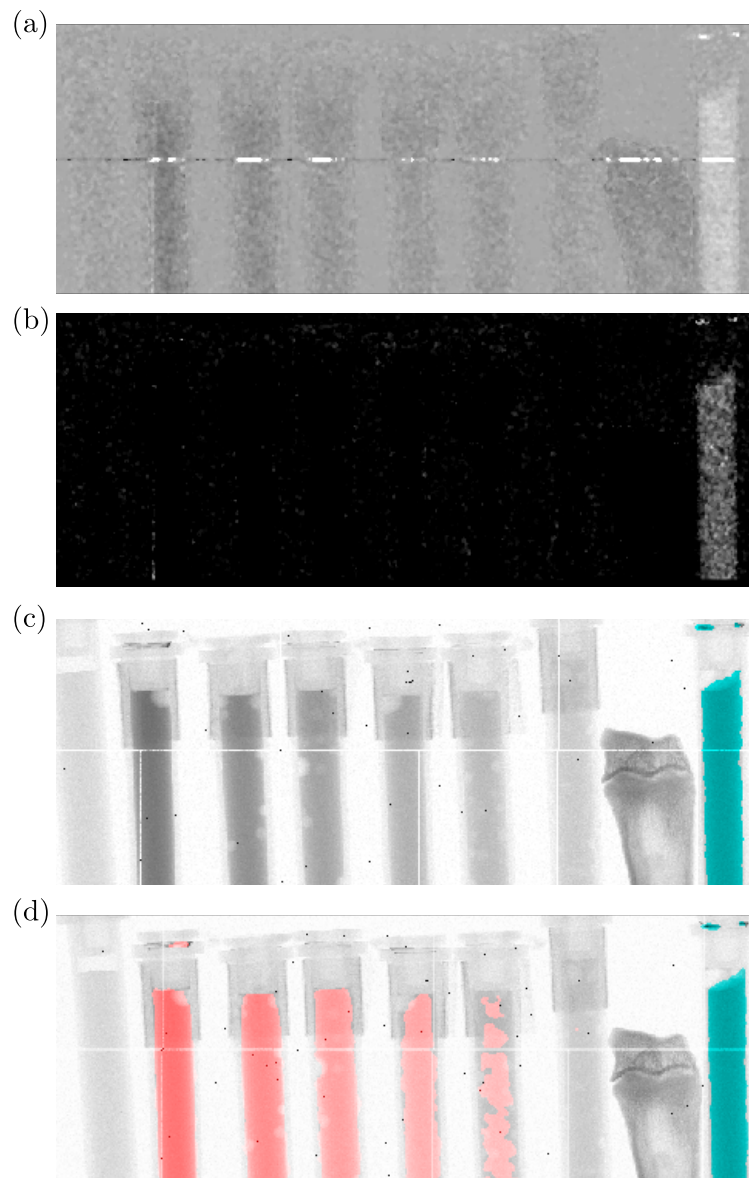

Figure 5.6: (a) Image of the extracted silver K-edge. (b) Positive K-edge image for silver obtained by restricting the K-edge image to values above zero. (c) Transmission image of the phantom where the silver content is marked by superimposing the positive K-edge image. (d) Transmission image where both, silver and iodine, have been marked by blue and red, respectively. Both K-edges can be extracted from a single measurement by applying four energy windows simultaneously.
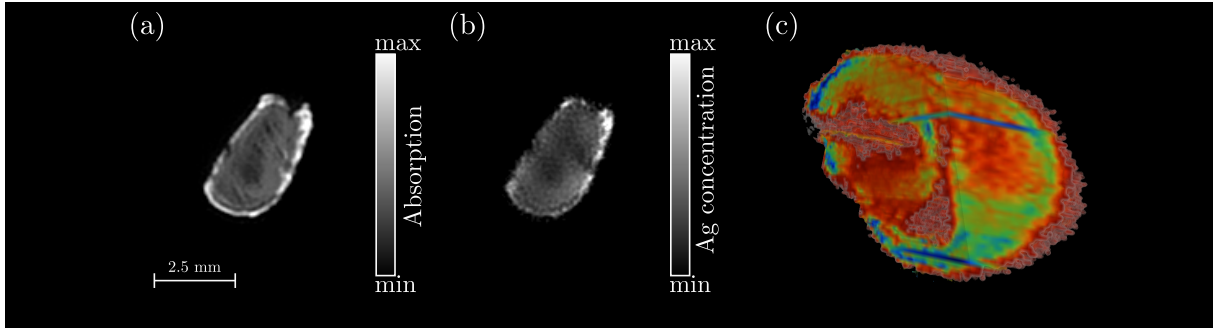
Figure 5.7: (a) Attenuation image of a mouse liver stained with iodine. (b) Extracted K-edge image of the mouse liver. Both images show the highest silver concentration at the edge of the heart and a decreasing concentration with increasing depth into the tissue. (c) 3D-representation of the K-edge image.

5.4 K-edge imaging | Samples stained with iodine and silver

In biomedical ex-vivo imaging conventional attenuation-based X-ray imaging is particularly useful for the characterisation of highly absorbing structures such as the skeleton and calcifications. However, its benefit is very limited for the investigation of soft tissues such as the brain structure, the lung, or the liver. In order to better depict those weakly absorbing tissues it has been demonstrated that certain contrast agents can be utilized to stain the soft tissue in order to enhance the X-ray attenuation [96]. The staining is usually performed by following a certain protocol that includes the tissue to be soaked in a staining solution. Thereby, the dye penetrates the specimen. Recently, it has been shown that dedicated staining protocols allow to mark the distinct tissues within the specimen differently, which allows a better differentiation [97].

Further improvement might be gained, if the specimen is stained by multiple staining solutions that can be differentiated by their spectral information, for example the different locations of the K-edges. In cases where the staining solutions adsorb with varying concentrations at certain parts of the specimen, a further differentiation can be made. During this work, an iodine-stained mouse liver as well as a silver-stained mouse heart were measured in conventional attenuation and K-edge imaging method as described in section 5.2. For the tomography, the source was set to 60 kVp and 801 images where acquired equally distributed over 360°. The images were taken with the LAMBDA detector with two energy windows 'low' and 'high' set to be $w_l = 29-32$ keV and $w_h = 35-39$ keV, respectively and with a total exposure time of 7 s per image. The attenuation and K-edge image as well as the 3D reconstruction of the mouse liver is shown in fig 5.7 (a), (b) and (c), respectively. Obviously, both the absorption image and the K-edge image show a high concentration of the iodine staining at the edge of the liver. The concentration decreases with increasing depth into the tissue. Due to the poor resolution because of the small specimen dimensions and the comparatively large pixel size of 50 μm it is difficult
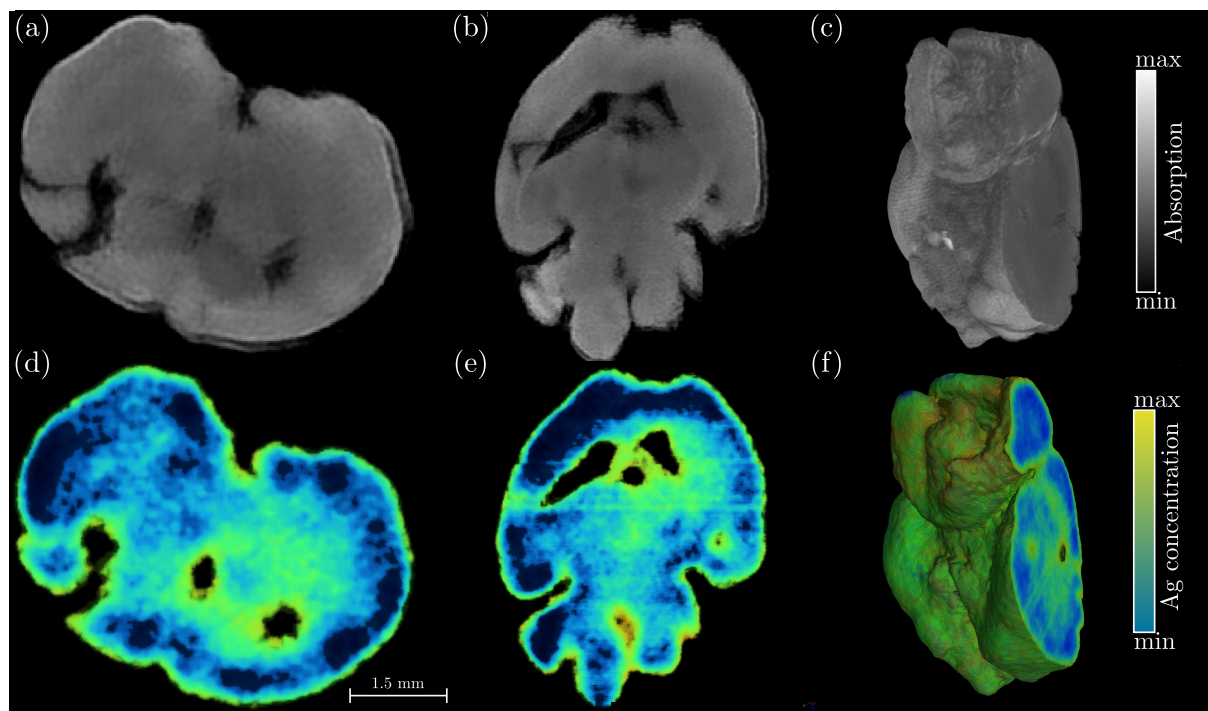
Figure 5.8: Mouse heart stained with silver. (a) Axial plane, (b) sagittal plane, and (c) the 3D-representation of conventional attenuation based CT scan. (d) Axial plane, and (e) sagittal plane, and (f) 3D-representation of the extracted K-edge image. The K-edge image shows regions with lower iodine concentrations, which do not appear as clear in the attenuation image. (Note: The artefacts which are visible in the reconstructed slices are due to sample movements.)

to perform a detailed analysis. Nevertheless, the 3D representation of the K-edge clearly shows regions with differing silver concentrations. For the tomography of the mouse heart, which was stained with silver, the two energy windows 'high' and 'low' were set to be $w_l = 20 - 23 \, \text{keV}$ and $w_h = 26 - 29 \, \text{keV}$, respectively. The source was again set to $60 \, \text{kVp}$ and 801 images were taken equally spaced over $360°$ with an exposure time of $7 \, \text{s}$ per image. Again, different concentrations of silver can be seen in both, the absorption images, fig 5.8 (a)-(c) and the K-edge images (d)-(f). Again, in both imaging modalities, the margins of the sample shows the highest concentration of iodine. However, the K-edge image shows certain parts (marked with arrows), in which the iodine concentration seems to be reduced. In contrast, these parts cannot be distinguished as easily in the conventional attenuation image. The reason for that could not be answered on the basis of those two test images, but further studies need to be performed. Moreover, a sample containing both staining materials, iodine and silver, was not available within the framework of this thesis, but would be an interesting case to investigate.
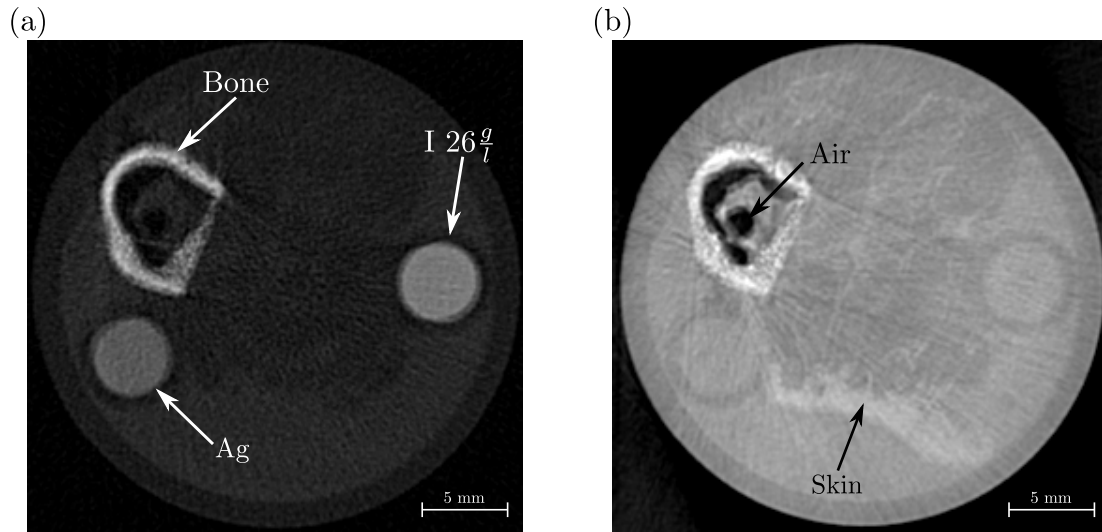
Figure 5.9: CT reconstruction of a phantom sample containing soft tissue, bone, a silver-water solution, and 26 mg/ml iodine solution. (a) Pure attenuation image and (b) pure phase-contrast image. The images were extracted from the counter with the lowest threshold set to be $Th_1 = 20$ keV. In both images it is difficult to distinguish between the silver from the iodine solution.

5.5 K-edge imaging | Combined with differential-phase imaging

As introduced in chapter 1, differential-phase imaging (DPC) provides three kinds of images: the conventional attenuation-based image, the differential-phase contrast image, and the small angle scattering (dark-field) image, which contain a complementary information about the specimen. The differential phase-contrast images typically provide better soft tissue contrast than the attenuation-based images. Therefore, DPC imaging might provide sufficient information about different types of tissue without the application of a contrast agent at all. Nevertheless, since an energy-sensitive detector provides the images acquired at different energy regimes as an add-on to the conventional single-threshold measurement, a combination of both methods is possible without additional effort. Therefore, fusing the phase-contrast imaging with the K-edge imaging technique can be interesting to further improve the diagnostic value, for instance by investigating the washout characteristics of a contrast-enhanced DPC-CT scan for the examination of adrenal lesions. In particular, the combination of dark-field and K-edge images could improve the diagnostic outcome in cases where the phase images are not usable due to phase wrapping, for instance in the field of myelography. Further, in mammography a combination of the dark-field and K-edge images would make it possible to extract not only the structure, but also the angiogenesis around a breast tumor at an early stage.

In order to evaluate the possibility to combine phase-contrast imaging with K-edge imaging, we used the 3 mm plastic tubes with 26 mg/ml iodine concentration and the
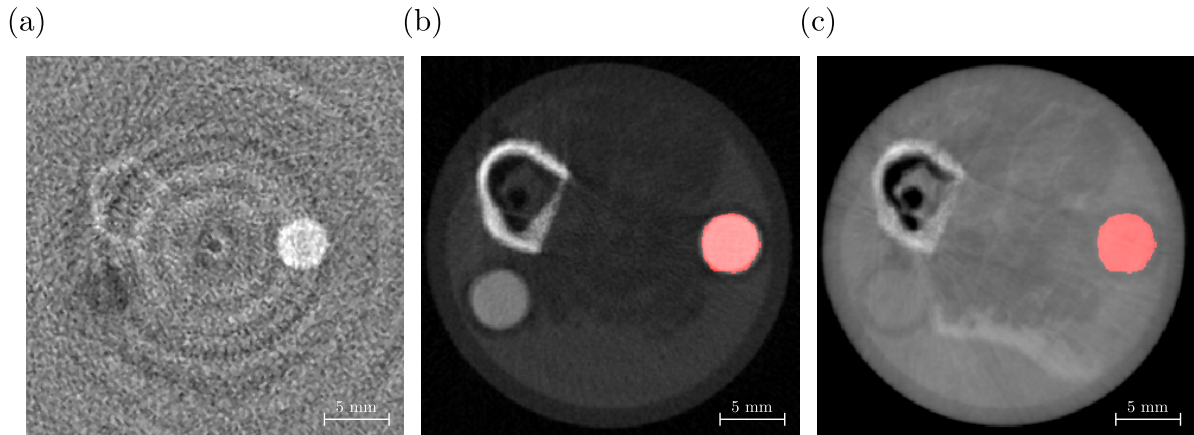
Figure 5.10: (a) Iodine K-egde image of the sample presented in Fig. 5.9 extracted with the log-diff method. (b) and (c) depict the attenuation and phase-contrast image, respectively. The iodine content is marked using the threshold technique explained in 5.2.1.

silver-water solution with an unknown concentration as contrast agents. Those were buried in a phantom, which contained skin, muscle and fatty tissue and bone. A tomographic measurement was performed selecting four energy windows $w_l^{Ag} = 20 - 23 \, \text{keV}$, $w_h^{Ag} = 26 - 29 \, \text{keV}$, $w_l^I = 29 - 32 \, \text{keV}$ and $w_h^I = 35 - 39 \, \text{keV}$. Figure 5.9 (a) and (b) show the pure attenuation and the phase-contrast images, respectively, which are extracted from the single threshold set to be $\text{Th}_1 = 20 \, \text{keV}$. As can be seen, the phase-contrast image contains a complementary information to the attenuation image and has a better soft tissue contrast. However, in both images it is not easily possible to distinguish the silver from iodine samples by applying only a single threshold. Figure 5.10 (a) shows exemplarily the iodine K-edge image extracted with the log-diff method of eq. (5.2c) and (b) and (c) show the attenuation and phase-contrast images where the iodine is marked using the threshold technique, respectively. Figure 5.11 (a) and (b) show the attenuation and phase-contrast images where the silver and iodine content is marked, respectively. The regions containing the contrast agents were marked using the threshold technique, which was applied after the extraction of the silver and the iodine K-edge images.

(a)   (b)
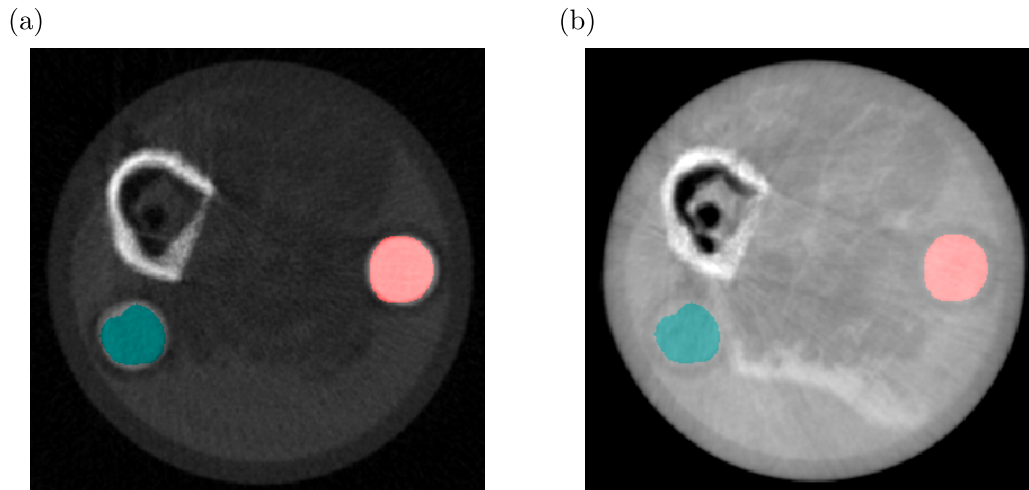
Figure 5.11: The attenuation (a) and phase contrast image (b), where the silver and the iodine content have been separated by applying the threshold technique explained in 5.2.1.

5.6 Summary and discussion

In this chapter, it was shown, that the LAMBDA detector can be utilized to perform K-edge imaging. Up to four energy windows were applied to distinguish two contrast agents; namely silver and iodine, simultaneously. For the extraction of the K-edge image, the log-difference method given by eq. (5.2c) was used as described in section 5.2. The optimal energy-window widths for the 'low' and 'high' energy windows utilized to extract silver and iodine K-edges were obtained with the SNR optimization approach introduced in section 5.2.2. With that, the best K-edge extraction results were obtained with energy window widths of $w_l^{Ag} = 20 - 23\,\mathrm{keV}$, $w_h^{Ag} = 27 - 29\,\mathrm{keV}$, $w_l^I = 29 - 32\,\mathrm{keV}$, and $w_h^I = 35 - 39\,\mathrm{keV}$ for silver and iodine, respectively. It was demonstrated that an ordinary threshold procedure can be used to identify iodine concentrations down to approximately $17\,\mathrm{mg/ml}$. Lower iodine concentrations could not be identified due to the Si-sensor of the LAMBDA detector used in this study, as it provides a poor absorption efficiency for X-ray photons above $30\,\mathrm{keV}$. Nevertheless, it could be demonstrated that both contrast agents (silver and iodine) can be identified simultaneously within one single acquisition. Thereby, this verifies one of the main advantages of spectral detectors with multiple energy windows over dual-energy approaches. In addition, the K-edge imaging technique was combined with the grating-based differential-phase imaging method. Here, it was demonstrated that in some cases it remains difficult to distinguish contrast agents, for instance silver from iodine, in both contrast modalities, i.e. attenuation and phase contrast, due to low concentrations of the contrast agents. It has been shown that K-edge imaging can be combined with grating-based phase-contrast imaging, for example, to distinguish different specific contrast agents or to determine concentration differences. Further work will be necessary to investigate the medical benefit when combining both methods, and the applied radiation dose with regard to the necessary image quality has to be considered.

Chapter 6

Summary, Conclusions and Perspectives

This chapter summarizes the main achievements obtained within this PhD thesis and provides conclusions and perspectives for further developments and research. The chapter follows the structure of the chapters 3 to 6.

High-speed readout implementation
A preliminary high-speed readout with internal bit reordering was designed in VHDL. The complete design, including the bit reordering, was implemented at a LAMBDA prototype module that consisted of six Medipix3 chips. It was proven to work reliable up to a frame rate of 750 Hz. However, the resources of the Virtex5-70T FPGA were not sufficient to make an implementation for the full LAMBDA module, which consists of 12 Medipix3 chips, possible. Therefore, a modified readout version without the internal bit reordering was implemented for the full LAMBDA module, which allowed for first high-speed experiments. An implementation of the full high-speed readout including the bit reordering for the full LAMBDA module would require a larger FPGA with more resources. In addition, a re-design might be necessary that uses different FPGA resources for the reordering task for some of the chips. This would make the signal-routing process more difficult and probably limit the maximal readout speed. Since the main issue for the high-speed readout is the large amount of data that needs to be buffered on the FPGA, a board re-design providing additional external memory or a second FPGA would relax the routing and timing complexity. The current status of the LAMBDA detector was published in [53,56].

Spectral phase unwrapping in differential phase-contrast imaging with multiple monochromatic measurements
A new phase unwrapping method applicable for differential phase-contrast imaging was presented. The method exploits the energy dependency of the phase shift, which makes it possible to estimate the unwrapped phase shift from measurements at different energies. The estimation is done with the maximum-likelihood method using the normal and 'von Mises' distribution to model the uncertainty of the measurement due to the presence of noise. The method was first evaluated at a synchrotron where monochromatic energies are available. A dedicated grating interferometer allowed to measure the object multiple

times at different energies without changing the inter-grating distances. The results proofed that the method is able to unwrap the corrupted phase even if all individual measurements suffered from wrapping. The method and experimental results were published in Epple et al. (2013) [70].

In perspective, work about the limitations and the success of the unwrapping procedure in connection with the number of distinct energy values is open for further investigation.

Spectral phase unwrapping in differential phase-contrast imaging with energy-sensitive detector

It was demonstrated that the unwrapping method can be translated to a standard polychromatic X-ray tube combined with an energy-sensitive detector. It was shown that those detectors allow to measure the phase shifts simultaneously at different energies, which can be used successfully to estimate the unwrapped phase shift. The method and the experimental results were published in Epple et al. (2014) [71].

In conclusion, this study demonstrated the general concept to utilize the spectral information of an energy-sensitive detector to reduce artefacts resulting from phase wrapping. Further work will be necessary in order to investigate the limits of the method, for example, in terms of energy-window widths and number of energy-windows, among others. Moreover, additional studies are mandatory to give a reliable estimation about the dose that is necessary to ensure a correct phase unwrapping.

K-edge imaging

It was demonstrated that K-edge imaging is feasible using the LAMBDA detector. A study about multi K-edge imaging with two contrast agents, i.e. silver and iodine was performed successfully, showing that the distinguishability of two contrast agents simulataneously in one single measurement is possible. Further, it was illustrated that additional information can be gained when K-edge imaging is combined with phase contrast imaging. The K-edge images were extracted by using a simple log-difference method that was introduced in the according chapter.

A detailed study about the minimal dose that is necessary to extract the K-edge images and about the additional information that is gained by using different combinations of contrast agents together with phase-contrast imaging remains to be performed in the future.

Conclusion

In this work, a first step was accomplished to evaluate the impact of spectral detectors on grating-based phase-contrast imaging. The results of this work demonstrate that the additional information provided by spectral X-ray imaging allows to reduce artefacts and can be used to obtain to gain extra knowledge about the sample properties. Ultimately, it contributes to the translation of both grating-based phase-contrast imaging and spectral detectors to in routine applications in materials science and, potentially, the clinical arena.

Bibliography

[1] Wilhelm Conrad Röntgen. Über eine neue Art von Strahlen. *Sitzungsberichte der Würzburger Physik.-Medic.-Gesellschaft*, 1898.

[2] Assmus Alexi. Early History of X-Rays, 1995.

[3] A. et al. Snigirev. On the possibility of X-ray phase contrast microimaging by coherent highenergy synchrotron radiation. *Rev. Sci. Inst.*, 66:54865492, 1995.

[4] S. et al. Wilkins. Phase-contrast imaging using polychromatic hard X-rays. *Nature*, 384:335338, 1996.

[5] T. et al. Davis. Phase-contrast imaging of weakly absorbing materials using hard X-rays. *Nature*, 373(19):595598, 1995.

[6] L. et al. Chapman. Diffraction enhanced X-ray imaging. *Phys. Med. Biol.*, (42):20152025, 1997.

[7] C. David, B. Nöhammer, and E. Ziegler. Differential X-ray phase contrast imaging using a shearing interferometer. *Appl. Phys. Lett.*, 81:3287–3290, 2002.

[8] T. et al. Takeda. Vessel imaging by interferometric phase-contrast X-ray technique. *Appl. Phys. Lett.*, 105:17081712, 2002.

[9] Thomas Weber, Peter Bartl, Florian Bayer, Jurgen Durst, Wilhelm Haas, Thilo Michel, Andre Ritter, and Gisela Anton. Noise in x-ray grating-based phase-contrast imaging. *Medical Physics*, 38(7):4133, 2011.

[10] Florian Bayer, Karl Gödel, Wilhelm Haas, Jens Rieger, Andr Ritter, Thomas Weber, Lukas Wucherer, Jürgen Durst, Thilo Michel, and Gisela Anton. Spectroscopic darkfield imaging using a grating-based talbot-lau interferometer, 2012.

[11] T Weber, F Bayer, W Haas, G Pelzer, J Rieger, A Ritter, L Wucherer, J Durst, T Michel, and G Anton. Energy-dependent visibility measurements, their simulation and optimisation of an x-ray talbot-lau interferometer. *Journal of Instrumentation*, 7(02):P02003, 2012.

[12] T. Thuering, W. C. Barber, Y. Seo, F. Alhassen, J. S. Iwanczyk, and M. Stampanoni. Energy resolved X-ray grating interferometry. *Applied Physics Letters*, 102(19):191113, 2013.

[13] J.S. Iwanczyk, E. Nygard, O. Meirav, J. Arenson, W.C. Barber, N.E. Hartsough, N. Malakhov, and J.C. Wessel. Photon Counting Energy Dispersive Detector Arrays for X-ray Imaging. *IEEE Transactions on Nuclear Science*, 56(3):535–542, 2009.

[14] Pelzer G., Weber T., Anton G., Ballabriga R., Bayer F., Campbell M., Gabor T., Haas W., Horn F., Llopart X., Michel N., Mollenbauer U., Rieger J., Ritter I., Sievers P., Stefan W. W., Winnie S., Zang A., and Michel T. *"Grating-based x-ray phase-contrast imaging with a multi energy-channel photon-counting pixel detector"*. *Opt. Express*, 21(22):25677–25684, (2013).

[15] Georg Pelzer, Andrea Zang, Gisela Anton, Florian Bayer, Florian Horn, Manuel Kraus, Jens Rieger, Andre Ritter, Johannes Wandner, Thomas Weber, Alex Fauler, Michael Fiederle, Winnie S. Wong, Michael Campbell, Jan Meiser, Pascal Meyer, Jürgen Mohr, and Thilo Michel. Energy weighted x-ray dark-field imaging. *Opt. Express*, 22(20):24507–24515, Oct 2014.

[16] J Anthony Seibert. X-Ray Imaging Physics for Nuclear Medicine Technologists. Part 1: Basic Principles of X-Ray Production. pages 139–147, 2004.

[17] Jens Als-Nielson and Des McMorrow. *Elements of Modern X-ray Physice*. WILEY, Chichester, West Sussex, 2011.

[18] Andrey V Gitin. Huygens-Feynman-Fresnel principle as the basis of applied optics. *Applied optics*, 52(31):7419–34, 2013.

[19] M. Bech. X-ray imaging with a grating interferometer. Phd thesis, University of Copenhagen, 2009.

[20] Goodman J. W. *Introduction to Fourier Optics*. The MscGraw-Hill Companies, Chichester, West Sussex, 2nd edition edition, 1996.

[21] Bushberg J. T., Seibert J. A., Leidholdt E.M., and Boone J.M. *The Essential Physics of Medical Imaging*. Lippincott, Williams and Wilkins, Philadelphia, PA 19106 USA, 2002.

[22] M Yaffe and J Rowlands. X-ray detectors for digital radiography. *Physics in medicine and biology*, 42:1–39, 1997.

[23] Lowe B. G. and Sareen R. A. *Semiconductor X-Ray Detectors*. CRC Press, Boca Raton, USA, 2013.

[24] H. Spieler. *Semiconductor Detector Systems*. Oxford University Press, New York, USA, 2009.

[25] A. Konstantinidis. *Evaluation of digital X-ray detectors for medical imaging applications.* Lap Lambert Academic Publishing, 2012.

[26] Physical Reference Data. @ONLINE.

[27] Christopher Allwork, Dimitris Kitou, Sandeep Chaudhuri, Paul J. Sellin, Paul Seller, Matthew C. Veale, Nicola Tartoni, and Perumal Veeramani. X-ray beam studies of charge sharing in small pixel, spectroscopic, CdZnTe detectors. *IEEE Transactions on Nuclear Science*, 59(4):1563–1568, 2012.

[28] W. S. Boyle and G. E. Smith. Charge Coupled Semiconductor Devices. *Bell Sys. Tech. J.*, 49, 1970.

[29] G. F. Amelio, M. F. Tompsett, and G. E. Smith. Experimental Verification of the Charge Coupled Device Concept. *Bell Sys. Tech. J.*, 49, 1970.

[30] S. T. Sheppard, M. R. Melloch, and J. A. Jr. Cooper. Characteristics of inversion-channel and buried-channel MOS devices in 6H-SiC. *IEEE Trans. Electron Devices*, 14, 1994.

[31] Paul K. Weimer. The TFT A New Thin-Film Transistor. *Proceedings of the IRE.*, 50, 1962.

[32] X. Llopart, R. Ballabriga, M. Campbell, L. Tlustos, and W. Wong. Timepix, a 65k programmable pixel readout chip for arrival time, energy and/or photon counting measurements. *NIM in Physics Research A*, 581, 2007.

[33] Katsuyuki Taguchi and Jan S Iwanczyk. Vision 20/20: Single photon counting x-ray detectors in medical imaging. *Medical physics*, 40(10):100901, 2013.

[34] Nigel G Anderson and Anthony P Butler. Clinical applications of spectral molecular imaging: potential and challenges. (May 2013), 2014.

[35] Taly Gilat Schmidt. Optimal image-based weighting for energy-resolved CT. *Medical Physics*, 36(7):3018, 2009.

[36] K Rajendran, M F Walsh, N J A de Ruiter, A I Chernoglazov, R K Panta, A P H Butler, P H Butler, S T Bell, N G Anderson, T B F Woodfield, S J Tredinnick, J L Healy, C J Bateman, R Aamir, R M N Doesburg, P F Renaud, S P Gieseg, D J Smithies, J L Mohr, V B H Mandalika, A M T Opie, N J Cook, J P Ronaldson, S J Nik, A Atharifard, M Clyne, P J Bones, C Bartneck, R Grasset, N Schleich, and M Billinghurst. Reducing beam hardening effects and metal artefacts in spectral CT using Medipix3RX. *Journal of Instrumentation*, 9(03):P03015, 2014.

[37] Fabian Bamberg, Alexander Dierks, Konstantin Nikolaou, Maximilian F. Reiser, Christoph R. Becker, and Thorsten R C Johnson. Metal artifact reduction by dual energy computed tomography using monoenergetic extrapolation. *European Radiology*, 21(7):1424–1429, 2011.

[38] Computed tomography with energy-resolved detection: a feasibility study. *Physics in medicine and biology*, 53(5):1475–95, 2008.

[39] Energy-resolved computed tomography: first experimental results. 53(20):5595–613, oct 2008.

[40] R Aamir, a Chernoglazov, C J Bateman, a P H Butler, P H Butler, N G Anderson, S T Bell, R K Panta, J L Healy, J L Mohr, K Rajendran, M F Walsh, N de Ruiter, S P Gieseg, T Woodfield, P F Renaud, L Brooke, S Abdul-Majid, M Clyne, R Glendenning, P J Bones, M Billinghurst, C Bartneck, H Mandalika, R Grasset, N Schleich, N Scott, S J Nik, a Opie, T Janmale, D N Tang, D Kim, R M Doesburg, R Zainon, J P Ronaldson, N J Cook, D J Smithies, and K Hodge. MARS spectral molecular imaging of lamb tissue: data collection and image analysis. *Journal of Instrumentation*, 9(02):P02005–P02005, 2014.

[41] B. Henrich, J. Becker, R. Dinapoli, P. Goettlicher, H. Graafsma, H. Hirsemann, R. Klanner, H. Krueger, R. Mazzocco, A. Mozzanica, H. Perrey, G. Potdevin, B. Schmitt, X. Shi, A.K. Srivastava, U. Trunk, and C. Youngman. The adaptive gain integrating pixel detector AGIPD a detector for the European XFEL. *NIM in Physics Research Section A*, 633, 2010.

[42] Paganin D. M. *Coherent X-ray Optics*. Oxford University Press, Oxford, England, 2006.

[43] T. Weitkamp, C. David, C. Kottler, O. Bunk, and F. Pfeiffer. Tomography with grating interferometers at low-brilliance sources. *Proc. of SPIE*, 6318, 2006.

[44] Born M. and Wolf E. *Principles of Optics*. Pergamon Press, Oxford, England, sixth ed. edition, 1993.

[45] F Pfeiffer, M Bech, O Bunk, P Kraft, E F Eikenberry, Ch Brönnimann, C Grünzweig, and C David. Hard-X-ray dark-field imaging using a grating interferometer. *Nature materials*, 7(February):134–137, 2008.

[46] M Engelhardt, C Kottler, O Bunk, C David, C Schroer, J Baumann, M Schuster, and F Pfeiffer. The fractional Talbot effect in differential x-ray phase-contrast imaging for extended and polychromatic x-ray sources. *Journal of microscopy*, 232(1):145–57, 2008.

[47] A. Hipp, M. Willner, J. Herzen, S. Auweter, M. Chabior, J. Meiser, K. Achterhold, J. Mohr, and F. Pfeiffer. Energy-resolved visibility analysis of grating interferometers operated at polychromatic X-ray sources. *Optics Express*, 22(25):30394, 2014.

[48] S. Ehn. Experimental investigation of the new LAMBDA detector for x-ray spectral phase-contrast. Diploma thesis, Technische Universiät München, 2013.

[49] F. Pfeiffer, T. Weitkamp, O. Bunk, and C. David. Phase retrieval and differential phase-contrast imaging with low-brilliance X-ray sources. *Nautre Physics*, 2(4):258–261, 2006.

[50] Kak A. C. and M. Slaney. *Principles of Computerized Tomographic Imaging.* IEEE Press, The lnstitute of Electrical and Electronics Engineers, Inc., New York, 1999.

[51] S. W. Smith. *The Scientist and Engineer's Guide to Digital Signal Processing.* California Technical Publishing, USA, 1997.

[52] F Pfeiffer, C. Kottler, O. Bunk, and C. David. Hard-X-ray dark-field imaging using a grating interferometer. *Phys. Rev. Lett.*, 98, 2007.

[53] D Pennicard, S Lange, S Smoljanin, H Hirsemann, H Graafsma, M Epple, M Zuvic, M-O Lampert, T Fritzsch, and M Rothermund. The LAMBDA photon-counting pixel detector. *Journal of Physics: Conference Series*, 425, 2013.

[54] R Ballabriga, J Alozy, G Blaj, M Campbell, M Fiederle, E Frojdh, E H M Heijne, X Llopart, M Pichotka, S Procz, L Tlustos, and W Wong. The Medipix3RX: a high resolution, zero dead-time pixel detector readout chip allowing spectroscopic imaging. *Journal of Instrumentation*, 8:C02016–C02016, 2013.

[55] Daniel Durini Romero. Solid-State Imaging in Standard CMOS Processes . Doctoral thesis, Universität Duisburg-Essen, 2009.

[56] David Pennicard, Sabine Lange, Sergej Smoljanin, Julian Becker, Helmut Hirsemann, Michael Epple, and Heinz Graafsma. Development of LAMBDA: Large Area Medipix-Based Detector Array. *Journal of Instrumentation*, 6(11):C11009–C11009, 2011.

[57] S. Smoljanin. Entwicklung der Firmware eines Auslese- und Steuerungssystems für das "Large Are Medipix Based Detektor Array". Diploma thesis, Hochschule Mittweida, University of Applied Sciences, 2013.

[58] D. Pennicard, S. Smoljanin, I. Sheviakov, Q. Xia, A. Rothkirch, Y. Yu, B. Struth, H. Hirsemann, and H. Graafsma. High-speed readout of high-Z pixel detectors with the LAMBDA detector. *Journal of Instrumentation*, 9(12):C12014–C12014, 2014.

[59] R. Ballabriga and X. Llopart. *Medipix3RX manual*, volume 1.4. 2012.

[60] W. J. Dally and J. W. Poulton. *Digital Systems Engineering.* Cambridge University Press.

[61] M. Shinagawa, Y. Akazawa, and T. Wakimoto. Jitter analysis of high-speed sampling systems. Diploma thesis, 2013.

[62] Nicola Da Dalt, Moritz Harteneck, Christoph Sandner, and Andreas Wiesbaue. On the Jitter Requirements of the Sampling Clock for Analog-to-Digital Converters. *IEEE Transaction on circuits and systems I: Fundamental Theory and Applications*, 49(9):1354–1360, 2002.

[63] XILINX. *Virtex-5 FPGA User Guide.*

[64] G. Burton. 16-Channel, DDR LVDS Interface with Per-Channel Alignment. *Application Note: Virtex-5 FPGAs*, XAPP855 (v1.0), 2006.

[65] D. C. Ghiglia and M. D. Pritt. *Two-Dimensional Phase Unwrapping: Theory, Algorithms, and Software.* John Wiley & Sons, New York, Chichester, 2008.

[66] Iwan Jerjen, Vincent Revol, Philipp Schuetz, Christian Kottler, Rolf Kaufmann, Thomas Luethi, Konstantins Jefimovs, Claus Urban, and Urs Sennhauser. Reduction of phase artifacts in differential phase contrast computed tomography. *Optics express*, 19(14):13604–11, jul 2011.

[67] Wilhelm Haas, M. Bech, P. Bartl, F. Bayer, a. Ritter, T. Weber, G. Pelzer, M. Willner, K. Achterhold, J. Durst, T. Michel, M. Prümmer, F. Pfeiffer, G. Anton, and J. Hornegger. Phase-unwrapping of differential phase-contrast data using attenuation information. pages 79624R–79624R–6, mar 2011.

[68] L. Ritschl, S. Sawall, S. Schüller, and et al. Optimizing the antiderivative of X-ray differential phase contrast data for tomographic reconstruction. *Proc. 2nd Intl. Mtg. on image formation in X-ray CT*, page 218221, 2012.

[69] S. Asbeck. Phase-Wrapping Correction for X-Ray Phase-Contrast Computed Tomography. Master thesis, Technische Universität München, 2012.

[70] P. Thibault S. Ehn J. Herzen A. Hipp F. Beckmann F. M. Epple, G. Potdevin and F. Pfeiffer. Unwrapping differential x-ray phase-contrast images through phase estimation from multiple energy data. *Opt. Express*, 21:29101–29108, 2013.

[71] Franz M. Epple, Sebastian Ehn, Pierre Thibault, Thomas Köhler, Guillaume Potdevin, Julia Herzen, David Pennicard, Heinz Graafsma, Peter B. Noel, and Franz Pfeiffer. Phase unwrapping in spectral x-ray differential phase-contrast imaging with an energy-resolving photon-counting pixel detector. *IEEE Transactions on Medical Imaging*, 2014.

[72] Jean-Marie Bonny, Michel Zanca, Jean-Yves Boire, and Annie Veyre. Maximum Likelihood Estimation from Multiple Spin- Echo Magnitude Images. *Magnetic Resonance in Medicine*, (36):287–293, 1996.

[73] J. Sijbers, A. J. den Dekker, E. Raman, and D. Van Dyck. Parameter Estimation from Magnitude MR Images. *Int J Imag Syst Tech*, (10):109–114, 1999.

[74] G. Cowan. *"Statistical data analysis". Oxford University Press Inc., New York*, pages 70–93, (1998).

[75] D. Hahn. *"Statistical iterative reconstruction for X-ray phase-contrast computed tomography". PhD Thesis, Technische Universität München*.

[76] M. Chabior. *"Contributions to the characterization of grating-based x-ray phase-contrast imaging". PhD Thesis, Technische Universität München*.

[77] J. Herzen, T. Donath, F. Beckmann, M. Ogurreck, C. David, J. Mohr, F. Pfeiffer, and A. Schreyer. *"X-ray grating interferometer for materials-science imaging at a low-coherent wiggler source"*. Rev. Sci. Instrum., 82(11):113711, (2011).

[78] Klaus J. Engel, D. Geller, T. Köhler, G. Martens, S. Schusser, G. Vogtmeier, and E. Rössl. Contrast-to-noise in X-ray differential phase contrast imaging. *Nuclear Instruments and Methods in Physics Research Section A: Accelerators, Spectrometers, Detectors and Associated Equipment*, 648, 2011.

[79] The Phantom Laboratory. *Catphan504Manual*. 2012.

[80] P. Fischer, A. Helmich, M. Lindner, N. Wermes, and L. Blanquart. A photon counting pixel chip with energy windowing. *IEEE Trans. Nucl. Sci.*, 47.

[81] R. Ballabriga, M. Campbell, E. Heijne, X. Llopart, L. Tlustos, and W. Wong. Medipix3: A 64k pixel detector readout chip working in single photon counting mode with improved spectrometric performance. *Nucl. Instrum. Meth. Phys. Res. Sec. A*, 633.

[82] R. Steadman, C. Herrmann, O. Mülhens, and D. G. Maeding. ChromAIX: Fast photon-counting ASIC for spectral computed tomography. *Nucl. Instrum. Meth. Phys. Res. Sec. A*, 648.

[83] Roessl E. and Proksa R. *"K-edge imaging in x-ray computed tomography using multi-bin photon counting detectors"*. Phys. Med. Biol., 52.

[84] S. Schleede. *"X-ray phase-contrast imaging at a compact laser-driven synchrotron source."*. PhD Thesis, Technische Universität München.

[85] J. CR. Roux and BALTRASARD V. Etude du fonctionnement moteur de l'estomac. *Arch. de Physiol.*, 10(85), 1898.

[86] Heubner W. and Schüller J. *Handbuch Der Experimentellen Pharmakologie*. Verlag von Julius Springer, BERLIN, 1939.

[87] P. Radt. Eine Methode der röntgenologischen Kontrastdarstellung von Milz und Leber. *Klin Wschr.*, 8(2128), 1929.

[88] B. Jacobson. *Acta Radiol.*

[89] P. Edholm and Jacobson B. Quantitative determination of idoine in-vivo. *Acta Radiol.*, 52:337–346, 1959.

[90] J. F. Adam, C. Nemoz, A. Bravin, S. Fiedler, S.and Bayat, S. Monfraix, G. Berruyer, A. M. Charvet, J. F. Le Bas, H. Elleaume, and F. Estève. High-resolution blood-brain barrier permeability and blood volume imaging using quantitative synchrotron radiation computed tomography: study on an F98 rat brain glioma. *Journal of cerebral blood flow and metabolism*, 25:145–153, 2005.

[91] J F Adam, S Bayat, L Porra, H Elleaume, F Estève, and P Suortti. Quantitative functional imaging and kinetic studies with high-Z contrast agents using synchrotron radiation computed tomography. *Clinical and experimental pharmacology & physiology*, 36(December 2007):95–106, 2009.

[92] K. Krug, J. Dik, M. den Leeuw, A. Whitson, J. Tortora, P. Coan, C. Nemoz, and A. Bravin. Visualization of pigment distributions in paintings using synchrotron K-edge imaging. *Applied Physics A*, 83(2):247–251, 2006.

[93] He P., Wei B., Cong W., and Wang G. "Optimization of K-edge imaging with spectral CT". *Med. Phys.*, 39(11):6572–6579, (2012).

[94] J P Schlomka, E Roessl, R Dorscheid, S Dill, G Martens, T Istel, C Bäumer, C Herrmann, R Steadman, G Zeitler, a Livne, and R Proksa. Experimental feasibility of multi-energy photon-counting K-edge imaging in pre-clinical computed tomography. *Physics in medicine and biology*, 53(15):4031–47, 2008.

[95] Sebastian Feuerlein, Ewald Roessl, Roland Proksa, Gerhard Martens, Oliver Klass, Martin Jeltsch, Volker Rasche, Hans-Juergen Brambs, Martin H K Hoffmann, and Jens-Peter Schlomka. Multienergy photon-counting K-edge imaging: potential for improved luminal depiction in vascular imaging. *Radiology*, 249(3):1010–1016, 2008.

[96] Neu Corey P. and Genin Guy M. *Handbook of Imaging in Biological Mechanics*. CRC Press Taylor & Francis Group, 6000 Broken Sound Parkway NW, Boca Raton, FL 33487-2742, 2014.

[97] Karl Degenhardt, Alexander C Wright, Debra Horng, Arun Padmanabhan, and Jonathan a Epstein. Rapid 3D phenotyping of cardiovascular development in mouse embryos by micro-CT with iodine staining. *Circulation. Cardiovascular imaging*, 3(3):314–22, 2010.

Publications and Scientific Presentations

Publications

Ehn S., Epple F. M., Fehringer A., Pennicard D., Graafsma H., Noël P. B., Pfeiffer F. X-ray deconvolution microscopy, submitted to *Opt. Express*, August, (2015).

Epple F. M., Ehn S., Thibault P., Köhler T., Potdevin G., Herzen J., Pennicard D., Graafsma H., Noel P. B., and Pfeiffer, F., Phase unwrapping in spectral X-ray differential phase-contrast imaging with an energy-resolving photon-counting pixel detector, *IEEE Transactions on Medical Imaging*, 34(**3**), pp. 816-823, (2014).

Epple F. M., Potdevin G., Thibault P., Ehn S., Herzen J., Hipp A., Beckmann F., and Pfeiffer F., Unwrapping differential X-ray phase-contrast images through phase estimation from multiple energy data, *Opt. Express*, 21(**24**), pp. 29101-29108, (2013).

Pennicard D., Lange S., Smoljanin S., Hirsemann H., Graafsma H., Epple F. M., Zuvic M., Lampert M.-O., Fritzsch T., and Rothermund M., The LAMBDA photon-counting pixel detector, *Journal of Physics: Conference Series*, **245**, (2013).

Pennicard D., Lange S., Smoljanin S., Becker J., Hirsemann H., Epple F. M., and Graafsma H., Development of LAMBDA: Large Area Medipix-Based Detector Array, *Journal of Instrumentation*, 11(**6**), (2011).

Conferences | Oral and poster presentations

Phase unwrapping of differential phase-contrast images with multiple monochromatic measurements. *DESY User Meeting*, Hamburg, Germany, **2014**.

Spectral X-ray imaging methods using the new LAMBDA detector. International Workshop on X-ray and Neutron Phase Imaging with Gratings (XNPIG) and Symposium on Biomedical Phase-Contrast Imaging (IMXP), Garmisch-Partenkirchen, Germany, **January 2014**.

Large area Medipix3 Detector for energy-resolved phase-contrast imaging used in material science. *European Congress and Exhibition on Advanced Materials and Processes (EUROMAT)*, Sevilla, Spain, **February 2013**.

Medical imaging and non-destructive testing with the LAMBDA detector. *IEEE Medical Imaging Conference*, Seoul, South Korea, **November 2013**.

Energy-sensitive phase-contrast imaging using the Large Area Medipix-Based Detector Array: LAMBDA. *SPIE Medical Imaging*, San Diego, USA, **February 2012**.

Large Area Medipix3 Based Detector Array for energy-resolved phase-contrast imaging. *Workshop Detector technologies and systems platform* , Dresden, Germany, **September 2012**.

Large Area Medipix3 Detector for biomedical phase contrast imaging. *International Workshop on X-ray and Neutron Phase Imaging with Gratings (XNPIG)*, Tokyo, Japan, **March 2012**.

Medipix3 for biomedical phase contrast imaging. *International Workshop on Radiation Imaging Detectors (IWORID)*, Zurich, Switzerland, **2011**.

Acknowledgements

The work and results achieved in this thesis would not have been successful without the contributions and help of many people that I would like to acknowledge in the following.

First of all, I would like to thank my academic supervisor Prof. Dr. Franz Pfeiffer for the opportunity to work on this topic. Thank you for your support, motivation and patience in all aspects that were necessary for the success of this thesis. Thank you for the chance to participate at scientific conferences all over the world and the professional opportunities you made possible to me. Most importantly, I want to mention that the unique working atmosphere you have created at you chair and your spirit to offer everyone the freedom that one needs has made going to work always a pleasure.

I would like to acknowledge and thank Prof. Dr. Sibylle Ziegler for being my second supervisor.

Further, I would like to thank Prof. Dr. Heinz Graafsma and the whole detector group at DESY. I got the opportunity to visit the group many times during the LAMBDA development process and always enjoyed the friendly atmosphere.
In particular, I would like to thank Dr. David Pennicard who acted as kind of a supervisor and was a very competent advisor for detector electronics. Thank you very much for patiently answering all my questions and concerns I had about detector electronics and manufacturing. Thank you for the good time at DESY where I have learned a lot.
Also, I would like to thank Sergej Smoljanin for his support with the FPGA programming. It was always a pleasure to discuss about the implementations and progresses.
Furthermore, I would like to acknowledge Igor Sheviakov from DESY for answering all my questions about the practical habits of FPGA devices.
In this context, I also want to acknowledge the Medipix3 collaboration at CERN.

Then, I would like to acknowledge all my diploma students, to whom I am grateful for their valuable work.
First and foremost, I would like to thank Sebastian Ehn who was my first diploma student and who became a good friend during that time. Thank you for supporting me with the setup and the detector implementation, as well as the fruitful discussions which pleasurably annoyed our office mates. Your support helped me a lot!
Further, I would like to thank Stephan Kaczmarz, my second diploma student, for the